Ministério de Ciência y Tecnologia, Observatório Nacional/Brasil
Friedrich-Alexander-Universität Erlangen-Nürnberg/Alemanha

ESPECTROSCOPIA QUANTITATIVA DE ESTRELAS OB

Hydrogênio, Hélio e Carbono

María Fernanda Nieva

Tese para obtenção do título de doutor
Programa de orientação bilateral (co-tutelle)

Orientadores:
Dra. Katia Cunha e Dr. Ulrich Heber

Erlangen - Maio de 2007

A Tese foi apresentada às 14:30 horas do dia 21 de Maio de 2007, na sala de seminarios do departamento de Física do Estado Sólido da Universidade de Erlangen-Nürnberg.

A banca examinadora foi composta por:

Dr. Thomas Fauster, presidente (Universität Erlangen-Nürnberg)
Dr. Ulrich Heber (Universität Erlangen-Nürnberg)
Dra. Katia Cunha (Observatório Nacional)
Dr. Ramiro de la Reza (Observatório Nacional)
Dr. Ulrich Katz (Universität Erlangen-Nürnberg)
Dr. Keith Butler (Ludwig-Maximilians-Universität München)

Os referees da Tese foram:

Dr. Ulrich Heber
Dra. Katia Cunha
Dr. Klaus Werner (Universität Tübingen)

Dedicated to my parents, Graciela I. Russo and Felipe J. Nieva,
who gave me the freedom to choose my own path in life.

Dedicado a mis padres, G.I.R y F.J.N., quienes me dieron
la libertad de elegir mi propio camino en la vida.

Resumo

Determinações precisas da composição química de estrelas OB constituem vínculos observacionais fundamentais para a evolução estelar e evolução química da Galáxia. Dentre os elementos leves, o carbono é um dos metais mais abundantes no Universo mas a sua análise em estrelas jovens apresentou resultados não-conclusivos nas últimas décadas. Na vizinhança solar, as abundâncias de carbono obtidas principalmente para estrelas OB não evoluídas apresentam um grande espalhamento - com mais de uma ordem de magnitude - e o seu valor médio é sistematicamente mais baixo do que aquele obtido para estrelas FG (incluindo o Sol) e regiões H II. Ambos os resultados não podem ser explicados em termos da evolução estelar e da evolução química da Galáxia. A análise espectral deste tipo de estrelas também apresenta abundâncias discrepantes a partir de diferentes linhas de C II e falha ao estabelecer o equilíbrio de ionização C II/III.

Por outro lado, linhas espectrais de hidrogênio e hélio são ferramentas de diagnóstico cruciais para a análise quantitativa de estrelas OB, uma vez que elas são indicadores primários para a determinação de parâmetros atmosféricos fundamentais, isto é, a temperatura efetiva e a gravidade superficial. A análise cuidadosa destes parâmetros fornece a base para o estudo posterior de abundâncias de metais. Cálculos de formação de linhas em não-ETL para estes elementos, com uma abordagem híbrida, ainda não foram discutidos completamente até o momento, apesar desta abordagem ser amplamente adotada em análises de linhas metálicas.

Inicialmente, espectros sintéticos de hidrogênio e hélio são calculados com base na abordagem híbrida não-ETL a fim de testar a capacidade destes modelos de reproduzir espectros de alta resolução e alta razão sinal/ruído de estrelas OB anãs e gigantes. Modelos atômicos e teorias de alargamento de linhas modernos são empregados para modelar os espectros de H e He I/II. Os espectros sintéticos híbridos não-ETL ajustam simultaneamente quase todas as linhas mensuráveis de H e He observadas nos espectros de seis estrelas usadas como teste, em um grande intervalo espectral, do limite da série de Balmer até o infravermelho próximo.

Comparações das estruturas atmosféricas e dos espectros sintéticos de H e He com modelos não-ETL já publicados e que incluem obscurecimento por linhas demostram que a aproximação ETL é apropriada para modelar a estrutura atmosférica de estrelas OB anãs e gigiantes com metalicidades de até 1/5 do valor solar. Esta abordagem evita inconsistências na modelagem dos singletos do He I encontradas em outros resultados em não-ETL publicados na literatura. Também supera os modelos ETL puros – amplamente aplicados na análise de estrelas OB – em muitos aspectos: o aumento da intensidade das linhas calculadas em não-ETL e o uso de dados detalhados de alargamentos de linhas resultam em diferenças significativas tanto nos perfis de linhas como nas larguras equivalentes das linhas de Balmer de do hélio. Efeitos sistemáticos na determinação dos parâmetros

estelares são quantificados. Um procedimento incial confiável para estudos de espectros de metais é estabelecido.

Em seguida, um modelo detalhado e robusto para C II-IV para cálculos de formação de linhas em não-ETL é apresentado. O modelo é baseado em dados atômicos selecionados cuidadosamente em uma calibração empírica. Uma análise espectral quantitativa auto-consistente é realizada usando um esquema iterativo para determinar os parâmentos atmosféricos estelares com grande acurácia e para selecionar os dados atômicos apropriados para o cálculo das abundâncias. O equilíbrio de ionização do carbono é estabelecido com sucesso com um único conjunto de dados atômicos para todas as estrelas da nossa amostra, que cobre um grande intervalo de parâmetros. A consistência é atingida para um grande número de linhas de carbono - em um total de 40. Isto inclui, em particular, perfis mais intensos que são de grande importância para aplicações extra-galácticas. O duradouro problema de inconsistências na determinação das abundâncias de carbono a partir de diferentes linhas e estágios de ionização é resolvido.

A análise auto-consistente permite definir parâmetros atmosféricos e abundâncias de carbono com acurácia sem precedentes, com incertezas da ordem de 1% na temperatura efetiva, 10% na gravidade superficial e 20% na abundância de carbono, com reduzidos erros sistemáticos. Isto é significativamente melhor do que os resultados de estudos anteriores, que tipicamente apresentam incertezas de 5-10%, $\sim$25% e um fator de $\sim$2-3, respectivamente.

Além disso, uma abundância extremamente homogênea de $\log(\mathrm{C/H})+12 = 8.32 \pm 0.04$ é obtida para as estrelas da nossa amostra. Este resultado estabelece a abundância de carbono atual em estrelas da vizinhança solar como sendo $\log(\mathrm{C/H})+12 \simeq 8.35 \pm 0.05$, após pequenos ajustes de $< +0.05$ dex por estrela, devido a efeitos evolutivos. Este resultado está em acordo com o valor solar revisto recentemente e com a abundâncias nebulares na região H II de Orion.

A abordagem apresentada aqui permite que os efeitos de erros sitemáticos nos parâmetros fundamentais e nas abundâncias sejam estabelecidos. Isto sugere que muitas das dificuldades encontradas em trabalhos anteriores podem estar relacionadas com grandes efeitos sistemáticos na análise causados por incertezas nos dados atômicos e/ou na determinação dos parâmetros atmosféricos.

A obtenção de um valor homogêneo para a abundância de carbono atual na vizinhança solar concorda com análises do meio interestelar e também com previsões de modelos de evolução química da Galáxia. A grande acurácia alcançada aqui é um pré-requisito para a determinação do gradiente Galáctico de abundâncias, que é da ordem das incertezas atuais (em contraste com um espalhamento em abundâncias da ordem de uma magnitude encontrado em estudos anteriores). Modelos de evolução estelar e de evolução química da Galáxia podem assim ser vinculados mais fortemente com abundâncias de carbono confiáveis. Isto pode ser feito em ambientes de diferentes metalicidades (i.e., galáxias) com limitações definidas apenas pela qualidade dos espectros estelares.

Zusammenfassung

Unser Verständnis der Entwicklung der Sterne und der Galaxien ruht auf der empirischen Bestimmung der chemischen Zusammensetzung von Sternen und Gasnebeln. Um die heute vorherrschenden Elementhäufigkeiten zu ermitteln, spielen die Sterne des Spektraltyps OB eine herausragende Rolle, da sie sehr junge Objekte sind. Kohlenstoff ist unter den leichten Elementen eines der häufigsten Metalle. Allerdings liefern die bisherigen Analysen des Kohlenstoffspektrums widersprüchliche Ergebnisse.

Die Sonnenumgebung ist das am besten untersuchte Himmelsareal. Hier zeigt sich, dass die Kohlenstoffhäufigkeit bei den jungen, unentwickelten OB-Sternen im Mittel niedriger ist als bei älteren Sternen des Spektraltyps F und G (einschließlich der Sonne) und bei Gasnebeln (H II-Regionen). Ebenfalls weisen die Kohlenstoffhäufigkeiten von OB-Sternen eine große Streuung von bis zu einer Größenordnung auf. Dies kann weder im Rahmen der Theorie der Sternentwicklung noch der Galaxienentwicklung verstanden werden. Bemerkenswert ist darüberhinaus, dass in vielen Analysen weder die Häufigkeiten aus verschiedenen Linien des einfach ionisierten Kohlenstoffs, C II, miteinander in Einklang zu bringen sind, noch dass das Ionisationsgleichgewicht von C II/III eingestellt werden kann.

Wasserstoff und Helium spielen für die quantitative Spektralanalyse von OB-Sternen, wie in fast allen astronomischen Objekten, eine wichtige Rolle. Sie werden zur Bestimmung der fundamentalen atmosphärischen Parameter, d.h. der Effektivtemperatur und der Schwerebeschleunigung, genutzt. Ohne die genaue Kenntnis dieser Parameter können die Häufigkeiten der Metalle nicht zuverlässig bestimmt werden. Die hier benutzte Analysetechnik, die Spektrumssynthese mittels sogenannter hybriden non-LTE Rechnungen, ist bisher noch nie sorgfältig für Wasserstoff- und Heliumlinien diskutiert worden, obwohl sie für Metalllinien weit verbreitet ist.

Im ersten Arbeitsschritt werden hybride non-LTE Rechnungen für Wasserstoff sowie für neutrales und einfach ionisiertes Helium durchgeführt. Die synthetischen Spektren werden anhand von erstklassigem Beobachtungsmaterial, hochaufgelösten, nahezu rauschfreien Spektren von sechs Zwerg- und Riesensternen der Spektraltypen O und B, getestet. Dabei werden die zur Zeit besten Modellatome und Linienverbreiterungstabellen berücksichtigt. Die Ergebnisse sind sehr überzeugend, denn es gelingt praktisch alle meßbaren Wasserstoff- und Heliumlinien über den gesamten Spektralbereich vom Balmersprung bis ins Nahinfrarote konsistent zu reproduzieren.

Die Verlässlichkeit der Methode wird durch Vergleich mit publizierten non-LTE Modellen verifiziert. Die Annahme des lokalen thermodynamischen Gleichgewichts erweist sich als völlig ausreichend, um die Druck- und Temperaturschichtung der Atmosphäre korrekt wiederzugeben. Dies gilt unabhängig vom Metallgehalt bis hinunter zu einem fünftel der solaren Metallizität. Es wird gezeigt, dass der gewählte Ansatz Inkonsistenzen beim He I Singlettsystem vermeidet, die in anderen non-LTE Rechnungen auftreten. Im Vergleich zu LTE-Analysen, die immer noch weit verbreitet weil einfacher auszuführen sind, lassen sich systematische Abweichungen bei der Bestimmung der atmosphärischen Parameter quantifizieren. Ein verlässlicher Ausgangspunkt für die Analyse der Metalllinenspektren wurde gefunden.

Im zweiten Arbeitsschritt wird ein umfassendes und robustes Modellatom für Kohlenstoff entwickelt, das die Ionisationsstufen C II–C IV berücksichtigt. Es basiert auf sorgfältig überprüften atomaren Daten und wurde anhand von beobachteten Spektren kalibriert. Für die selbstkonsistente quantitative Spektralanalyse wird ein umfangreiches Iterationsschema ausgearbeitet, um die atmosphärischen Parameter noch genauer zu bestimmen und geeignete Atomdaten zu selektieren. Das Ionisationsgleichgewicht des Kohlenstoffs lässt sich mit dem kalibrierten Modellatom zwanglos einstellen. Ebenfalls werden übereinstimmende Kohlenstoffhäufigkeiten aus insgesamt 40 Spektrallinien abgeleitet. Dabei ist besonders bemerkenswert, dass auch die stärksten Absorptionslinien reproduziert werden, die bei extragalaktischen Sternen von großer Bedeutung sind, da schwächere Linien in diesen Objekten nicht meßbar sind. Der gleiche Befund ergibt sich bei allen sechs Programmsternen, obwohl sie einen weiten Bereich von Effektivtemperaturen und Schwerebeschleunigungen überdecken. Damit kann das alte Problem der widersprüchlichen Häufigkeiten aus verschiedenen Linien des einfach ionisierten Kohlenstoffs und des Ionisations-Ungleichgewichts als gelöst angesehen werden.

Die Früchte der Bemühungen um größtmögliche Genauigkeit werden nach der Fehleranalyse deutlich. Mit $\sim$1% bei der Effektivtemperatur und $\sim$10% bei der Schwerebeschleunigung sind die Parameter weit genauer bestimmt als üblich (5-10% bzw. $\sim$25%). Dies setzt sich bei den Kohlenstoffhäufigkeiten fort, bei denen bisher nie dagewesene $\sim$20% erreicht werden, während bei den meisten publizierten Analysen Fehler von Faktoren 2 bis 3 nicht ungewöhnlich sind.

Vergleicht man die Programmsterne miteinander, fällt die große Homogenität der Kohlenstoffhäufigkeit auf. Die mittlere Häufigkeit aller sechs Programmsterne ist $\log(\mathrm{C/H}) + 12 = 8.32$ mit einer sehr geringen Streuung von 0.04. Berücksichtigt man noch kleine Entwicklungseffekte ($<$0.05 dex) so ergibt sich die heutige Kohlenstoffhäufigkeit in der Sonnenumgebung zu $\log(\mathrm{C/H}) + 12 = 8.35$ $\pm$0.05 in guter Übereinstimmung mit den jüngsten Resultaten für die Sonne und für den Orionnebel. Die Ergebnisse der Analyse legen nahe, dass die Ungereimtheiten und Widersprüche vieler publizierter Analysen auf unterschätzte systematische Effekte in den Spektralanalysen zurückzuführen sind, die wiederum

aus Ungenauigkeiten bei den Atomdaten und/oder der atmosphärischen Parameter herrühren.

Die hier erzielten Analyseergebnisse stehen im Einklang mit den Vorhersagen galakto-chemischer Entwicklungsmodelle. Geht man über die Sonnenumgebung hinaus, sind galaktische Häufigkeitsgradienten zu erwarten. Die hohe Genauigkeit der gegenwärtigen Analysen ist unabdingbare Voraussetzung, um solche Gradienten zu vermessen, die nach Vorhersagen von Entwicklungsmodellen klein sein sollten. Die große Streuung alter Resultate erlaubte bisher keine überzeugenden Schlußfolgerungen zu treffen.

Mit der hier entwickelte Analysemethodik für Kohlenstoffhäufigkeiten werden künftig Modelle für die Sternentwicklung wie auch für die chemische Entwicklung von Galaxien sehr viel genauer als bisher überprüft werden können. Dies kann auf Umgebungen sehr unterschiedlicher Metallizität ausgedehnt werden, z.B. in anderen Galaxien, beschränkt nur durch die Qualität des Beobachtungsmaterials.

Abstract

Precise determinations of the chemical composition of OB-type stars constitute fundamental observational constraints to stellar and galactochemical evolution. Among the light elements, carbon is one of the most abundant metals in the Universe but analyses in early-type stars showed inconclusive results in the past decades. In the solar vicinity, carbon abundances derived from mostly unevolved OB stars indicate a large scatter – by more than one order of magnitude – and the mean value is systematically lower than those derived from FG-type stars (including the Sun) and H II regions. Both results cannot be explained in terms of stellar evolution and chemical evolution of the Galaxy. Spectral analyses of this kind of star also give largely discrepant abundances from different C II lines and fail to establish the C II/III ionization balance.

On the other hand, hydrogen and helium line spectra are crucial diagnostic features for the quantitative analysis of OB stars as they are primary indicators for deriving the fundamental atmospheric parameters, i.e. the effective temperature and the surface gravity. Their careful analysis provides the basis for any further study of metal abundances. Hybrid non-LTE line-formation calculations for these elements have not been discussed thoroughly so far, despite a wide use of this approach for analyses of metal line spectra.

In a first step, synthetic spectra of hydrogen and helium are computed on the basis of a hybrid non-LTE approach in order to test the ability of these models to reproduce high-resolution and high-S/N spectra of dwarf and giant OB stars. State-of-the-art model atoms and line-broadening theories are employed to model the H and He I/II spectra. The present hybrid non-LTE synthetic spectra match simultaneously almost all measurable hydrogen and helium lines observed in six test stars over a wide spectral range from the Balmer limit to the near-infrared.

A comparison of atmospheric structures and synthetic spectra of H and He with published line-blanketed non-LTE models validates the suitability of the LTE approximation for modelling the atmospheric structure of dwarf and giant OB stars at metallicities down to (at least) $1/5 \times$ solar. The present approach avoids inconsistencies in the modelling of the He I singlets found in other published non-LTE calculations. It improves on pure LTE models – widely applied for OB star analyses – in many aspects: non-LTE strengthening and the use of detailed line-broadening data result in significant differences in the line profiles and equivalent widths of the Balmer and helium lines. Systematic effects on the stellar parameter determination are quantified. A reliable starting point for studies of the metal spectra is established.

In a second step, a comprehensive and robust C II-IV model for non-LTE line-formation calculations is presented. The model is based on atomic data carefully selected in an empirical calibration. A self-consistent quantitative spectrum analysis is performed using an extensive iteration scheme to determine stellar atmospheric parameters with improved accuracy and to select the appropriate atomic data to be used for the derivation of abundances. The carbon ionization balance is successfully established with a unique set of input atomic data for all sample stars, which cover a wide parameter range. Consistency is achieved for a large number of carbon lines – in total 40. This includes in particular the strongest features that are of highest importance for extragalactic applications. The long-standing problem of inconsistencies in the determination of carbon abundances from different lines and ionization stages is solved.

The self-consistent analysis provides atmospheric parameters and carbon abundances with unprecedented accuracy, with uncertainties as low as $\sim$1% in effective temperature, $\sim$10% in surface gravity and $\sim$20% in carbon abundance, with reduced systematic error. This improves significantly on results from previous studies, which typically give uncertainties of 5-10%, $\sim$25% and a factor $\sim$2-3, respectively.

Moreover, an extremely homogeneous abundance of $\log(\mathrm{C/H}) + 12 = 8.32 \pm 0.04$ is derived from the star sample, This result constrains the present-day stellar carbon abundance in the solar neighbourhood to $\log(\mathrm{C/H}) + 12 \simeq 8.35 \pm 0.05$, after small adjustments by $< +0.05$ dex per star for evolutionary effects. This is in agreement with the recently revised solar value and with the gas-phase abundance of the Orion H II region.

The approach presented here allows the effects of systematic errors on fundamental parameters and abundances to be constrained. This suggests that most of the difficulties found in previous work may be related to large systematic effects in the analysis caused by inaccuracies in the atomic data and/or the atmospheric parameter determination.

The finding of a homogeneous present-day carbon abundance in the solar vicinity conforms with analyses of the interstellar medium and also with predictions of chemical-evolution models for the Galaxy. The high accuracy achieved here is a prerequisite for the determination of the Galactic abundance gradient, which is of the order of the present uncertainties (in contrast to an overall abundance scatter of one order of magnitude found in previous studies). Stellar and galactochemical evolution models can from now on be constrained more tightly with reliable carbon abundances. This can be done for environments of different metallicities (i.e. galaxies), with the only remaining limitation being the quality of the observed stellar spectra.

Contents

Chapter 1

Introduction (in Portuguese)

As estrelas de tipo espectral 'O-late' e de tipo espectral 'B-early' pertencem a um subgrupo que é comumente conhecido como estrelas OB (Jaschek & Jashek 1990). Tais estrelas são jovens (com idades entre 10^6 e 10^7 anos), massivas (com massas entre aproximadamente 9 e 20 $M_\odot$) e também luminosas (com luminosidades entre 10^4 e 10^6 $L_\odot$). Em nossa Galáxia, a via Láctea, a maioria destas estrelas jovens encontra-se em associações OB localizadas nos braços espirais da Galáxia. São objetos de interesse para este trabalho de tese, a maioria das estrelas OB não evoluídas que encontram-se ainda na sequência principal (estrelas anãs); assim como estrelas mais evoluídas já na fase gigante da evolução estelar.

As estrelas massivas são os principais propulsores da evolução química e dinâmica do meio interestelar ('MI'), e consequentemente da evolução das galáxias como um todo. Tais estrelas contribuem de modo decisivo para o conteúdo global de energia e momento do MI, sendo fonte de radiação ionizante no ultra-violeta, através de seus ventos estelares e ao explodirem como supernovas em sua fase final de evolução. No que concerne a evolucão química galáctica (modelos de Hou et al. 2000; Chiappini et al. 2001; 2003), as estrelas OB são vínculos importantes, por representarem a composição química da Galáxia no tempo presente. Adicionalmente, estas estrelas fornecem também informações sobre a variação espacial das abundâncias dos elementos químicos na vizinhança solar, assim como em regiões galáticas mais distantes, o que permite a determinação de gradientes de metalicidade ao longo do disco da Galáxia (p.e. Gummersbach et al. 1998; Rollerston et al. 2000; Daflon & Cunha 2004). As referidas abundâncias que são obtidas para estas estrelas jovens servem também como um dado complementar para os resultados de abundância que são obtidos através dos estudos de regioes H II; dado que ambas as populações representam o estado presente da nucleosíntese de metais no ciclo cósmico da matéria. Com o advento da geração moderna de grandes telescópios equipados com espectrógrafos de alta-resolução abundâncias 'primordiais' podem ser obtidas não somente para estrelas de tipo 'early-type' de nossa Galáxia, assim como também podem ser estudados objetos nos ambientes de mais baixa metalicidade das Nuvens de Magalhães (p.e., Korn

et al. 2002; 2005; Rolleston et al. 2003; Hunter et al. 2007). Tais estudos podem até ser estendidos para galáxias mais distantes do grupo local, e mesmo para além do grupo local, analisando-se espectros de resolução intermediária de estrelas supergiantes do tipo 'early-type' (e.g. Trundle et al. 2002; Urbaneja et al. 2005 a,b).

Adicionalmente, as abundâncias dos elementos carbono, nitrogênio e oxigênio obtidas através de análises quantitativas de espectros de estrelas massivas de tipo 'early-type' servem também como condições de contorno observacionais para modelos de evolução estelar. Informações sobre os parâmetros estelares básicos juntamente com as determinações dos padrões de abundância dos elementos leves resultantes da mistura com material processado nuclearmente, permite uma avaliacão empírica dos diferentes modelos evolutivos (p.e. Heger & Langer 2000; Maeder & Meynet 2000).

A precisão atingida nas determinações das abundâncias dos elementos define em última análise o grau com que uma teoria pode ser testada. Entretanto, vale lembrar que a espectroscopia quantitativa baseia-se em várias hipóteses. Em particular, é necessário se ter uma comprensão detalhada dos processos de interação entre o campo radiativo e o plasma da atmosfera estelar. Qualquer debilidade no modelo físico adotado acaba limitandoo a relevância de uma análise, mesmo que a observações sejam de muito alta qualidade e que a redução dos dados tenha sido efetuada de forma ideal.

Para que as abundâncias estelares tenham associadas a elas um verdadeiro significado, as determinações dos parâmetros estelares para os objetos individuais estudados não podem ser afetadas por erros sistemáticos significativos. As estrelas de tipo espectral O 'early' e O 'medio' apresentam dificuldades consideráveis em suas análises de modelos de atmosferas devido, por exemplo, à efeitos como esfericidade, perda de massa, além de efeitos de bloqueamento / obscurecimento por linhas em não-ETL (equilibrio termodinâmico não local). Por estas razões as estrelas massivas OB de menor luminosidade tem sido os principais objetos dos estudos de abundâncias estelares durante longo tempo (p.e. Gies & Lambert 1992; Kilian 1992; Cunha & Lambert 1992; e numerosos estudos similares desde então). De um modo geral, as atmosferas das estrelas anãs e gigantes do tipo OB são supostamente razoavelmente bem descritas por modelos de atmosferas em ETL (equilibrio termodinâmico local) em uma dimensão, plano paralelos, homogêneos e hidrostáticos, com blanketing das linhas e que assumem a validade do equilibrio radiativo . No entanto, estas simplificações nao implicam em que as análises quantitativas de estrelas OB anãs e gigantes sejam triviais.

O elementos hidrogênio e hélio são de maior interesse neste contexto astrofísico, já que estes constituem praticamente todo o plasma emissor de luz. As transições de H e He são as linhas mais fortes que encontram-se presentes nos espectros das estrelas OB. Enquanto estes perfis de linhas constituem-se nas principais ferramentas para diagnósticos em análises estelares ao longo do diagrama HR, estas medem também as condições físicas do plasma em grandes extensões ao

longo das atmosferas estelares, especialemente quando comparadas às extensões cobertas por linhas metálicas.

A maioria das análises quantitativas de perfis de linhas do H e do He publicadas na literatura seguem dois tipos básicos de metodologia: realiza-se uma análise baseada em tratamentos puramente em ETL (p.e. Rolleston et al. 2000 e referências incluídas); ou bem, se resolve o problema em não-ETL restrito adotando-se modelos de atmosferas em ETL, que incluem o 'blanketing' das linhas. Para as estrelas discutidas neste trabalho, um teste completo dos modelos, no que concerne a reprodução de espectros do H e do He (via comparações diretas com observações no visível e infravermelho próximo, e cobrindo um intervalo grande de parametros) não encontra-se publicado na literatura (note que estes existem para as estrelas O pelo menos para alguns grupos de linhas: Bouret et al. 2003; Repolust et al. 2004; 2005; Mokien et al. 2005, 2006; Heap et al. 2006). A disponibilidade de tais testes ajudaria ao usuário de redes de espectros sintéticos publicadas na literatura a compreender suas limitações e pontos fortes. Usualmente, somente uma ou duas linhas de Balmer de hidrogênio e algumas linhas selecionadas de He, no ótico azul, são consideradas em estudos da literatura.

Dentre os metais, o elemento carbono tem um importante papel porque este é o elemento principal criado no processo triplo-alfa e assim sendo, servindo como sementes para a síntese subsequente de todos os elementos mais pesados (Burbidge et al. 1957; Cameron 1957). O carbono é um catalisador para a transformação de hidrogênio em hélio através do ciclo CNO em estrelas massivas e de massa intermediária e este elemento também constitui a base de toda a química orgânica. As abundâncias de carbono derivadas em estrelas 'early-type' tem sido o objeto de inúmeros estudos ao longo das últimas décadas, com crescentes melhoramentos na qualidade dos dados observacionais, e na complexidade e consistência atingida nos cálculos dos modelos e nas análises espectrais. Um passo crucial neste trajeto foi o abandono da aproximação de equilibrio termodinâmico local nos cálculos de formação das linhas, permitindo-se os desvios do ELT (não-ETL). Inúmeros modelos atômicos foram discutidos na literatura (Lenon 1983; Eber & Butler 1988; Grigsby et al. 1992; Sigut 1996; Lanz & Hubeny 2003; 2007). Em particular, o modelo atômico de Eber & Butler tem sido amplamente aplicado em trabalhos de determinação de abundâncias em estrelas O e B, na sua maioria nao evoluídas e da vizinhança solar (e.g. Gies & Lambert 1992; Kilian 1992; Cunha & Lambert 1992; Gummersbach et al. 1998; Daflon et al. 1999; 2001a,b).

Em um número grande de estrelas de tipo 'early-type', principalmente aquelas em meios extra-galáticos e aquelas com altas velocidades projetadas de rotação, apenas um número pequeno de linhas de carbono no ótico podem ser utilizadas em determinações de abundâncias, devido à uma maior dificuldade em se atingir uma boa relação sinal-ruido (S/N) e ao fato de as linhas serem muito alargadas devido a rotação. Isto inclui a forte linha de C II em $\lambda\lambda$ 6578/82Å e, em particular, o multipleto em $\lambda\lambda$ 4267Å, que tem se mostrado tradicionalmente bastante difícil

de ser modelado em cálculos em não-ETL (e.g. Lambert 1993; Sigut 1996). Estes dois multipletos usualmente não reproduzem bem as observações (e.g. Grigsby et al. 1992; Hunter et al. 2007), encontrando-se resultados de abundância sistematicamente mais baixas do que aqueles derivados a partir de outras linhas mais fracas de C II (Gies & Lambert 1992). As linhas de C IIII também pódem ser modeladas inadequadamente (Grigsby et al. 1992). Uma complicação adicional é a impossibilidade de se estabelecer o equilibrio de ionização do C II / C III. Diferenças nas abundâncias obtidas através destes dois ions podem chegar a um fator 5-10 (Daflon et al. 2001b; Hunter et al. 2007). Entretanto, existem inconsistências adicionais entre as abundâncias de carbono em estrelas 'early-type' publicadas na literatura que necessitam de outras explicações, dado que a maioria destes estudos deriva abundâncias de carbono a partir de linhas que não são tão sensíveis a efeitos não-ETL.

Uma comparação entre os resultados de abundância para estrelas de tipo 'early-type' indica que a abundâncias de carbono na vizinhança solar são altamente inomogêneas (mesmo para estrelas em um mesmo aglomerado) e fortemente sub-solares. Tal resultado constrasta-se com a uniformidade encontrada nas abundâncias obtidas para a fase gasosa no meio interestelar dentro de um limite aproximado de 1.5 kpc do Sol (Sofia & Meyer 2001; e referências citadas neste trabalho). Este resultado de inomogeneidade não pode tampoco ser compreendido no contexto dos modelos recentes de evolução química da Galáxia. A expectativa seria que as estrelas massivas e jovens, que se formam a partir de uma nuvem molecular numa curta escala de tempo, apresentem uma abundância de carbono homogênea, coincidindo com os resultados obtidos de regiões H II. Adicionalmente, o valor de abundância deve ser maior do que aquele observado em objetos provenientes de gerações estelares anteriores em sua vizinhança, tal como estrelas de tipo F e G (< 2 Gyr), e também maior que o valor solar. Na realidade, diferenças sistemáticas significativas existem (ver p.e. Sofia & Meyer 2001; Herrero 2003), levantando dúvidas sobre a realidade das abundâncias de carbono derivadas para as estrelas de tipo B.

O objetivo deste trabalho é resolver o problema de abundâncias de carbono não confiáveis obtidas a partir de estrelas de tipo espectral O e B. Com este propósito, melhoramentos na *modelagem* e na *análise quantitativa* dos espectros observados serão realizados. Em um passo preparatório a validade da análise não-ETL híbrida será testada e o status atual dos cálculos da formação das linhas de H e He – os absorventes mais abundantes – será avaliado. Um modelo atômico de C II a C IV será construído e calibrado empiricamente utilizando as observações de seis estrelas de tipo B 'early' da vizinhança solar. Uma ênfase especial será dada a uma avaliação crítica dos dados atômicos de entrada. Os parâmetros atmosféricos fundamentais das estrelas estudadas serão derivados de modo auto-consistente a partir de simultâneos equilibrios de ionização. Este método permite obter abundâncias com acurácia sem precedentes, resultando em uma determinação precisa da abundância presente do carbono na vizinhança

solar. Partes dos resultados apresentados neste trabalho de tese e aplicações adicionais foram publicados, um artigo foi submetido e outros estão em preparação: Korn et al. (2005); Nieva et al. (2003); Nieva & Przybilla (2006ab; 2007 a-d); Przybilla et al. 2006ab).

A tese encontra-se organizada da seguinte forma: no capítulo 2 uma introdução ao modelo de atmosferas estelares e a análise espectral tal como considerada neste trabalho será apresentada. No capítulo 3 os conceitos básicos relativos aos dados atômicos de entrada para a modelagem espectral serão discutidos. No capítulo 4 se apresentará uma breve descrição da análise espectroscópica. No capítulo 5 uma análise do método não-ETL híbrido para a formação das linhas de H e He será apresentada. No capítulo 6 uma calibração auto-consistente e simultânea do modelo de C II-IV e a análise espectral será descrita. Finalmente, as conclusões deste trabalho de tese serão sumarizadas no capítulo 7.

Chapter 2

Model Atmospheres

Almost all physical information of stars has to be inferred from the radiation they emit. The photons escape to space from a medium located in the external layers of the star, called the *stellar atmosphere*. In order to compute the emergent flux of the star, it is necessary to specify the physical conditions under which the radiation is transported. A set of state parameters as function of depth is termed a *model atmosphere*. The list of state parameters will depend on the basic assumptions under which the model is constructed (e.g. temperature, density, etc.). An important component for the construction of the atmospheric structure is the radiation, and its transfer through and interaction with the atmospheric medium is a complex problem to be solved. The emergent spectrum of the star, and in particular the spectral lines, has to be modelled in detail for quantitative analyses by comparison with the observed spectra.

From the pioneering work of Unsöld (1955) enormous progress has been achieved in the field of stellar atmosphere modelling. A detailed theoretical description of stellar atmospheres can be found in the textbook of Mihalas (1978) and a discussion of more recent developments is given in Hubeny (1997). Current realistic models are built on the basis of a well understood underlying physics and they allow the analysis of stellar atmospheres to be performed quantitatively.

Overall, the atmospheres of late O and early B-type (OB) main sequence and giant stars are supposed to be described reasonably well by one-dimensional, plane-parallel, homogeneous and hydrostatic line-blanketed LTE models in radiative equilibrium. However, this does not imply that quantitative analyses of the spectra of OB dwarfs and giants are trivial. Even for a simple approach, like the one employed here, the modelling of the stellar atmosphere is complex and requires the solution of the atmospheric structure equations coupled to the radiative transfer. As a further complication, small discrepancies in the atmospheric structure due to different model assumptions or input parameters can produce large variations of spectral line profiles, and can therefore impact the physical information derived from the observed spectra notably.

Line-blanketed plane-parallel stellar atmospheres in hydrostatic equilibrium are briefly discussed in the present chapter and they are further investigated in Chapter 5. Models for expanding atmospheres and the coupling of the atmosphere with the stellar wind (which describe, e.g. Wolf-Rayet stars or supergiants envelopes) will not be discussed. The readers can refer to the review of Kudritzki & Hummer (1990) and other monographs, e.g. *Stellar Atmospheres: Beyond Classical Models* (Crivellari et al. 1990); *The Atmospheres of Early-Type Stars* (Heber & Jeffery 1992); *Stellar Atmosphere Modeling*, (Hubeny, Mihalas & Werner 2003).

On the other hand, a realistic calculation of spectral line formation considering non-local effects caused by the radiation field is also addressed in the present chapter. In particular, the restricted non-LTE line-formation calculations employed in this work are described. Both the model atmospheres and the line-formation calculation are the basis of any further quantitative spectral analysis that, in order to be meaningful, should be free of systematic errors.

2.1 Radiative Transfer

The radiation field of early-type stars constitutes an important physical property of the atmosphere and, at the same time, its interaction with the medium determines the state of the plasma. The propagation of the photons through the stellar atmosphere is described by the radiative transfer equation, which involves a number of quantities to be defined for the case of a plane-parallel atmosphere (see Sect. 2.2) as follows.

The *specific intensity* I_ν of radiation with frequency ν is defined as the amount of energy transported by the radiation in frequency range $(\nu,\ \nu + \mathrm{d}\nu)$ per unit area $\mathrm{d}S$ into the solid angle $\mathrm{d}\omega$ within a time interval $\mathrm{d}t$

$$\mathrm{d}E = I_\nu \, \mathrm{d}S \cos\theta \, \mathrm{d}\omega \, \mathrm{d}\nu \, \mathrm{d}t, \tag{2.1}$$

where θ is the angle between the direction of propagation and the surface normal. The dimension of I_ν is $\mathrm{erg\,cm^{-2}\,s^{-1}\,hz^{-1}\,sr^{-1}}$ (in cgs units). The specific intensity provides a macroscopic description of the radiation field.

The interaction of the radiation field with matter is described by two phenomenological quantities: the *absorption coefficient* χ_ν and the *emission coefficient* η_ν defined as follows

$$\mathrm{d}E = \chi_\nu \, I_\nu \, \mathrm{d}S \, \mathrm{d}s \, \mathrm{d}\omega \, \mathrm{d}\nu \, \mathrm{d}t, \tag{2.2}$$

$$\mathrm{d}E = \eta_\nu \, \mathrm{d}S \, \mathrm{d}s \, \mathrm{d}\omega \, \mathrm{d}\nu \, \mathrm{d}t. \tag{2.3}$$

In Eqn. (2.2), $\mathrm{d}E$ is the energy absorbed by an element of material of cross-section $\mathrm{d}S$ and length $\mathrm{d}s$, from a beam of specific intensity I_ν (incident normal to $\mathrm{d}S$ into a solid angle $\mathrm{d}\omega$). In Eqn. (2.3), $\mathrm{d}E$ corresponds to the amount of

energy released by the material in form of radiation. The dimension of χ_ν is cm^{-1}, consequently $1/\chi_\nu$ measures the characteristic distance a photon travels between absorption processes: the *photon mean-free path*. On the other hand, the dimension of η_ν is erg $\mathrm{cm}^{-3}\,\mathrm{s}^{-1}\,\mathrm{Hz}^{-1}\,\mathrm{sr}^{-1}$. Numerical values for the absorption and emission coefficients are assigned from a microscopic point of view, and they follow the form

$$\text{absorption coefficient} = \text{number of absorbers} \times \text{atomic cross-section},$$

where the relevant cross-sections are given by atomic physics.

The absorption can be distinguished in two different processes: *true absorption*, where a photon is destroyed and its energy thermalized, and *scattering*, where the photon is absorbed and immediately re-emitted in a different direction at a Doppler-shifted frequency (scattering can occur in bound states, but also free electrons can scatter radiation with the same efficiency at all wavelengths). Therefore, the total absorption coefficient has two components: $\chi_\nu = \kappa_\nu + \sigma_\nu$, where κ_ν is the true absorption and σ_ν the scattering coefficient.

The total continuous 'true' absorption coefficient is the sum of an ionization process where a *bound-free* transition occurs, and a *free-free* transition, where one charged particle is accelerated upon passing close to another charged particle. The remaining possibility is *bound-bound* transitions, which produce spectral lines, also included in κ_ν. In the case of many overlapped and crowded lines, their effect on the continuous spectrum is considerable (see Sect. 2.4). Most of the continuous absorption is due to hydrogen, a direct result of the overwhelming dominance of hydrogen in the chemical composition. Neutral hydrogen is the major source of absorption for the temperatures of OB stars. Both the bound-free and the free-free absorption of hydrogen are important. The ionization limit for principal quantum number $n = 1$ (Lyman limit) is at 912 Å, for $n = 2$ (Balmer limit) is at 3647 Å, etc. In most stars, helium is the next most abundant element after hydrogen, but its electrons are so tightly bound that its contribution to κ_ν becomes important only at higher temperatures, and primarily in the ultraviolet. The excitation energy of the first level is $E_1 = 19.72$ eV and the ionization energies of He I and He II are $\chi_{I1} = 24.59$ eV and $\chi_{I2} = 54.42$ eV, respectively (χ_{I1} corresponds to 504.19 Å and χ_{I2} to 227.82 Å). Because E_1 is so close to χ_{I1}, by the time electrons start populating the excited levels, helium is beginning to ionize. A single-electron ion (He II) behaves similarly to hydrogen, but with energies scaled up and wavelengths scaled down by a factor of four.

In strict thermodynamic equilibrium (TE), the energy removed by matter from the radiation field is in detailed balance with the energy emitted, and from Eqns. (2.2) and (2.3) follows that $\chi_\nu\, I_\nu = \eta_\nu$. In TE, the radiation intensity is

described by the Planck function, $I_\nu = B_\nu$, with

$$B_\nu = \frac{2h\nu^3}{c^2}\frac{1}{\exp(h\nu/kT)-1}. \tag{2.4}$$

This function depends only on the frequency ν and temperature T; h is the Planck constant, k is the Boltzmann constant and c is the speed of light. A consequence of these considerations in TE is *Kirchoff's law*, $\eta_\nu/\chi_\nu = B_\nu$.

Based on the previous definitions, the radiative transfer equation can be defined, for the planar 1-D case, as

$$\mu\frac{\mathrm{d}I_\nu}{\mathrm{d}z} = \eta_\nu - I_\nu\chi_\nu, \tag{2.5}$$

where z is the geometrical coordinate and μ is the directional cosine, defined by $\mu \equiv \cos\theta$. After division by $-\chi_\nu$, it can be written as

$$\mu\frac{\mathrm{d}I_\nu}{\mathrm{d}\tau_\nu} = I_\nu - S_\nu, \tag{2.6}$$

with the *optical depth* τ_ν defined by

$$\mathrm{d}\tau_\nu \equiv -\chi_\nu\,\mathrm{d}z, \tag{2.7}$$

and the *source function* S_ν defined by

$$S_\nu \equiv \eta_\nu/\chi_\nu. \tag{2.8}$$

The optical depth corresponds to the integrated absorptivity of the material along the line of sight and measures the number of photon mean-free paths.

The radiation field can be described in terms of different averages or moments of the specific intensity. The zero-order moment is the *mean intensity* J_ν and corresponds – except for a numerical factor – to the photon energy density

$$J_\nu = \frac{1}{2}\int_{-1}^{1} I_\nu\,\mathrm{d}\mu. \tag{2.9}$$

The first-order moment is defined as the *Eddington flux* H_ν and corresponds to the astrophysical flux ($F_\nu = 4H_\nu$)

$$H_\nu = \frac{1}{2}\int_{-1}^{1} I_\nu\,\mu\,\mathrm{d}\mu. \tag{2.10}$$

The second-order moment K_ν is physically related to the radiation pressure

$$K_\nu = \frac{1}{2} \int_{-1}^{1} I_\nu \, \mu^2 \, \mathrm{d}\mu. \tag{2.11}$$

If the source function is known, the transfer equation (2.6) becomes a linear first-order differential equation with constant coefficients, solved via an integrating factor $\exp(-\tau_\nu/\mu)$. The *formal solution* for the emergent intensity from a semi-infinite atmosphere seen by an external observer ($\tau = 0$) then is

$$I_\nu(0, \mu, \nu) = \int_0^\infty S_\nu(t) \, \exp(-t/\mu) \, \mathrm{d}t/\mu, \tag{2.12}$$

i.e. the source function at every depth point along the line of sight is attenuated (here, t is the optical depth). The emergent intensity has approximately the value of the source function at optical depth unity along the line of sight (see Fig 2.1).

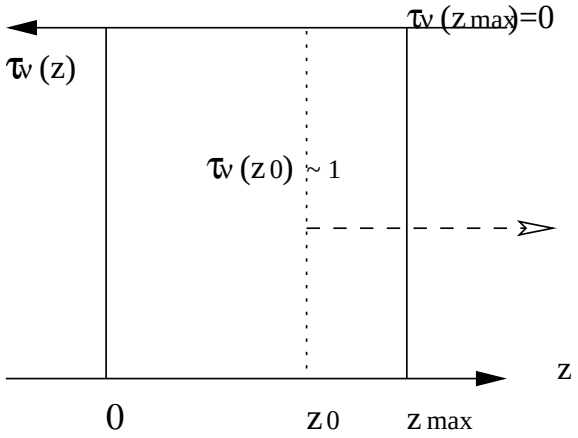

Figure 2.1: In a plane-parallel atmosphere the emergent spectrum at frequency ν is formed in the region around z_0, where the optical depth is $\tau_\nu(z_0) \sim 1$.

For the angle-averaged mean intensity, the formal solution can be expressed as

$$J_\nu(\tau_\nu) = \frac{1}{2} \int_0^\infty S_\nu(t) \, E_1(|t - \tau_\nu|) \, \mathrm{d}t = \Lambda_{\tau_\nu}[S(t)], \tag{2.13}$$

where E_1 is the first exponential integral. In the second expression, the mean intensity is formulated in terms of an operator acting on the source function. This is the so-called Λ-operator. The calculation of this integral has a high computational cost due to E_1. For practical applications, the last equation has to be replaced by a quadrature sum, with the mean intensity and the source function discretised for a number of depth points. The Λ-operator is then expressed in

the form of the Λ-matrix, which describes the coupling of the contributions of the source function from all depth points. In that case, the formal solution can be written as

$$J_d = \sum_{d'}^{D} \Lambda_{dd'}\, S_{d'}, \tag{2.14}$$

where d denotes the depth index.

The following example illustrates the effect of the Λ matrix on the source function. For the simple case where all the elements of the source function vector are zero except for the i-th element, which is taken to be 1, $S_d = \delta_{di}$, then the formal solution reads

$$\begin{bmatrix} J_1 \\ J_2 \\ \vdots \\ J_D \end{bmatrix} = \begin{pmatrix} \Lambda_{11} & \Lambda_{12} & \cdots & \Lambda_{1D} \\ \Lambda_{21} & \Lambda_{22} & \cdots & \Lambda_{2D} \\ \vdots & \vdots & \ddots & \vdots \\ \Lambda_{D1} & \Lambda_{D2} & \cdots & \Lambda_{DD} \end{pmatrix} \times \begin{bmatrix} 0 \\ \vdots \\ 1 \\ 0 \end{bmatrix} = \begin{bmatrix} \Lambda_{1i} \\ \Lambda_{2i} \\ \vdots \\ \Lambda_{Di} \end{bmatrix}, \tag{2.15}$$

In this case, the i-th column of the Λ matrix is a solution of the transfer equation with the source function given as a unit pulse function. Physically, the source function $S = S_i = 1$ at depth point i of the atmosphere is re-distributed over all depth points. In practice, the problem is much more complex, since the source function is not known a priori, and it also depends non-linearly on the intensity.

An iteration scheme can be used to solve the transfer problem, the so-called Λ-*iteration*. Starting from a first estimate of the source function (for instance, equal to the Planck function), the radiation field is computed by solving the transfer equation. The radiation field is in turn employed to compute a new source function, and this procedure can be iterated until some convergence criterion is achieved. Nevertheless, in practical applications the Λ-*iteration* fails to converge. Photons emitted in the wings of a line can travel large distances through the medium before being absorbed and thus can transport information about inhomogeneities (for example the existence of an outer boundary), whereas photons in the line core can travel only comparatively very short distances and are essentially trapped at the place of their formation. Although the latter constitute the majority of all photons in the line, the line source function nevertheless can respond quickly to inhomogeneities. This is because of the large number of interactions which redistribute absorbed photons over the line profile and thus convert a core photon into a wing photon in a short time. By doing a Λ-iteration, we follow this process from scattering to scattering and finally need as many iterations as necessary to give each core photon a chance to be emitted into the wing at least once (or to be destroyed in a thermalisation process). This involves a large number of iterations which prevents the applicability of the Λ-procedure. Therefore other algorithms have to be considered.

Deep in the stellar atmosphere, the source function approaches to the Planck function: $S_\nu \rightarrow B_\nu$, as practically no photons escape, and thus the medium is close to TE. Under these conditions, the transfer problem can be expressed in terms of a diffusion process (see Mihalas 1978). The total radiation flux in the diffusion approximation is proportional to the temperature gradient and an averaged opacity, defined by the *Rosseland mean opacity*

$$\frac{1}{\chi_R}\frac{\mathrm{d}B}{\mathrm{d}T} = \int_0^\infty \frac{1}{\chi_\nu}\frac{\mathrm{d}B_\nu}{\mathrm{d}T}\,\mathrm{d}\nu. \tag{2.16}$$

The importance of the Rosseland opacity lies in the fact that it yields the exact total radiation flux at large depths and therefore the correct temperature structure. Integration of χ_R over the geometrical distance gives the *Rosseland optical depth* τ_R.

The general problem of radiative transfer involves the coupling of physical variables (depths, frequencies, angles) which numerically means inverting large matrices. Several methods have been developed in order to solve the radiation transfer problem numerically as can be found in Mihalas (1978) and in the overview of Hubeny (1997). They are not only aimed at the problem of model atmospheres but also to the line-formation calculations, with an additional coupling of source functions in different transitions via the statistical equilibrium condition, when local detailed balance is no longer valid (Sect. 2.5.2).

Currently, the most powerful techniques are the *Accelerated Lambda Iteration* (ALI) methods, reviewed by Hubeny (1992). The basic concept is to realise that some part of the physical coupling in the radiation transfer problem is more important than others. Cannon (1973) introduced the method of *operator splitting* into astrophysical radiative transfer. The idea consists of writing

$$\Lambda = \Lambda^* + (\Lambda - \Lambda^*), \tag{2.17}$$

where Λ^* is an appropriately chosen *approximate lambda operator*. The choice of Λ^* is arbitrary. From mathematical principles it can be shown that the diagonal of the true Λ-operator is the optimum choice for a local Λ^*, while when considering nearest-neighbour interactions the tridiagonal operator can be chosen. The mean intensity resulting from the i-th iteration is then

$$J^i = \Lambda^* S^i + (\Lambda - \Lambda^*) S^{i-1}. \tag{2.18}$$

The action of the Λ-operator splits into two contributions: the approximate Λ^*-operator acts on the source function of the current iteration, describing the (slowly converging) local absorption and emission processes. The difference between the exact and the approximate operator $\Lambda - \Lambda^*$ acts on the previous, known, iterate

of the source function, accelerating the convergence.

The ALI approach was addressed in several studies and implemented in the numerical computation of the radiative transfer. The ALI approach for solving the non-LTE line-formation problem, as in this work, was first used by Werner & Husfeld (1985). The preferred recipe for the realisation of the ALI scheme for numerical radiative transfer of multilevel atoms was developed in the study of Rybicki & Hummer (1991). This is the formulation implemented in the numerical codes used in the course of the present work (See Sect. 2.5.2).

2.2 Classical Stellar Atmospheres

The *classical stellar atmosphere problem* can be described by a horizontally-homogeneous, plane-parallel and static atmosphere. This model is applicable to the so-called *stellar photosphere*, constrained to a thin layer and not significantly affected by outer layers where a stellar wind may play an important rôle. Here, the basic assumptions and equations are described.

Plane-Parallel Geometry and Homogeneity. The thickness of the atmosphere is small compared to the radius of the star and it is described well by a plane-parallel geometry. The atmosphere consists of horizontally homogeneous layers (without spots, granulations, etc.). Only one variable is therefore needed to specify a given position in the atmosphere. For an observer the optical depth is zero at the surface and increases into the atmosphere.

Stationarity. It is assumed that no phenomena depending on time such as pulsations or variable magnetic fields are present in the atmosphere. The transfer equation and the populations of atomic levels have to be constant in time.

Hydrostatic Equilibrium. This condition requires that at each point of the atmosphere the weight of the overlying layers is supported by the total pressure.

The hydrostatic equilibrium equation can be written as:

$$\frac{\mathrm{d}P}{\mathrm{d}z} = -\rho\,(g - g_{\mathrm{rad}}), \tag{2.19}$$

where P is the total pressure, ρ the mass density, g the surface gravity and g_{rad} the radiative acceleration, defined by $g_{\mathrm{rad}} = \frac{4\pi}{c}\int_0^\infty \chi_\nu H_\nu \,\mathrm{d}\nu$. The radiative acceleration in the stars of interest here (main sequence and giant stars) is small compared to the surface gravity.

Radiative Equilibrium. All the energy released by nuclear reactions in the stellar interior is carried through the stellar atmosphere by radiation. This is equivalent to the conservation of radiative flux:

$$\int_0^\infty H_\nu \,\mathrm{d}\nu = \text{const.} = \frac{\sigma}{4\pi} T_{\mathrm{eff}}^4, \tag{2.20}$$

where σ is the Stefan-Boltzmann constant and $T_{\rm eff}$ is the *effective temperature*. Applying the radiative transfer equation, the latter can be written as follows:

$$\int_0^\infty (\kappa_\nu J_\nu - \eta_\nu)\,\mathrm{d}\nu = \int_0^\infty \kappa_\nu\,(J_\nu - S_\nu)\,\mathrm{d}\nu = 0 \tag{2.21}$$

Here, only true absorption processes enter the energy balance of the medium (κ_ν instead of χ_ν) because scattering contributions to the absorptivity and emissivity cancel.

Charge conservation. This condition expresses the global electric neutrality of the medium of a certain elemental composition,

$$\sum_i n_i Z_i - n_e = 0, \tag{2.22}$$

where Z_i is the charge associated to the level i, which equals 0 for levels of neutral species, 1 for those of a singly-ionized species, etc. The summation extends over all levels of all ions of all chemical species.

2.3 Thermodynamic State: LTE vs. Non-LTE

Two different assumptions can be considered concerning the thermodynamic state of the atmospheric medium: *local thermodynamic equilibrium* (*LTE*) or departures from it (*non-LTE*). LTE is very restricted but offers an analytical description of the source function, while non-LTE is more realistic but its numerical solution might be computationally intensive.

LTE. The statistical physics description of the properties of a medium is enormously simplified when thermodynamic equilibrium is achieved. In such a case, the particle velocity distributions and the distributions of atoms over ionization and excitation states are specified by only two thermodynamic variables. In the stellar atmosphere context these variables are chosen to be the absolute temperature T and the total particle number density N, or the electron number density n_e. The assumption of TE cannot be applied to the whole stellar atmosphere, as the stars emit radiation. However, the standard thermodynamic relations can be applied locally assuming that each individual volume element of the atmosphere is in thermodynamic equilibrium (in plane-parallel geometry this assumption is applied for each layer). This concept is called *local thermodynamic equilibrium*. Following this approximation, the equilibrium values of distribution functions are assigned only to massive particles, but the radiation field is allowed to depart from a Planckian character. The local kinetic temperature determines both the velocity distribution of the particles, which is therefore Maxwellian, and the distribution of the particles through their various ionization and excitation stages

by means of the Saha-Boltzmann equations, defined as follows.

The Maxwellian velocity distribution of particles is given by

$$f(v)\,\mathrm{d}v = (m/2\pi kT)^{3/2}\exp(-mv^2/2kT)\,4\pi v^2\,\mathrm{d}v, \tag{2.23}$$

where k is the Boltzmann constant, v the velocity and m the particle mass.

The Boltzmann excitation formula reads

$$(n_j/n_i) = (g_j/g_i)\exp(-(E_j - E_i)/kT), \tag{2.24}$$

where n_i is the occupation number density, g_i the statistical weight, E_i the energy of the level i and $(E_j - E_i) = h\,\nu_{ij}$ measures the frequency of the transition $i \rightarrow j$. The occupation number density is often termed as the atomic *level population* and refers to the number density of ions in the excited level i.

The Saha ionization equation reads

$$\frac{N_I}{N_{I+1}} = n_e\frac{U_I}{U_{I+1}}CT^{-3/2}\exp(\chi_I/kT), \tag{2.25}$$

where N_I is the total number density of the ionization stage I, χ_I is the ionization potential of the ion I, $U = \sum_1^{i_{\max}} g_i\exp(-E_i/kT)$ is the partition function, and $C = (h^2/2\pi mk)^{3/2}$ is a constant ($= 2.07 \times 10^{-16}$ in cgs units).

The last three equations describe the LTE state macroscopically. From a microscopic point of view, LTE holds if all atomic processes are in *detailed balance* (i.e. if every process is exactly balanced by its inverse).

Non-LTE. Any state departing from LTE is denoted as being in non-LTE. This means that the populations of some energy levels of some atoms/ions may depart from their LTE values, while the velocity distribution of all particles remain Maxwellian, with the same kinetic temperature T. In this case, the Saha-Boltzmann equations have to be replaced by more general equations accounting for the detailed atomic processes which populate/depopulate the energy levels: these are the statistical equilibrium or rate equations,

$$n_i\sum_{j\neq i}(R_{ij} + C_{ij}) = \sum_{j\neq i} n_j(R_{ji} + C_{ji}), \tag{2.26}$$

where R_{ij} and C_{ij} are the radiative and collisional rates, respectively, for the transitions from level i to level j.The left-hand side represents the transitions depopulating the level i, while the right-hand side describes the processes populating this level.

Radiative upward rates are given by the following expression,

$$R_{ij} = 4\pi\int \alpha_{ij}\frac{J_\nu}{h\nu}\,\mathrm{d}\nu, \tag{2.27}$$

where α_{ij} is an atomic cross-section for radiative bound-bound or bound-free processes. The downward rate is given by

$$R_{ji} = 4\pi \left(\frac{n_i}{n_j}\right)^* \int \frac{\alpha_{ij}}{h\nu} \left(\frac{2h\nu^3}{c^2} + J_\nu\right) \exp(-h\nu/kT)\,\mathrm{d}\nu, \tag{2.28}$$

with the asterix denoting LTE populations. The first term is due to *spontaneous emission*, while the second describes *stimulated emission*. Note that both R_{ij} and R_{ji} are computed on the basis of the same cross-section value.

The collisional upward rates are given by

$$C_{ij} = n_e \int \sigma_{ij}(v) f(v) v\,\mathrm{d}v, \tag{2.29}$$

where $f(v)$ is the velocity distribution of the colliding particles, which for hot stars ($T_{\mathrm{eff}} \gtrsim 10\,000$ K) are mainly electrons. The collisional downward rates result from

$$C_{ji} = \left(\frac{n_i}{n_j}\right)^* C_{ij} \tag{2.30}$$

The set of statistical equations for all levels of an atom form a linearly dependent system. In order to close the system, one of these equations has to be replaced by another relation, the *total number conservation* equation $\sum_i n_i = N_{atoms}$, with the summation extending over all levels and ions of a given species.

Conceptually, the non-LTE effects become important when the radiation field is strong enough for the radiative rates to dominate the atomic transitions over the collisional rates. A non-local effect takes place when photons coming from different parts of the atmosphere interact with the local medium. In the numerical calculations this translates to a coupling of the radiation field at different frequencies with the absorption and emission coefficients at different optical depths. In addition to the basic equations of the classical stellar atmospheres, the coupling of the radiative transfer and rate equations has to be solved simultaneously, which requires a greater effort than for the LTE case. This leads to a set of highly coupled, non-linear system of equations to be solved simultaneously. Due to the complexity of the problem, the basic structural equations have to be discretised and solved numerically.

In general terms, non-LTE model atmospheres are required in the analysis of stars at high temperature (high intensities and radiative rates) and low atmospheric densities (low collisional rates). Electron collisions cannot restore TE locally when the electron mean-free path is too large between collisions and the radiation field is strong enough to dominate the atomic transitions. The limits in atmospheric parameters (effective temperature, surface gravity) where the LTE approach is suitable to describe the atmospheric structure is still under investi-

gation, and one of the purposes of this Thesis is to contribute to this study. The LTE assumption for the model atmosphere is a good approximation for the kind of star analysed in this work, in particular for the line-formation region of the spectral lines of interest. This will be described in Chapter 5, where a comparison with non-LTE model atmospheres is provided.

2.4 Metal Line Blanketing

The inclusion of thousands to millons of lines in the computations of the atmospheric structure and the emergent flux changes the theoretical predictions. These spectral lines are often computed under the LTE approximation since it is prohibitive to treat all levels of all ions of all elements in non-LTE. Some computations are, nevertheless, performed in non-LTE for selected elements, including some iron-group members, with simplified model atoms accounting for *superlevels*. These superlevels group many individual levels of similar energies and physical properties. The individual levels are in LTE relative to each other (see e.g. Hubeny & Lanz 1995 for further details). However, LTE background line opacities are a good approximation for the computation of the atmospheric structure and the emergent flux for the stars under study here.

Since spectral lines are opaque to radiation, the energy transport takes place at other frequencies in order to conserve the total flux. For OB stars, numerous strong spectral features are located in the UV region and the photons escape at longer wavelengths. This is denoted as *line blocking*, which affects the overall shape of the emergent flux. The restriction of the energy transport by absorption lines produces a steeper temperature gradient in order to drive the flux through the atmosphere, resulting in an increase of temperature at deeper layers: the *backwarming effect*. On the other hand, in the outer layers the presence of lines give rise to *surface cooling*. The combined effects are known as *line blanketing*.

The implementation of line blanketing is performed following two different approaches: *opacity sampling* (OS) and *opacity distribution functions* (ODF). Both approaches use simplified line-broadening mechanisms. ODFs resample the detailed line opacity distribution to form a monotonic function of frequency, represented by a small number of quadrature points. The detailed calculations are performed once and the ODFs are tabulated (e.g. as a function of temperature and pressure) for discrete frequency intervals, at a given chemical composition and microturbulent velocity. These tables can be used in further applications, as in the present work. In the OS approach, the spectrum is sampled by choosing a larger number of frequency points than for the ODFs, allowing for a statistically approximate computation of the radiation flux. It offers many advantages in the treatment of line blends or overlaps and it allows non-standard chemical composition to be handled.

2.5 Spectral Line Formation

Spectral lines are formed by transitions between bound states of atoms and ions and they can provide information over a wide range of atmospheric depths, from the outer layers (where the line core is formed) to the deepest observable points (the continuum formation region). It is possible to gain deep insight into the physical state of the stellar atmosphere from the analysis of spectral lines. The line profile depends on the local conditions of the stellar plasma and on the atomic properties of the atom or ion under investigation. It is thus important to develop reliable methods to model spectral lines in order to infer the desired physical information from comparison to the observed spectra. In this section, the basic principles of spectral line formation are summarised, giving special emphasis to calculations accounting for departures from LTE.

2.5.1 Line Strength & Broadening Mechanisms

The strength of a spectral line is basically determined by the number of absorbers and the line absorption cross-section, given by

$$\alpha_{ij} = \frac{\pi e^2}{mc} f_{ij} \phi_\nu = B_{ij} \frac{h\nu_{ij}}{4\pi} \phi_\nu \tag{2.31}$$

where e is the electron charge, m the electron mass, f_{ij} the oscillator strength, and ϕ_ν is the line absorption profile, which is normalised such that $\int \phi_\nu \, \mathrm{d}\nu = 1$. The absorption profile is identical to the emission profile when complete redistribution is assumed. The basic atomic quantity that determines the line strength is f_{ij}. This is related to the *Einstein coefficient* B_{ij}, which gives the absorption probability. The line-centre frequency of the transition is denoted by ν_{ij}. The Einstein coefficients for absorption, stimulated emission (B_{ji}) and spontaneous emission (A_{ji}) are connected via the *Einstein relations*

$$A_{ji} = (2h\nu^3/c^2) B_{ji} \quad \text{and} \quad g_i B_{ij} = g_j B_{ji}. \tag{2.32}$$

The Einstein coefficients B_{ij} and B_{ji} can be obtained from a quantum mechanical treatment of atoms. On the other hand, the ab-initio derivation of A_{ji} requires to quantize the radiation field, which is much more complicated than deriving B_{ij}. Therefore Eqn. 2.32 is useful for obtaining A_{ji} once B_{ij} is known.

For an ideal and isolated atom with levels of infinite lifetime, the spectral lines would be perfectly sharp. However, there are several radiative and collisional mechanisms which produce smearing of the levels of real atoms in a plasma, resulting in a spectral line broadening.

Natural damping. This describes the line width related to the finite lifetime of the atomic levels set by the radiative decay. It results from Heisenberg's uncertainty principle $\Delta E \Delta t \geq h$, where Δt is the characteristic lifetime for a decaying state and ΔE refers to the energy spread of the state. Only the ground states of atoms and ions are stable, and the typical lifetimes of excited levels are of the order of 10^{-8} s. The radiation damping produces a *Lorentz profile*,

$$\phi_\nu = \frac{\gamma_{\rm rad}/4\pi^2}{(\nu - \nu_{ij})^2 + (\gamma_{\rm rad}/4\pi)^2}, \tag{2.33}$$

with a full half-intensity width $\gamma_{\rm rad}$ (mathematically equivalent to the full width at half maximum FWHM). It is the sum of the reciprocal mean lifetimes of the upper and lower levels, which accounts for all possible radiative decays of both levels (they are obtained experimentally or as a by-product of oscillator strength computations),

$$\gamma_{\rm rad} = \sum_{n<i} A_{in} + \sum_{m<j} A_{jm}. \tag{2.34}$$

Pressure broadening. The atoms embedded in a plasma interact via collisions with other atoms or charged particles, producing a pressure broadening of the lines. Precise collisional line-broadening data are derived from the quantum theory of pressure broadening; details can be found in Griem (1964, 1974). For early-type stars, the most important mechanisms of collisional broadening are the linear Stark effect for hydrogen lines and the quadratic Stark effect for the non-hydrogenic atoms and ions. Other broadening mechanisms, such as the Van der Waals interaction become more relevant at lower temperatures, where the presence of neutral atoms cannot be neglected (e.g. solar-type stars). When quantum mechanic data for pressure broadening are not available (in general for metallic lines), a good approximation formula given by Cowley (1971) can be employed to estimate Stark-widths,

$$\gamma_{\rm col} = 4.335 \times 10^{-7} Z^2 (Rc)^2 (E_u^{-2} + E_l^{-2}), \tag{2.35}$$

where Z is the ionic charge (1 for neutrals, 2 for singly-ionized species, etc.), $R = R_\infty \mu/m$ the Rydberg constant (with reduced mass μ and $R_\infty = 109737.315$ cm^{-1}) and $E_{u/l}$ the ionization energy of the upper/lower level (in s^{-1}). Pressure broadening also yields a Lorentz profile, except for the Linear Stark effect at high densities. The combination of radiative and collisional damping gives a Lorentzian profile with total width of $\gamma = \gamma_{\rm rad} + \gamma_{\rm col}$, as both processes are uncorrelated.

Doppler broadening. It is caused by the movement of atoms with a velocity distribution along the line of sight. The profile of each atom is Doppler shifted according to its individual line-of-sight velocity and the shifted profiles of an

ensamble of atoms are superimposed to yield the characteristic Gaussian Doppler broadening

$$\phi_\nu = \frac{1}{\sqrt{\pi}\Delta\nu_D} \exp(-\Delta\nu/\Delta\nu_D)^2 \tag{2.36}$$

where $\Delta\nu = \nu - \nu_{ij}$ and $\Delta\nu_D$ is the Doppler width of the line,

$$\Delta\nu_D = \frac{\nu_{ij}}{c}\sqrt{\frac{2kT}{m_A} + \xi^2}, \tag{2.37}$$

with m_A being the mass of an atom of the chemical species under consideration and ξ is the microturbulent velocity. The first term of the Doppler width corresponds to the thermal motion of the atoms in the medium, while the second is due to a non-termal component: the *microturbulence*. It is assumed that non-thermal motions have a Gaussian distribution around a most probable value ξ and occur on small scales when compared to a photon mean-free-path. Therefore, this constitutes an additional source of broadening. The most probable thermal velocity for atoms and ions is

$$v_{th} = \sqrt{\frac{2kT}{m_A}} = 0.129\sqrt{\frac{T}{m_A}} \text{ km s}^{-1}, \tag{2.38}$$

and it is comparable to the velocity of sound in the stellar atmosphere (e.g. at 30 000 K, the thermal velocity for hydrogen is $\sim$22 km s^{-1}).

The total line profile, accounting for natural, collisional and Doppler broadening, results from the convolution of a Lorentzian and a Gaussian, termed a *Voigt profile*,

$$\phi_\nu^{\text{Voigt}} = \phi_\nu^{\text{Doppler}} * \phi_\nu^{\text{Lorentz}} \tag{2.39}$$

All the previous broadening mechanisms act on microscopic scales and affect both equivalent width and line shapes. Macroscopic scales also have to be considered because resolving the star surface is not possible and only the light integrated over the stellar disk can be measured.

Rotational broadening. In rotating stars the spectral lines can be strongly affected by the relative Doppler shifts of the light emerging from different parts of the stellar disk. Only the line shape is affected by the frequency redistribution of the photons, while the equivalent width remains unchanged. High values of projected rotational velocities (along the line-of-sight) may cause a complication in the analysis of spectral lines as strong blends can be overlooked in this case.

Macroturbulence. Turbulent motions can also occur on a large scale compared to a photon mean-free-path. Individual macroturbulence cells give rise to Doppler shifts corresponding to the velocity of the cell. The effects on the line profile are well described with the radial-tangential model for macroturbu-

lence. This requires a further convolution of the line profile with an appropriate macrobroadening function (Gray 1992), introducing the radial-tangential macroturbulent velocity ζ as an additional parameter. Lucy (1976) proposed that non-radial oscillations of A-type supergiants might produce macroturbulent-like surface motions, imitating the movement of convective cells in cooler stars. More recent applications are given by Przybilla (2002) and Przybilla et al. (2006) for A-type supergiants and Ryans et al. (2002) for the case of B-type supergiants. Macroturbulence may also be important for giant and main sequence stars. Maximum values for the macroturbulence are constrained by twice (both directions of movement of the cells) the sound speed, in order to avoid cells moving at supersonic velocities.

Instrumental profile. An additional broadening of the spectral lines is due to the finite resolution of the spectrograph. This is important in cases of medium-resolution spectra and for high resolution only in cases where the stars present a low projected rotational velocity and therefore sharper lines. The instrumental profile is assumed to be Gaussian, with a FWHM corresponding to $v = c/2\sqrt{\ln 2}R$, where $R = \Delta\lambda/\lambda$ is the resolving power of the spectrograph.

2.5.2 Non-LTE Line Formation

Non-LTE line formation is also known as the restricted non-LTE problem. In this approach, the atmospheric structure (temperature, density, etc.) is assumed to be known from previous calculations (either LTE or simplified non-LTE), and is kept fixed, while only radiative transfer and statistical equilibrium for a chosen atom is solved simultaneously. In the present work, the non-LTE line formation is computed with the codes DETAIL and SURFACE (Giddings 1981; Butler & Giddings 1985; both updated by K. Butler). The implementation of the ALI approach of Rybicki & Hummer (1991) in DETAIL allows us to solve the coupling of the radiative transfer and the statistical equilibrium equations for multilevel atoms. The synthetic spectra are calculated with SURFACE on the basis of the non-LTE populations computed with DETAIL and refined line-broadening theories.

Hundreds of atomic energy levels and several thousands of transitions can be accounted for in the computations. The multilevel-line problem is treated for a single or several atoms (with different ionization stages) in a plane-parallel medium. The temperature and electron density are assumed to be prescribed as a function of depth. The continuum opacity and emissivity of H and He are previously computed with DETAIL. For multilevel atoms, one may express the coupling of the radiative transfer and statistical equations as

$$S_{ij} = S_{ij}(\mathbf{n}) \quad \text{and} \quad \mathbf{n} = \mathbf{n}\,(\bar{J}_{ij}), \tag{2.40}$$

where S_{ij} is the source function, $\mathbf{n}$ is the vector of level populations, $\bar{J}_{ij}$ is the *frequency-averaged mean intensity* and ij indicates the transition $i \rightarrow j$.

With careful preconditioning of the statistical equilibrium equations it is possible to simplify the coupled problem. Rybicki & Hummer (1991) show some examples where most of the transfer at frequencies of the 'core' of the line (described by the local part of the lambda operator) can cancel out analytically. The preconditioned statistical equilibrium equations can become linear in the ion level populations.

The solution scheme follows this procedure: (i) optical-depth scales and source functions for all frequencies are calculated from current estimates of the occupation numbers (the first estimate may be LTE-values); (ii) correction terms $\Delta J_\nu = (\Lambda - \Lambda^*)S_\nu = \Lambda S_\nu - \Lambda^* S_\nu$ are computed for all frequencies and depths by a formal solution (using for instance the scheme of Feautrier 1964) and by approximate formal solution using the Λ^*-operator; (iii) the approximate radiative transfer and the statistical equilibrium equations are simultaneously solved depth by depth, starting at the inner boundary (requiring that this boundary lies deep enough in the atmosphere). These steps are iterated until changes in the source functions and/or occupation numbers are sufficiently small. The iterative method proceeds as follows. An initial choice of the *old* populations is made. This allows one to setup the equations of statistical equilibrium. These equations are then solved for the *new* populations. Regarding these to be the old populations, another cycle of iteration can be made, continuing until convergence is obtained.

The coupled problem of radiative transfer and statistical equilibrium can be described for an idealised case of a two-level atom (lower level:1; upper level:2). This approximation may seem to be inadequate because real atoms contain many energy levels, however it provides a good description and an explanation of elementary processes that are crucial to understand the non-LTE line formation. Under this approximation, the source function can be written in terms of the $\bar{J}$ (non-local contribution of the radiation field) and the Planck function (local contribution)

$$S = (1 - \epsilon)\bar{J} + \epsilon B_\nu, \tag{2.41}$$

where ϵ is the *destruction probability* and can be calculated in terms of the collisional rate C_{21} and the Einstein coefficient for spontaneous emission A_{21} for cases where $h\nu \gg kT$ (for details see Mihalas, 1978)

$$\epsilon \approx \frac{C_{21}}{C_{21} + A_{21}}, \tag{2.42}$$

i.e. ϵ is the probability that an absorbed photon is destroyed by a collisional de-excitation process (C_{21}) rather than being re-emitted (A_{21}).

Equation (2.41) is fundamental for the problem. The first term on the right hand side represents the photons in the line created by scattering (emission fol-

lowing a previous absorption of a photon), while the second term represents the thermal creation of a photon (emission following a previous collisional excitation). Mathematically, the source function for a two-level atom (2.41) is still a linear function of the mean intensities.

For a two-level atom the source function is equal to the Planck function deep in the atmosphere and decreases from a point called the *thermalization depth* $\tau_{\rm th} \approx 1/\epsilon$ towards the surface to the value $\sqrt{\epsilon}B$. This can be explained by the fact that in a homogeneous medium departures from LTE arise only because of the presence of the boundary through which the photons escape. At large optical depths, all microscopic processes are in detailed balance, so the LTE approximation holds. However, as soon as the photons start to escape from the medium through the boundary, the photoexcitations are no longer balanced by radiative de-excitations. Since the absorption rate depends on the number of photons present, while the spontaneous emission does not (neglecting, stimulated emission for simplicity), the number of radiative excitations drops below the number of de-excitations as soon as photons start to escape. The lower level will start to be overpopulated with respect to LTE, while the upper level will be underpopulated. Since the source function measures the number of photons created per unit depth and is therefore proportional to the population of the upper level, the source function has to drop below the Planck function.

In a multilevel atom the source function contains non-linear terms in the radiation intensity coupling strongly with the optical depth, the frequency and the direction. In this case the source function may also increase towards the surface as it will be shown in Chapters 5 and 6. The non-LTE effects on the level occupations give rise to departures of the line source function $S_{\rm l}$ from the Planck function B_ν, which can be defined in terms of the departure coefficients $b_i = n_i/n_i^*$ (n_i, n_i^* are the level populations in non-LTE and LTE, respectively)

$$S_{\rm l} = \frac{2h\nu^3/c^2}{b_i/b_j \exp\left(h\nu/kT\right) - 1} \ , \tag{2.43}$$

with T being the local temperature.

A schematic description of the non-LTE line-formation calculations is displayed in Fig. 2.2. The model atmosphere is computed with ATLAS9 (Kurucz 1993b). Most of the input data of DETAIL were already discussed in this Chapter, except for the model atoms, which will be described in general terms in Chapter 3 and for the specific case of carbon in Chapter 6. The atmospheric parameters and the ODFs are input data for computing the atmospheric structure (ATLAS9), which is in turn an input for DETAIL and SURFACE. The classical atmospheric parameters accounted for are the effective temperature $T_{\rm eff}$, surface gravity $\log g$ and the metallicity [M/H]. The metallicity is the abundance of all elements heavier than He. The abundance of an element in a star is expressed

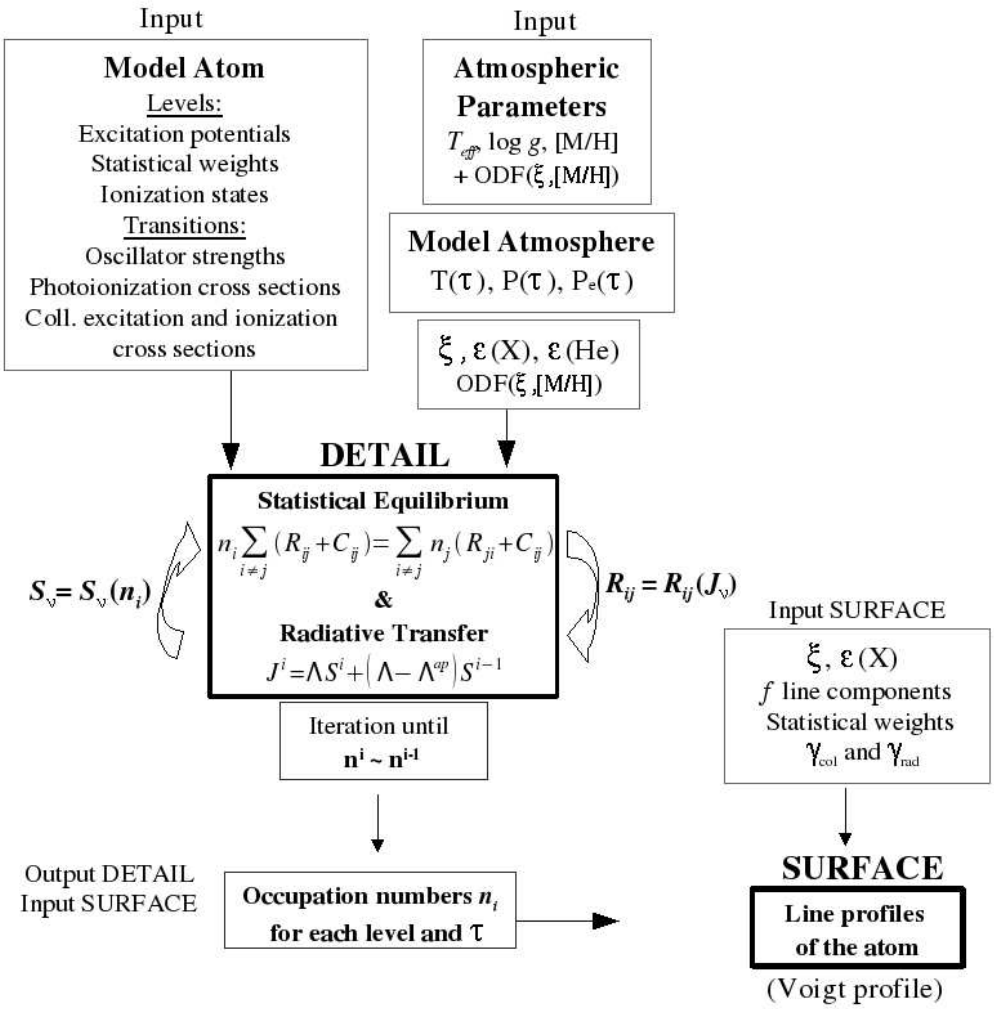

Figure 2.2: Schematic description of the non-LTE line-formation calculations with the codes DETAIL and SURFACE.

in a logarithmic scale relative to hydrogen, which is normalised in the Sun to a value of 12, $\epsilon(\mathrm{X}) = \log(\mathrm{X/H}) + 12$. Here, X and H are the number densities of absorbers of the species under study and of hydrogen in the star. The chemical abundance is one of the main parameters to be determined in this work.

The ODFs account for different values of microturbulence and metallicity, which should be consistent with those values derived from the analysed star. The line blocking, discussed in Sect. 2.4, is affected by ξ (broader/stronger lines result at higher microturbulence) and [M/H] (stronger lines result at high metallicity). Consequently a variable backwarming effect is expected to give different temperature $\mathrm{T}(\tau)$, pressure $\mathrm{P}(\tau)$, and electron pressure $\mathrm{P}_e(\tau)$ structures – in particular in the line-formation region. DETAIL accounts indirectly for $\mathrm{T}(\tau)$, $\mathrm{P}(\tau)$, and $\mathrm{P}_e(\tau)$ through the temperature, number density of heavy particles and of

electrons as a function of the mass-scale instead of the optical depth.

The ODFs and the microturbulence are also crucial in the solution of the coupled problem of radiative transfer and statistical equilibrium. In this case the line blocking affects the radiative rates and therefore the ionization balance. The ODF is accounted for as an input of DETAIL and the same value of ξ is considered in both DETAIL and SURFACE. A further input parameter of the model structure is the helium abundance. The chemical abundance of H, He and the metals under consideration also enter in the DETAIL computations.

SURFACE computes the formal solution of the radiative transfer (with a known source function from the level populations of DETAIL) for each depth point, resulting in synthetic non-LTE line profiles. Other essential input data for SURFACE are abundance, microturbulence, oscillator strength of each line component, collisional and radiative parameters (accounting for broadening mechanisms), energy levels, statistical weights, wavelengths of the transitions of interest. The atmospheric structure is also necessary to compute the line spectrum, as each line is formed at different depths in the atmosphere. The final line profile is a Voigt profile, which is subsequently convolved with a rotational, macroturbulent and instrumental profile (as explained in Sect. 2.5.1) before being compared with the observed spectra.

Since none of the atmospheric input data are known *a priori*, one can solve the problem by estimating some parameters or by performing an iterative (and extensive) procedure in order to derive them all self-consistently, depending on the accuracy one aims to achieve. More details of the spectral analysis based on ATLAS9, DETAIL and SURFACE are found in Chapters 5 and 6.

Chapter 3

Atomic Data for Spectral Modelling

The high precision of experimental and observational facilities impose a continuous demand for a large variety of good quality atomic data in order to interpret laboratory or astrophysical processes. In the case of astrophysics, the information concerning the physical state of the plasma in objects where the assumption of LTE is no longer valid can be inferred from their spectra only to the extent that radiative and collisional rates are known. Little of the relevant data can be determined under controlled laboratory conditions and therefore only few experimental data are available, motivating the development of sophisticated computational methods. Large collaborations have been established in order to provide an immense amount of accurate atomic data from ab-initio computations relevant for astrophysical studies: the Opacity Project (OP; Seaton 1987; Seaton et al. 1994) and the Iron Project (IP; Hummer et al. 1993). Large amounts of semi-empirical atomic data were also provided by Kurucz with an enormous effort over two decades (Kurucz 1992, and references therein).

A full description of the computation of atomic data is beyond the scope of the present work, therefore only the basis of theoretical calculations and some approximations will be described. Special emphasis will be given to some assumptions and possible sources of systematic uncertainties. A basic knowledge of the limitations and the different levels of accuracy of the atomic data involved is highly important in the construction of model atoms for non-LTE line-formation calculations. These are crucial for the modelling and further analysis of the stellar spectra. In this Chapter a brief description of the basic concepts of atomic data needed for spectral modelling, quantum mechanic ab-initio computations and some approximations is given. These are mainly based on Bautista (2000) and Berrington et al. (1995). Complementary information is also based on Hummer et al. (1993), Burke et al. (1971), and Nahar (2003). A summary of the construction of model atoms for DETAIL is also given, mainly based on the manual by K. Butler (http://ccp7.dur.ac.uk/Docs/detail.ps) and on Przybilla et al. (2001).

3.1 Basic Concepts

Two general atomic physics problems have to be solved in order to provide atomic data (energy levels and cross-sections) for spectral modelling: the atomic structure and scattering processes. The *atomic structure* problem is concerned with the computation of energy levels and spontaneous transition probabilities among bound states of the same ion (A-values) and from autoionizing levels of one ion to levels of the next ionized species. *The scattering problem*, relevant for the formation of the spectra in hot plasmas, is related to all the different processes that occur after a collision of an ion with a photon or other charged particle (in this case only electron collisions are considered because the electron velocity is much higher than the ion velocities).

- A (photon+ion) scattering $h\nu + A_i \rightarrow e^- + A_f$ can produce photoionization/radiative recombination or autoionization/dielectronic recombination[1] (the last two are not explicitly treated in the present computations, but are only implicit in the detailed resonance structures of the photoionization cross-sections). A_i, A_f refer to an ion in its initial and final state, respectively.
- A (electron+ion) scattering $e^- + A_i \rightarrow e^- + A_f$ can produce collisional excitation/de-excitation or collisional ionization/3-body recombination. A solution for ionization is more complicated because of the 3-body nature of the problem. Only limited data are available in the literature and for the remaining transitions approximate data are incorporated in the computations of the theoretical spectra.

Some theoretical methods to compute atomic structure, ionization and excitation of atoms and ions from ab-initio quantum mechanical considerations and other approximations are summarised in the next sections.

3.2 Atomic Structure Calculations

Quantum mechanics can provide a physical description of the interaction between electrons and photons with isolated atoms and their ions through the time-independent Schrödinger equation with appropriate boundary conditions

$$H\Psi_i = E_i\Psi_i, \tag{3.1}$$

where i represents a set of quantum numbers necessary to describe the system, Ψ_i are the wavefunctions, where all the information of the system is contained, E_i are the eigenvalues and H is the Hamiltonian.

[1]The inverse process of dielectronic recombination is photoionization via intermediate double-excited autoionizing states, i.e. resonances in atomic processes.

For light atoms and ions where the relativistic effects can be neglected (the spin the of electrons in not considered explicitly), the Hamiltonian can be written as

$$H = \sum_{i=1}^{N} \frac{p_i}{2m_e} - \sum_{i=1}^{N} \frac{Ze^2}{r_i} + \sum_{i \neq j} \frac{e^2}{|r_i - r_j|}, \tag{3.2}$$

where N is the number of electrons of the system. The first term is the sum of kinetic energy of all electrons, the second term is the potential energy due to the Coulomb attraction of all electrons by the nucleus and the third term is the energy due to electric repulsion between the electrons. The distance between an electron and the nucleus is r_i and the distance between two electrons is $|r_i - r_j|$. The nucleus is assumed to be infinitely heavy and a point charge.

In the presence of the two-electron operator $1/|r_i - r_j|$ one cannot obtain exact solutions to the Schrödinger equation for the N-electron system. Approximate methods for solving Eqn. (3.2) replace the two-electron term by one-electron potentials to give an effective Hamiltonian of the form

$$H^{\text{eff}} = \sum_{i=1}^{N} H_i^{\text{eff}} = -\sum_{i=1}^{N} \left[\frac{p_i}{2m_e} + \frac{Ze^2}{r_i} - V_i^{\text{eff}}(r_i) \right], \tag{3.3}$$

For highly ionized atoms the central field potential is a good approximation. There are several techniques regularly employed in the atomic structure calculations. The most important are: model potentials, methods based on Hartree-Fock theory, semiempirical methods, perturbation techniques, and the R-matrix method in the close coupling formalism. The latter will be described in Sect. 3.3.

Model potentials. An effective potential is proposed for specific cases (e.g., *central potential* for alkali atoms). A generally applicable potential is the Thomas-Fermi-Dirac type of central potential to generate one-electron orbitals (which depend on the angular momentum of the valence electrons). It is implemented in the widely used computer program SUPERSTRUCTURE (Eissner et al. 1974, Eissner 1991), which provides accurate results: ∼1% for energy levels and ∼10% for oscillator strengths.

Methods based on the Hartree-Fock theory. The Hartree-Fock (HF) method address the computation of one-electron orbitals in the non-local potential (direct and exchange) from electronic orbitals in a self-consistent way using the variational principle. A modification of this method for simple systems is the *frozen core* FC approximation: wave functions are computed by varying only valence orbitals while keeping orbitals in the core fixed. In most of the cases equivalent electrons in the same configuration[2] have to be accounted for. It is necessary to include the electronic configuration interaction, as in the *multicon-*

[2]Particular distribution of electrons among atomic orbitals.

figuration Hartree-Fock MCHF method (e.g. Froese Fischer 1977). The method is potentially very accurate, but computationally lengthy (it involves many iterations on the wavefunctions and normalisation coefficients).

Semiempirical methods. These methods compute the atomic structure of ions by solving simplified forms of the HF equations. The definition for the atomic potential is mostly empirically motivated and requires preconceived wavefunctions in order to compute the electron density function. The atomic structure equations are solved iteratively. The method has the advantage of being very efficient, but requires an enormous care in the construction of the initial electron density distribution. It is difficult to estimate the accuracy of any given calculation except by the observed agreement of a limited sample of data with experimental values. Kurucz (1988) and Kurucz & Peytremann (1975) based the computation of millons of energy levels and oscillator strengths for most ions of astrophysical interest on this method.

Some considerations of particular physical interest can also be taken into account in the atomic structure computations:

LS coupling. Light atoms and ions are well described by the Russell-Saunders or LS coupling, where the orbital (L) and the spin (S) angular momenta are assumed to be separately conserved, as is the parity π. An LS-term is a specific $LS\pi$ target state. LS coupling is characterised by a small separation of the fine-structure levels when compared to the separation of the terms (in contrast to jj coupling).

Configuration interaction. This refers to the interaction between different possible arrangements of the electrons in an atom; the resulting electron distribution, energy levels, and transitions differ from what would occur in the absence of the interaction. It can be seen as a correction to the Hartree's single-electron orbital approximation representing each electron moving individually in the field of the nucleus screened by the other electrons. In CI, wavefunctions may be obtained from linear combinations of single configuration wavefunctions of the same total angular momentum and spin symmetry (Condon & Shortley 1935). The CI representation has important effects on atomic quantities like oscillator strengths and it is a standard capability of codes like SUPERSTRUCTURE, CIV3 (Hibbert 1975), and Froese Fischer's MCHF code.

Relativistic effects. For heavy atoms and ions relativistic effects are important for the treatment of forbidden dipole transitions (under LS coupling) and also for the allowed transitions. The relativistic effects can be treated by the full Dirac formalism or by the addition of the Breit-Pauli operators to non-relativistic equations, the latter being widely used for practical applications. There are eight Breit-Pauli operators, but for low atomic number Z only four are considered (Eqn. 3.4): (1) the non-relativistic term (Eqn. 3.2); (2) the mass operator gives

the correction due to the relativistic variation of mass with velocity; (3) the Darwin term is characteristic of the Dirac theory and only applies to s orbitals; (4) the spin-orbit coupling term describes the interaction between the spin and the orbital magnetic moment of each electron. It splits the LS-term into fine-structure levels of symmetry $J\pi$: $J = L+S$, J being the total angular momentum. Other terms considering spin-other-orbit, spin-spin and orbit-orbit coupling are normally neglected, but can be included if necessary.

$$H^{\mathrm{BP}} = H^{\mathrm{NR}} + H^{\mathrm{mass}} + H^{\mathrm{Dar}} + H^{\mathrm{SO}} \tag{3.4}$$

Most of the current codes for atomic structure calculations as SUPERSTRUCTURE and CIV3 use the Breit-Pauli approximation to account for relativistic effects.

3.3 Scattering Calculations

The scattering system is composed of an atomic target with N electrons (Sect.3.2) and an additional incoming (electron impact) or outgoing (photoionization/electron impact) electron. Thus, the wavefunctions of the $(N+1)$-electron system Ψ can be expanded in terms of products of wavefunctions of the core ϕ_i (target wavefunctions obtained from atomic structure calculations) and those of the electron θ_i,

$$\Psi = \sum_i \phi_i(x_1, ..., x_N)\, \theta_i(x_{N+1}) \tag{3.5}$$

Substitution of Eqn. (3.5) in Eqn. (3.1), for the non-relativistic case, yields a system of coupled equations

$$-(\nabla^2 + k_i^2)\, \theta_i(x) + \sum_{i'} V_{ii'}\, \theta_i(x) = 0, \tag{3.6}$$

where $V_{ii'}$ is the potential energy generated by the interaction of the N electrons of the target, and k_i^2 is defined by

$$E = E_i(N) + k_i^2 \tag{3.7}$$

These equations have to be solved for every value of energy (k^2), of total angular momentum L of the $(N+1)$-electron system. This last condition motivates the so-called *partial waves expansion*, in which all states of definite angular momentum of the free electron are considered separately.

There are several methods to solve the scattering problem and calculate the cross-sections necessary for practical applications: the central field approximation, the Gaunt factor and the Coulomb-Born approximation, the R-matrix method, used for both photoionization and electron impact excitation and ion-

ization, as well as atomic structure. The latter has been implemented in several codes and has been widely used by groups like the Opacity Project and the Iron Project. Here, only the R-matrix and the Gaunt factor methods are briefly described.

R-matrix. The R-matrix method is a highly sophisticated and accurate technique. It takes into account nearly all the physical effects that contribute to cross-sections for astrophysical applications and it is applicable for all kind of ions, from neutral to highly ionized species. With the increased complexity of the calculations the R-matrix can be computationally very intensive.

The R-matrix method proposes a division of the configuration space by a sphere of radius a centered on the target nucleus (Burke et al. 1971). The aim is to compute the total wave function in the inner region, and the R-matrix on the boundary. The R-matrix is obtained for all energies by diagonalizing the Hamiltonian of the system only once for each set of conserved quantum numbers. The derived radial wave function of the scattered electron on the boundary depends on the R-matrix. The radial wave functions of the inner and outer regions have to be identical on the boundary. The next step in the calculation is to solve the electron-target scattering problem in the external region. There, the colliding electron is outside the atom, and can be considered distinct from the N target electrons. The wavefunction in the external region is fully determined in terms of the reactance matrix K. This matrix can be computed in terms of the wavefunction at $r = a$, and therefore, in terms of the R-matrix. Scattering observables may be calculated from the reactance matrix through the scattering matrix S.

In the internal region, $r < a$ (where r is the relative coordinate of the free electron) electron exchange and correlations between the scattered electron and the target are important and the $(N + 1)$-electron collision complex is similar to a bound state. Consequently, a CI expansion of this complex, analogous to that used in bound state calculations, is adopted (Eqn. 3.8). The total wavefunction Ψ in the inner region can be written in terms of the basis states set ψ_k and the energy-dependent expansion coefficients A_{Ek} as

$$\Psi = \sum_k A_{Ek}\psi_k. \tag{3.8}$$

Based on the assumption of the individual behaviour of both the colliding and the ionic electrons, the ψ_k functions for the $(N + 1)$-electron system can be expanded as the sum of product wavefunctions: the so-called close-coupling expansion (CC). The general form of the CC expansion for the radial wavefunction ψ in terms of a N-electron target basis χ_i and the scattering electron function θ_i is

$$\psi = \sum_i^{\infty} \chi_i\, \theta_i + \int_\epsilon \chi_\epsilon\, \theta_\epsilon, \tag{3.9}$$

where the first term address the bound and the second term the continuum wavefunctions (angular coupling and antisymetrization are assumed). For practical applications, only a finite close-coupling expansion can be used.

The R-matrix at $r = a$ is defined as

$$R_{ij}(E) = \frac{1}{2a} \sum_k \frac{\omega_{ik}(a)\omega_{jk}(a)}{E_k - E}, \tag{3.10}$$

where the surface amplitudes $\omega_{ik}(a)$ and the eigenvalues E_k are determined by diagonalizing the Hamiltonian.

This R-matrix is the basic solution of the electron-scattering problem in the internal region and must be matched to the external region solutions. It allows one to determine the structure of the $(N + 1)$ system, the collision strengths and photoionization cross sections. Although the basic computations in this method are very lengthy, it is a very efficient technique for computing large numbers of frequency points which allow complex resonance structures in the cross-sections to be accounted for.

In the external region, $r > a$, an electron exchange between the free electron and the target can be neglected if a is large enough to contain the charge distribution of the target. The internal and external regions are linked by the R-matrix on the boundary $r = a$. For the external region the scattered electron moves in a long-range multipole potential of the target. This potential is local and the solution can be obtained using a standard method for solving coupled differential equations with an asymptotic expansion or by using perturbation theory. These coupled equations for $r > a$ yield the solution for the reactance K-matrix and the scattering S-matrix, given by

$$S = \frac{1 + iK}{1 - iK} \tag{3.11}$$

The K-matrix contains all the information needed to derive the observables associated with electron collisions and the S-matrix elements determine the *collision strength* Ω_{ij} for a transition from an initial state i to a final target state j:

$$\Omega_{ij} = \frac{1}{2} \sum \omega |S_{if} - \delta_{if}|^2, \tag{3.12}$$

where $\omega = (2L + 1)(2S + 1)$ or $(2J + 1)$ depending on the coupling scheme. The collision strength is related to the *excitation cross-section* σ_{ij},

$$\sigma_{ij} = \Omega_{ij} \frac{\pi a_0^2}{g_i E_i}, \tag{3.13}$$

where a_0 is the Bohr radius, g_i is the statistical weight of the initial state i and E_i is the energy of the incident electron (in Rydbergs). In non-LTE computations the

transition rates C_{ij} are of interest (See Sect. 2.3). In this context it is convenient to define the thermally-averaged *effective collision strength* Υ_{ij},

$$\Upsilon_{ij} = \int_0^\infty \Omega_{ij} \, \exp(-E_j/kT) \, \mathrm{d}(E_j/kT), \tag{3.14}$$

with the transition rates being proportional to Υ_{ij}.

Radiative transition data are also provided by R-matrix computations. Oscillator strengths f_{ij} (computed with the R-matrix method applied to atomic structure) and photoionization cross-sections α_{iE} are proportional to the line strength $\mathbf{S}(j;i)$:

$$f_{ij} = \frac{8\pi^2 m \nu_{ij}}{he^2 g_i} \mathbf{S}(j;i). \tag{3.15}$$

The relation between line absorption cross-section and the oscillator strength is given by Eqn. (2.31). Using the dipole length operator $\mathbf{D}_L = e \sum_i \mathbf{r}_i$, where the sum is over all atomic electrons, the line strength is

$$\mathbf{S}_L(j;i) = | < \Psi_j | \mathbf{D}_L | \Psi_i > |^2. \tag{3.16}$$

An analogous expression, $\mathbf{S}_V(j;i)$ is found when employing the dipole velocity operator instead of the dipole length operator. Use of exact wavefunctions would give identical values of both operators, $\mathbf{S}_L = \mathbf{S}_V$. The difference between both line-strengths gives an indication of the accuracy achieved in the computations.

For final states Ψ_E in the continuum (photoionization) with energy E the oscillator strength per energy unity can be expressed as

$$\frac{\mathrm{d}f_{iE}}{\mathrm{d}E} = \frac{8\pi^2 m \nu_{iE}}{he^2 g_i} \mathbf{S}(E;i), \tag{3.17}$$

and the photoionization cross-section is given by

$$\alpha_{iE} = \frac{\pi e^2}{mc} \frac{\mathrm{d}f_{iE}}{\mathrm{d}E}. \tag{3.18}$$

Radiative transitions are restricted by selection rules, which may depend on the coupling scheme assumed. Electric dipole transitions require a change of the parity between the initial and final state, and the total angular momentum J can change only by $\Delta J = 0, \pm 1$ (but the transition $0 \leftrightarrow 0$ is forbidden). For LS coupling additional selection rules apply: $\Delta L = 0, \pm 1$ and $\Delta S = 0$. Intercombinations between two spin-systems are not allowed. Forbidden transitions, obeying other selection rules, can occur through electric quadrupole or magnetic dipole transitions, with significantly lower transition probability.

The inverse processes of the aforementioned collisional and radiative transitions are accounted for in the statistical equilibrium equations. The collisional downward rate is proportional to the collisional upward rate. In the case of radiative transitions, both the upward and the downward rates are functions of the oscillator-strength (for bound-bound processes) or of the photoionization cross section (for bound-free processes) defined above (see Sect.2.3).

Similar expressions to Eqn. (3.18) can be derived for free-free transitions. In hot stars such processes can be dominated by interaction of electrons with the fields of bare nuclei, as hydrogen is almost fully ionized, and they are referred to as Coulomb free-free transitions. In the case of electrons moving in the field of ions containing some bound electrons the free-free process due to other – much less abundant – ions is negligible but the perturbations affecting the line absorption process produce line broadening by electron impact (see Sect 2.5.1).

There are important physical effects to be taken into account in the evaluation of photoionization or collisional excitation/ionization cross-sections.

Configuration interaction. The first requirement in any scattering calculation is a good representation of the target, i.e. accurate wavefunctions for the target ion. Such a representation usually requires the inclusion of CI in the atomic structure model, which affects the calculated energy levels and oscillator strengths of the ion (See Sect. 3.2). Furthermore, comparisons between computed and experimental energies and oscillator strengths of the target are important indicators of the quality of the target representation and the overall accuracy of the obtained cross-sections.

Resonances. The resonance structure is an important part of collisional excitation/ionization and photoionization cross-sections. Physically, resonances occur when the incoming particle with just the right kinetic energy is trapped into an autoionizing state[3] of the $(N+1)$-electron system. Then, as the incoming particle remains trapped for a time before autoionization occurs, the time delay yields a phase shift in the wavefunction that manifests itself in sharp peaks in the cross-sections (resonances). Resonances appear in Rydberg series converging onto the various excitation thresholds of the target. Resonances in the collision strengths can produce an enhancement of the excitation rates by up to several factors in the case of valence electron excitation (up to orders of magnitude for inner-shell excitation). The resonances also enhance photoionization cross-sections.

Convergence of the partial wave expansion. It is a standard approach to expand the collision strengths in partial waves from 0 to infinity (in practice taking only the lower terms) for every possible value of the angular momentum of the free electron. The convergence of the partial wave expansion is very slow for allowed transitions and the number of partial waves needed for convergence increases with

[3]Autoionizing states are compound states of the (electron+ion) system located above the ionization potential. They result from the excitation of two or more electrons of the system.

the energy of the free electron. This convergence is a difficult practical problem and a possible source of error in the collision strengths for highly ionized systems for which very high collision energies need to be considered.

Convergence of the close coupling expansion. In the standard R-matrix approach, the integral term that accounts for the target continuum (Eqn. 3.9) is neglected or replaced by a discrete sum over bound functions. This approximation is good when considering valence electron excitation among the lowest energy levels of the ion. However, for excitations to highly excited levels the convergence of CC expansion must be looked at carefully. The collision strengths can depend on the size of the CC expansion.

Relativistic effects. The Breit-Pauli operators (see Sect. 3.2) have been implemented into the RMATRX package of codes by the Iron Project.

The Gaunt Factor approximation. Seaton (1962) and Van Regemorter (1962) suggested an approximate formula to obtain near-threshold collision rates for optically allowed transitions. The formula is based on the Bethe approximation and uses a g factor similar to that introduced by Kramers in the radiative case (the Gaunt factor). Later, the formula was modified to replace g, which is a varying function of energy, by an empirical parameter of $\bar{g} = 0.2$,

$$\Omega(i, i') = \frac{8\pi}{3\sqrt{3}} \mathbf{S}(i; i')\, \bar{g}. \tag{3.19}$$

where $\mathbf{S}(i; i')$ is the line strength. Seaton's approximation formula applies to the collision ionization cross-section, which is proportional to the threshold photoionization cross-section. Van Regemorter's formula applies to collisional excitation cross-section with $\bar{g} = 0.2$ for principal quantum number $n \neq n'$ and $\bar{g} = 0.7$ otherwise. For forbidden transitions, the collision strength can be estimated from the Allen (1973) semi-empirical formula. Often a value of $\Omega \approx 1$ is assumed for low ions. In practice, Ω can vary by orders of magnitude (see Chapter 5).

3.4 Construction of Model Atoms

The radiative and collisional bound-bound (RBB, CBB) and bound-free (RBF, CBF) transitions derived from atomic structure and scattering calculations are collected in order to construct model atoms (as indicated schematically in Fig. 3.1) for non-LTE calculations. They are input data for the codes DETAIL and SURFACE (Sect. 2.5.2). Figure 3.2 shows an example of the atomic structure of C II (singly-ionized carbon), accounted for non-LTE line-formation computations by Przybilla et al. (2001). The C II model atom considers simultaneously both the doublet and the quartet spin systems. All (dipole-allowed) radiative bound-bound transitions treated explicitly in non-LTE are displayed in the figure. One of the aims of the present work is to update this model with new input atomic

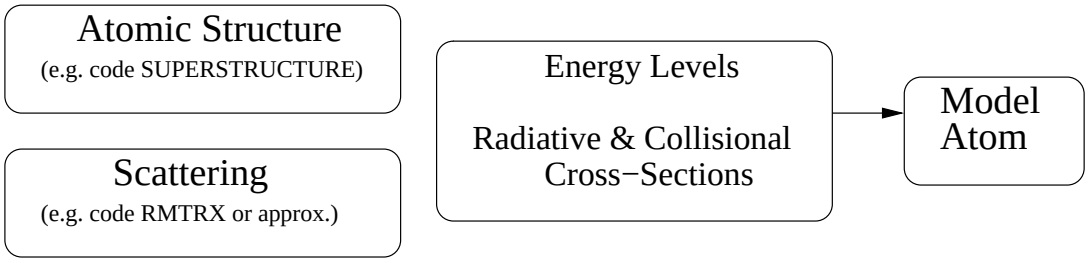

Figure 3.1: A model atom for non-LTE calculations, as the carbon model of the present work, can be constructed with input atomic data from the literature (with inhomogeneous accuracy). Energy levels are mostly adopted from NIST (National Institute of Standards and Technology) database.

data and the inclusion of other ionization stages to be treated simultaneously.

As explained in Chapter 2, DETAIL solves the coupled radiative transfer and statistical equilibrium equations. For model atoms of light elements these computations can be performed under the assumption of LS-coupled terms. When fine-structure data is available in the literature for light elements the cross-sections are co-added. Experimental level energies – when possible – are considered. Radiative and collisional transitions from different sources can have a wide range of accuracy, from a typical 10-20 % for the ab-initio calculations to orders of magnitude for approximation formulae. DETAIL allows robust model atoms with hundreds of levels to be implemented explicitly in non-LTE, several thousands of transitions and a large frequency grid allowing the resonance structure of photoionization cross-sections to be considered.

The following describes briefly the general structure of a model atom (of one or more ionization stages) for DETAIL.

Frequency grid. The frequency grid can have several thousands of points.

Energy levels and **statistical weights**. For most of the energy levels experimental energies are available. Data for high-excitation levels can be adopted from theoretical computations when experiments do not provide them.

RBB. Oscillator strengths for dipole-allowed and in some cases also intercombination lines are taken from ab-initio calculations.

RBF. Photoionization cross-sections are also based on ab-initio calculations. Autoionization and dielectronic recombination are consistently considered through the detailed resonance structure.

CBB. When available, collisional excitation cross-sections are adopted from ab-initio calculations (in general for the lowest states). When such calculations are not available, the Van Regemorter (1962) approximation is employed in the optically-allowed cases and the semi-empirical formula of Allen (1973) in the forbidden cases.

CBF. Collisional ionization rates are evaluated according to the Seaton (1962)

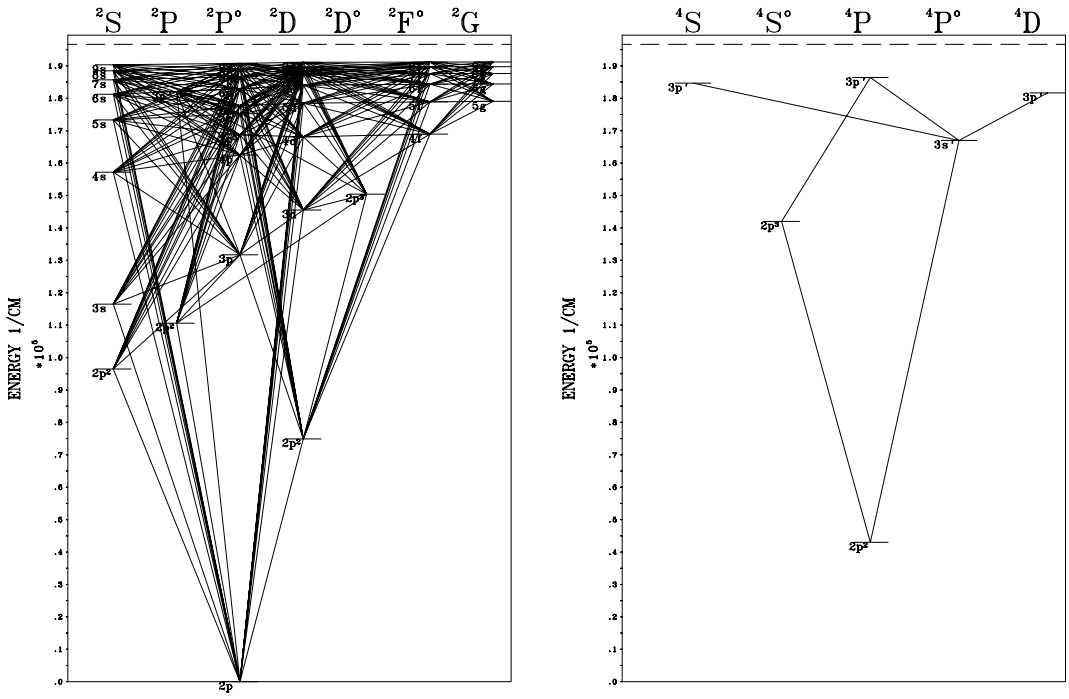

Figure 3.2: Grotrian diagram for the C II doublet (left hand) and quartet (right hand) spin systems from the carbon model atom by Przybilla et al. (2001). Displayed are all radiative bound-bound transitions treated explicitly in non-LTE.

approximation adopting threshold photoionization cross-sections from ab-initio calculations.

Continuous opacity from bound-free and free-free transitions of H and He, which are the main opacity contributors, are also accounted for. Non-LTE level populations for these may be computed in a previous step.

In most cases it is mandatory to evaluate the input atomic data by comparison with observed spectra. The empirical calibration of a model atom is the only way to choose the optimum set of atomic data able to reproduce observations independently of the physical conditions of the stellar plasma.

SURFACE computes the synthetic non-LTE line profiles based on the atomic level populations calculated in DETAIL (it can also compute LTE line spectra). Experimental wavelengths and fine-structure splitting are considered. Collisional damping parameters accounting for broadening mechanisms are calculated either from approximations (for metals) or from refined theories (for hydrogen and helium). Radiative damping constants can be derived from experiments or from oscillator strengths computations, as explained in Sect. 2.5.1.

Chapter 4

Spectroscopic Analysis

Some physical quantities derived from spectral analyses of stars constitute basic observational constraints for broad astrophysical fields, like stellar evolution and chemical evolution of the Milky Way and other galaxies. Hence, any systematic effect in the interpretation of the stellar spectrum might result in non-reliable conclusions concerning different fields. In particular, a precise atmospheric parameter determination is of fundamental importance for the further quantitative study of the stellar spectrum. This is a non-trivial problem to be solved because the line spectrum and the observed flux distribution provide the information for the determination of the atmospheric parameters (i.e., the spectroscopic analysis depends on basic parameters, which in turn depend on the spectrum).

As we have briefly discussed in the last chapters, the modelling of the stellar spectrum is complex even for the most simple cases of classical stellar atmospheres. The coupling of the radiation field with radiative and collisional transitions increases the number of variables to be taken into account in the analysis. The observational constraints derived from a spectral analysis rely on a large quantity of model assumptions: from the model atmosphere to the input atomic data of the model atoms for non-LTE line formation. In addition, the observed spectra suffer a long reduction process (see Appendix A) not free of systematic effects. The quantitative spectral analysis for the derivation of the fundamental stellar parameters can be schematised as in Fig. 4.1. The line-profile fitting of synthetic profiles to observed spectra could result in an inconsistent quantitative analysis when the underlying physics of the problem is not well solved. It is thus important to test the consequences of employing different theoretical approaches on the final synthetic lines and on the derived physical information of the star.

In this chapter, some open issues concerning quantitative analyses of stellar spectra for OB main sequence and giant stars are considered. They constitute an important motivation to the present study. In particular, some interesting results derived from an analysis of stars in the Large Magellanic Cloud (LMC) are presented.

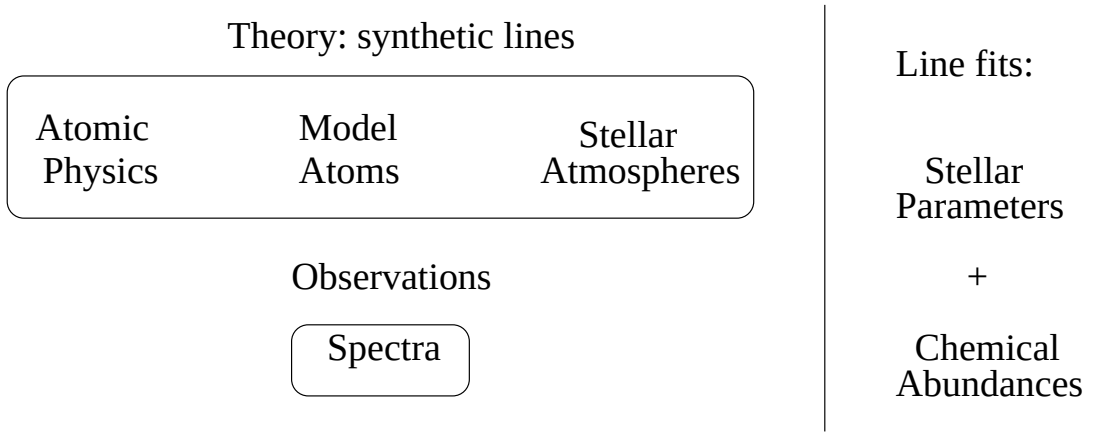

Figure 4.1: Quantitative Spectroscopy

4.1 Atmospheric Parameters

Among the various parameters that specify the physical conditions of stellar atmospheres, the most important are the stellar *effective temperature* and the *surface gravity* (to a lesser extent also the chemical composition). They are called *fundamental atmospheric parameters* and only these are directly related to fundamental physical properties of stars like the mass, radius and luminosity. Parameters like micro- and macroturbulence are of secondary importance in the overall description of stars, but nevertheless should not be ignored in a fine analysis.

The derivation of basic atmospheric parameters is an important issue of stellar spectroscopy. Numerous studies have contributed with techniques to determine them in different kind of star. The motivation of fundamental parameter determination in early-type stars started from a previous study of main sequence B, A and F-type stars (Nieva 2002; Adelman et al. 2002). For OB stars the accuracy of the effective temperature determination can be much lower than for cooler stars when employing standard methods (for instance, photometric calibrations). Discrepancies up to $\sim$25% can be found from different approaches for the $T_{\rm eff}$ determination (see Table 4.1 below). This can produce large inconsistencies in the derived chemical abundances, therefore the problem should be addressed with care before any further analysis.

Photometric Approach. The fundamental parameter $T_{\rm eff}$ can be derived from an analysis of the variations of strategic regions of the stellar flux. The area under the flux distribution curve delimited by a filter function can be expressed as a *photometric* magnitude. Several photometric systems have been developed to account for parameter-sensitive features in the shape of the stellar flux distribution via magnitude (colour) differences. The most commonly used

are the broad-band Johnson UBV and the intermediate-band Strömgren $ubvy\beta$ systems. The photometric colour indices can be calibrated on the basis of emergent fluxes from model atmospheres calculations and therefore it is possible to find a link between those indices and atmospheric parameters (see Smalley 1996 for an overview of several calibrations). For hot stars, the Strömgren system provides a temperature-sensitive indicator associated with the Balmer jump, the gravity sensitive β-index, which measures the strength of H_β, and even a metallicity sensitive indicator. A useful photometric calibration of $T_{\rm eff}$ for early-type stars based on Strömgren indices is provided by Napiwotzki, Schönberner & Wenske (1993). On the other hand, the three-colour Johnson system is less accurate for a parameter determination because of its broad-band character, but it is nevertheless useful to *estimate* temperatures when Strömgren indices are not available (as in the case of many stars belonging to several Galactic OB associations). The accuracy of photometric calibrations depends on the modelling of stellar atmospheres and on the sensitivity of the spectral features to the parameters of interest, with additional uncertainties from the interstellar reddening[1]. A solution for the latter is the $T_{\rm eff}$-calibration of the reddening-free Q-parameter defined by $Q = (U-B) - 0.72(B-V)$ (e.g. Daflon et al. 1999; Lyubimkov et al. 2002), widely used for analyses of large samples of OB-type stars. These Strömgren and Johnson photometric calibrations are derived for main sequence and giant stars, and therefore applicable – in principle – to the current work.

Spectroscopic Approach. Another method for the stellar atmospheric parameter determination relies exclusively on the analysis of the line spectrum, the so-called *spectroscopic approach*. The analysis involves profiles and line strengths of spectral features from hydrogen, helium and metals. This method can only be performed iteratively, and the final parameters are obtained when the overall conditions set by different spectral indicators are consistently met.

Assuming the metallicity and the helium abundance to be known, we are interested to derive from the line spectrum: $T_{\rm eff}$, $\log g$ and ξ. For early-type stars, $\log g$ can be determined (when the temperature is known) by fitting the wings of the Balmer lines, which are strongly affected by the linear Stark effect. Both $T_{\rm eff}$ and $\log g$ can be derived from ionization equilibria, i.e. from the condition that the chemical abundance is independent from the ionization stage of the elements to be analysed. Iterations of an ionization equilibrium with the Balmer-lines analysis result in a solution for ($T_{\rm eff}$, $\log g$). For a simultaneous analysis of three ionization stages there is a unique solution, independent from other parameters. For only two ionization stages the solution depends on the microturbulence. On the other hand, ξ can be derived by demanding the strong and weak lines to provide the same value of chemical abundance of a given species. This can be

[1] A frequency-dependent extinction of the radiation because of scattering by dust and molecules in the interstellar medium.

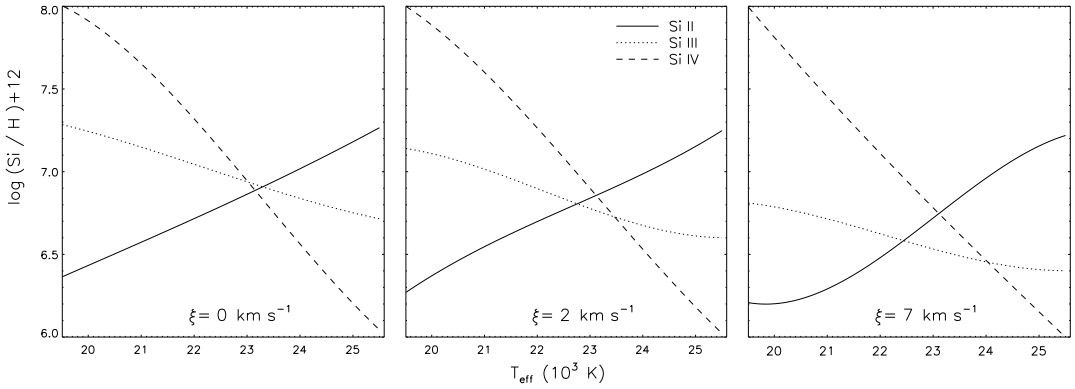

Figure 4.2: Effective temperature determination via Si ionization equilibrium for the star D15 in the LMC cluster NGC2004 (Nieva et al. 2003). Si abundances are denoted in logarithmic scale.

done for different elements, obtaining the same value of microturbulent velocity in the optimum case. When the metallicity and the He abundance are not known, they should also be determined from an iterative process.

In Fig. 4.2 an example of effective temperature determination from the Si II/III/IV ionization equilibrium is shown (calculations are based on the Si model of Becker & Butler 1990). For each $T_{\rm eff}$ value, a corresponding log g was derived from Hγ in LTE. The analysed star is LMC NGC2004 D15, and the final solution based on the Si II/III/IV ionization equilibrium, after some iterations on all atmospheric parameters, give $T_{\rm eff}$= 23 000 K, log g= 3.86 dex and ξ =0 km s^{-1}. The microturbulence was simultaneously derived from Si and O lines.

Note that the final $T_{\rm eff}$ is highly dependent on the value of ξ when *only two* consecutive ionization stages are considered (as it is usual in practice). When considering only Si II/III, a variation in microturbulence $\Delta\xi = +7$ km s^{-1} gives a different solution for the temperature by $\Delta T_{\rm eff} =\sim -1\,000$ K, while for Si III/IV, $\Delta\xi = +7$ km s^{-1} gives $\Delta T_{\rm eff} =\sim +1\,200$ K. The Si III triplet centered in λ4568 Å, chosen for the analysis, is strong in the studied star, and therefore sensitive to the microturbulence. The Si II $\lambda\lambda$4128/30 Å doublet and the Si IV λ4116 Å line are weak and almost insensitive to the microturbulence, consequently the temperature derived only from those ionization stages is almost insensitive to ξ (Nieva et al. 2003).

Figure 4.3 shows the effect of the temperature (21 000 $\leq T_{\rm eff} \leq$ 32 000 K) on some spectral lines of the stars analysed in the present work (for more details about the observed spectra see Sect. 5.2). Some lines like from Si II or Si IV can be very sensitive to temperature, while Si III lines remain strong in the selected stars. Both, Si II and Si IV are good indicators for $T_{\rm eff}$, as well as He II for higher temperatures. Lines of neutral helium change little with $T_{\rm eff}$. The strength of Hδ increases for lower temperatures.

The success of a self-consistent analysis indicates that the modeled spectra

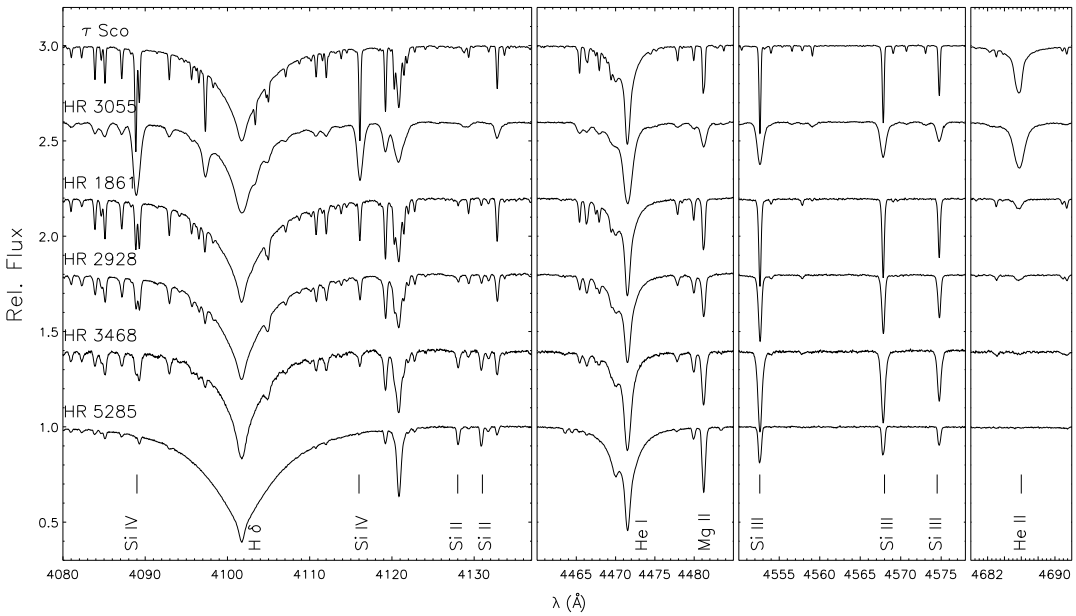

Figure 4.3: Sensitivity of some spectral lines to temperature for the stars analysed in the present work (τ Sco has the highest and HR 5285 the lowest temperature).

account for the necessary underlying physics to reproduce the observations and that the derived atmospheric parameters are almost free of systematic errors. Some inconsistencies like discrepant solutions of ($T_{\rm eff}$, log g) for different species might be related to problems in the iteration procedure (some parameter is still not converging to a unique value) or to shortcomings in the spectral line modelling (e.g. incomplete model atoms for non-LTE line formation and/or inappropriate input atomic data).

Metal lines, and consequently chemical abundances, can be highly sensitive to atmospheric parameter variations and therefore the final accuracy can be improved when a consistent spectroscopic analysis is performed. Therefore the spectroscopic approach can be much more accurate than the photometric methods. It also allows us to avoid important systematic effects in fundamental parameters, but only when the spectral modelling is realistic. This approach can be very lengthy, in particular when the starting points are chosen far from the final solution.

In the last decades, (not well-understood) systematic discrepancies of effective temperatures derived from photometric and spectroscopic approaches were reported in the literature. These discrepancies were also found in a previous analysis of early-B type main sequence and giant stars in the Magellanic Clouds. An example of solutions for $T_{\rm eff}$ following different approaches is shown in Table 4.1. Discrepancies as large as 4 000 K or more are found for this sample stars. For the star D15, a difference of temperature by −3 000 K (e.g. those derived from

Table 4.1: Values of $T_{\rm eff}$ for stars in the LMC cluster NGC2004. They are derived photometrically from different sources and calibrations, and from a spectroscopic approach. For the Q and UVB calibrations the indices from Balona & Jerzykiewicz (1993) are adopted.

Star	$T_{\rm eff}^{\rm C}$	$T_{\rm eff}^{\rm Ke}$	$T_{\rm eff}^{\rm D}$	$T_{\rm eff}^{\rm L}$	$T_{\rm eff}^{\rm N}$	$T_{\rm eff}^{\rm K}$
D15	22000	···	19442	18148	19100	22500
C16	···	28050	···	···	···	24600
D3	···	26180	25575	24063	···	23900
C9	···	···	18933	17377	19100	24000
B30	23000	23550	21344	20319	20251	23450

$T_{\rm eff}^{\rm C}$ from Caloi & Cassatella (1995): UV flux.
$T_{\rm eff}^{\rm Ke}$ from Keller et al. (2000): WFPC2 photometry.
$T_{\rm eff}^{\rm D}$ from calibration of Q-parameter (Daflon et al. 1999).
$T_{\rm eff}^{\rm L}$ from calibration of Q-parameter (Lyubimkov et al. 2002).
$T_{\rm eff}^{\rm N}$ from calibration of U-B index (Napiwotzki et al. 1993). E(B-V) from Balona (1993).
$T_{\rm eff}^{\rm K}$ from Korn et al. (2000, 2002): spectroscopic determination (Si, Becker & Butler 1990).

Daflon et al. 1999 and Korn et al. 2002), implies a subsequent correction for $\log g$ of -0.3 dex from a line fit to Hγ (in LTE) and a higher microturbulence by 10 km s^{-1}.

Those discrepancies in the fundamental atmospheric parameters are translated into systematic differences in the derived chemical abundances. For temperatures derived from Daflon et al. (1999), the Si ionization equilibrium is not achieved (for a visualisation of this see the variation of Si abundances in Fig. 4.2 for a lower $T_{\rm eff}$ by $\sim$3 000 K). Therefore, another aim of this work is to investigate the discrepancies of the derived fundamental atmospheric parameters.

The above mentioned silicon model atom has some limitations like a rather small number of levels treated explicitly in non-LTE, in particular for levels with high excitation energy, compared to a new model atom by Przybilla & Butler (2007). In the present work, silicon is not analysed but instead a self-consistent method to simultaneously derive the atmospheric parameters and select the optimum set of input atomic data for a carbon model atom is proposed. Effective temperature and $\log g$ are derived in the present work, when possible, from simultaneous ionization equilibria of He I/II and C II/III/IV and from the Balmer lines in non-LTE.

4.2 Chemical Abundances

The chemical abundance of a given species can also be derived by fitting synthetic spectral lines to the observed spectrum[2]. The abundance can be determined only when *all* other parameters are known (i.e. effective temperature, surface gravity, microturbulence, macroturbulence, projected rotational velocity, metallicity).

In the case of fundamental atmospheric parameters derived from photometric calibrations, the process is shortened and both ξ and $\epsilon(X)$ can be derived faster. This procedure does not always allow to obtain ionization balance of the species under consideration. In such cases it is difficult to identify the sources of errors, i.e. the parameter calibration or the model atom.

With the spectroscopic approach all parameters and abundances of some species can be simultaneously derived from multiple ionization equilibria. The optimum solution for the whole set of atmospheric parameters allows chemical abundances of the remaining species to be derived (see Chapter 6 for a detailed description of chemical abundance and atmospheric parameter determination).

[2]Another method is based on the equivalent widths of the line profiles and the curve of growth, nevertheless this is not as accurate as line fitting, as line blends with other species may be more easily overlooked.

Chapter 5

Hybrid Non-LTE Approach for H and He Line Formation

Hydrogen and helium are of major interest in the astrophysical context, as they constitute practically all light-emitting plasma. The lines of H and He are the strongest spectral features in OB stars. Moreover, they are primary diagnostic tools for stellar analyses throughout the Hertzsprung-Russell diagram. Because of their strength they can sample the plasma conditions throughout large parts of the stellar atmosphere, to a far greater extent than do the metal lines.

The information on the temperature and density structure encoded in the spectra is *interpreted* by comparison with synthetic spectra, which requires that the basic atmospheric structure equations in combination with the radiative transfer problem be solved (as explained in Chapter 2). The model predictions may differ, depending on the approximations made and on the atomic data used. Their quality can be assessed by the ability to reproduce observation. In the optimum case *all* observational constraints (continua/spectral energy distribution, line profiles) should be reproduced *simultaneously*, indicating the absence of systematic error (assuming a unique solution). A thorough reproduction of the hydrogen and helium line spectra should therefore be viewed as a precondition for all further studies.

Non-LTE effects play a dominant rôle in the formation of the hydrogen and helium line spectra in early-type stars, as known since the seminal work by Auer & Mihalas (1972, 1973). Despite the enormous progress made over the past 40 years, some notorious problems have remained. Observations in the near-infrared provide one key to improve the situation via extension of the present observational database to a domain of amplified non-LTE effects (in OB stars). Some of the problems have been related recently to the remaining inaccuracies in the atomic data. Thus, the modelling of the hydrogen Paschen, Brackett, and Pfund series in early-type stars could be improved, resulting in corrections of equivalent widths by as much as a factor 2–3 (Przybilla & Butler 2004; Repolust et al. 2005). Also, the observed behaviour of the He I λ10 830 Å transition in OB

dwarfs could be reproduced for the first time (Przybilla 2005). In other cases, the reasons for shortcomings in the non-LTE modelling can be subtler. An example of this is the He I singlet line problem in early-type stars: computations with non-LTE model-atmosphere codes reveal discrepancies not only between theory and observation but also between different theoretical calculations. The overlap of an He I resonance transition with Fe IV lines results in high sensitivity to the model assumptions (Najarro et al. 2006).

In this chapter, the status of non-LTE line-formation computations is evaluated for the two most abundant elements in the most common targets of massive star analyses, OB dwarf and giant stars. This study constitutes the basis for Chapter 6. The hybrid non-LTE approach (Sect. 5.1) is thoroughly tested on high-quality spectra of six stars in the solar vicinity (Sects. 5.2 and 5.3). In contrast to typical studies from the literature, the *entire* hydrogen and helium line spectra is investigated in the optical range, plus some additional near-IR data, taking advantage of recently improved non-LTE model atoms. After making sure that excellent agreement between theory and observation can be obtained (i.e. also avoiding the aforementioned He I singlet line problem), this non-LTE modelling is compared with libraries of synthetic fluxes from the literature (Sect. 5.4). This is done in order to test their suitability for quantitative analyses of OB dwarfs and giants. Such libraries are required for (automatised) analyses of large observational datasets obtained with existing or future multi-object spectrographs (e.g. the VLT-FLAMES survey of massive stars: Evans et al. 2005; GAIA: Perryman et al. 2001). It is shown that reliable modelling of the line spectra of the two most basic elements is not straightforward. On the contrary, considerable systematic errors may result for quantitative analyses of OB stars when applying these libraries blindly. Finally, a summary of this chapter is provided in Sect. 5.5.

5.1 Model Calculations

The hybrid non-LTE approach solves the restricted non-LTE problem on the basis of prescribed LTE model atmospheres. The approach is physically less elaborate than fully self-consistent non-LTE calculations, as more approximations are involved. However, at the same time it is superior to the pure LTE approximation. In particular, it provides an *efficient* way to compute realistic synthetic spectra in all cases where the atmospheric structure is close to LTE (which puts restrictions on the parameter space coverage). The hybrid non-LTE approach also allows extensive non-LTE model atoms to be implemented, facilitating a highly detailed treatment of the atomic processes involved (e.g. account for the resolved resonance structure in photoionizations, avoidance of the – powerful, however also approximate – superlevel formalism).

As described in Chapter 2, line-blanketed, plane-parallel, homogeneous, and hydrostatic LTE model atmospheres are computed using the ATLAS9 code (Ku-

rucz 1993b). Non-LTE population numbers and synthetic spectra are then obtained with recent versions of DETAIL and SURFACE (Giddings 1981; Butler & Giddings 1985). The coupled radiative transfer and statistical equilibrium equations are solved with DETAIL, employing the Accelerated Lambda Iteration (ALI) scheme of Rybicki & Hummer (1991). Synthetic spectra are calculated with SURFACE, using refined line-broadening theories.

The non-LTE model atoms for hydrogen and He I/II adopted in the present work are described in detail by Przybilla & Butler (2004) and Przybilla (2005), respectively. Use of improved atomic data for electron impact excitations, in particular from *ab-initio* computations, allows consistent results from the hydrogen lines in the visual and near-IR to be derived throughout the entire range of early-A to O stars . A 15-level model is used for modelling main sequence stars, as well as a 20-level model for the giants. The He I/II model atom considers all He I LS-coupled terms up to the principal quantum number $n = 5$ individually, and packed levels up to $n = 8$ separately for the singlet and triplet spin system. All levels up to $n = 20$ are considered in the He II model. This model atom has been successfully used to reproduce observed trends of the highly non-LTE-sensitive He I λ10 830 Å transition in early-type main sequence stars (Przybilla 2005). The He I/II model was also employed to analyse the visual/near-IR spectra of extreme helium stars (Przybilla et al. 2005) and subluminous B stars (Przybilla et al. 2006b).

Radiative transitions in DETAIL are treated with simplified line broadening formalisms: for transitions between hydrogen levels with $n \leq 7$ approximate Stark-broadening (Griem 1960, following the implementation of Auer & Mihalas 1972, Appendix) is considered, while for all other transitions, also in He I/II, depth-dependent Doppler profiles are assumed. Microturbulence is explicitly accounted for by including the appropriate term in the Doppler width (see Eqn. 2.37). Both continuous absorption and line blocking (via LTE Kurucz' opacity distribution functions, ODFs, Kurucz 1993a, using the 'little' wavelength interval versions), are accounted for as background opacities in solving the radiation transfer. In this regard the hybrid non-LTE approach has an advantage over present-day 'exact' non-LTE computations: all species responsible for metal line blocking and blanketing can be considered, though approximately. The 'exact' non-LTE methods, on the other hand, are constrained to several abundant light elements and typically iron (and sometimes nickel), i.e. only the major line opacity sources are covered. Note that these ODFs were calculated for solar abundances according to Anders & Grevesse (1989). The latter have been revised in more recent work such as Grevesse & Sauval (1998). In particular the reduction of the abundance of iron (the most important line opacity source) by $\sim$0.2 dex should be considered. This is done in this work by adopting the Kurucz (1993a) ODFs for appropriately reduced metallicity; see Sect. 5.4.1 for further discussion.

The resulting non-LTE populations are then used to compute realistic line profiles with SURFACE. The same microturbulent velocity as in DETAIL and in

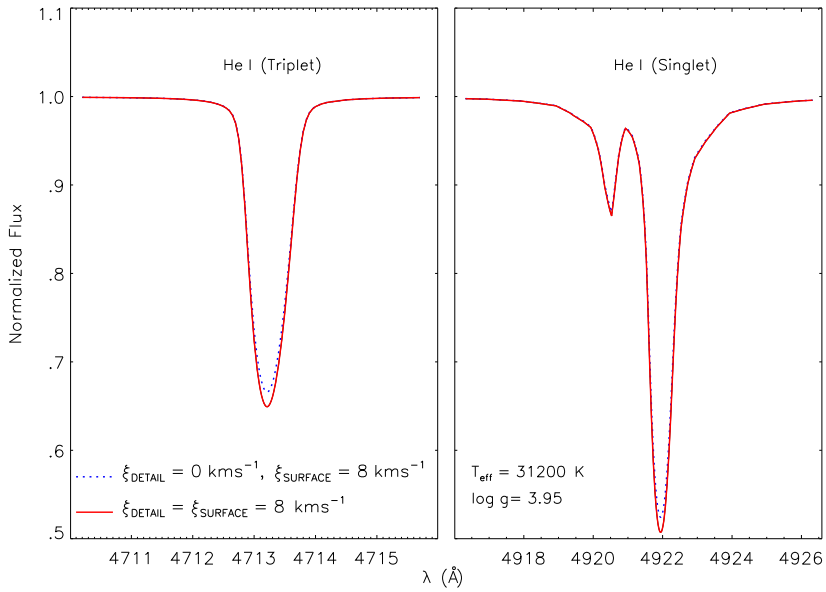

Figure 5.1: Sensitivity of theoretical He I line profiles to modifications of the microturbulent velocity in the statistical equilibrium calculations. The microturbulence of the ATLAS9 model atmosphere structure is held fixed at $\xi = 8\,\mathrm{km\,s^{-1}}$. The test calculations have been done for one of our sample stars (HR 3055). Similar effects are found for other He I lines, while the He II and H lines are practically insensitive to this.

the model structure computations with ATLAS9 is adopted. In this step of the calculation detailed Stark-broadening data are employed, as summarised in Table B.1. All other important data relevant to line formation are also given there: wavelengths, lower and upper levels involved in the transition, oscillator strengths $\log gf$, their accuracies, and sources.

Note that, in typical non-LTE computations for OB stars, microturbulence is only included in the final profile calculation. The present choice is based on test calculations that indicate line-profile fits are improved if microturbulence is also included in computing the level populations. The net effect is a slight strengthening of the lines (Fig. 5.1). However, the effect is far less pronounced than described by McErlean et al. (1998), who investigated unblanketed non-LTE models for B-type supergiants at slightly higher microturbulence; cf. their Figs. 3 & 4.

The hybrid non-LTE approach involving the codes ATLAS9, DETAIL, and SURFACE (henceforth abbreviated ADS) is tested here for early B-type dwarfs and giants, supplemented by LTE computations with ATLAS9 and SURFACE (AS). This methodology may be applied to a wider range of atmospheric parameters (i.e. $T_{\rm eff}$ and $\log g$). Line-blanketed, static, and plane-parallel LTE models provide an even more realistic description of stellar atmospheres at lower temperatures

and higher gravities (excited He II states should be ignored at lower $T_{\rm eff}$ in order to avoid numerical inconsistencies). Slightly higher temperatures (late O-types) and lower surface gravities (less-luminous supergiants) may also be covered, until the hybrid non-LTE approach meets its limitations when non-LTE effects on the atmospheric structure and/or hydrodynamic mass-outflow may no longer be neglected.

5.2 Observational Data

The proposed analysis technique is tested on six bright Galactic objects in the entire optical range and also for near-IR lines when available. The programme stars sample the parameter space in effective temperature and surface gravity covered by typical applications.

High signal-to-noise (S/N) Échelle spectra of τ Sco (HR 6165), HR 3055, HR 1861, HR 2928, HR 3468, and HR 5285 were obtained by M. Altmann using FEROS (Fiberfed Extended Range Optical Spectrograph, Kaufer et al. 1999) on the ESO 2.2m telescope in La Silla. The data reduction (Appendix A) was performed within the FEROS context in the ESO MIDAS package, using optimum extraction. The spectra were normalised by fitting a spline function to carefully selected continuum points. This suffices to retain the line profiles of the Balmer lines in these early-type stars. Finally, the spectra were brought to the wavelength rest frame by cross-correlation with an appropriate synthetic spectrum. Of the entire wavelength range covered by FEROS, only the part between ∼3800 and 8000 Å meets the quality criteria of this work for further analysis. The spectra are compromised by the lower sensitivity of the instrument at shorter wavelengths, and the reduced stellar fluxes in the far red. FEROS provides a resolving power $R \simeq \lambda/\Delta\lambda \approx 48\,000$, with 2.2 pixels per $\Delta\lambda$ resolution element. An S/N of up to ∼800 is achieved in B. With respect to resolution and signal-to-noise ratio, the spectra available to us are of much higher quality than in typical studies of OB stars, basically excluding observational uncertainties from the error budget.

A supplementary high-S/N spectrum of HR 1861, also covering the higher Paschen series, was obtained using FOCES (Fibre Optics Cassegrain Echelle Spectrograph, Pfeiffer et al. 1998) on the Calar Alto 2.2m telescope. The data were processed in a standard way, using the data reduction routines described by Pfeiffer et al. (1998). An $R \simeq 40\,000$ (2 pixels per $\Delta\lambda$ resolution element) was achieved. In addition, a high-S/N spectrum in the K-band of τ Sco taken with Subaru/IRCS ($R \simeq 12\,000$) is available for analysis; see Hanson et al. (2005) for details on the observations and data reduction. Finally, a high-S/N spectrum in the λ 2.058 μm region of τ Sco taken with UKIRT/CGS4 ($R \simeq 19\,000$) is also available for analysis (Zaal et al. 1999). Additional IUE fluxes and Johnson and 2MASS magnitudes are also employed for constraining the atmospheric parameters, in particular the effective temperature of the programme stars.

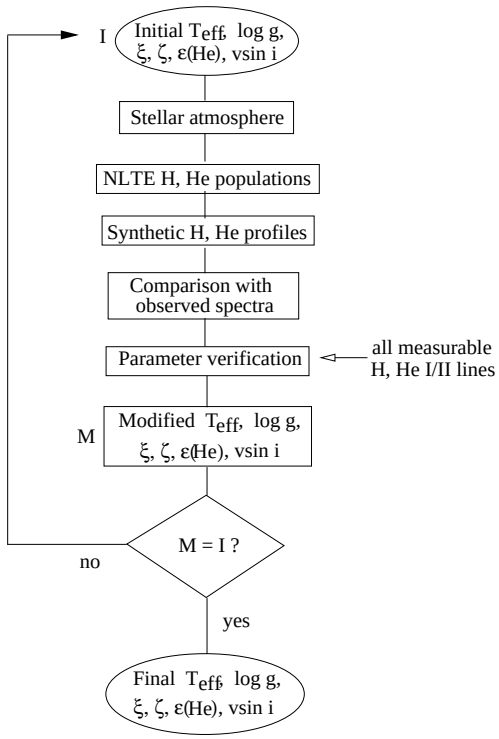

Figure 5.2: Scheme of the iterative procedure for obtaining a simultaneous fit to the hydrogen and helium lines.

5.3 Applications to Observations

Theoretical profiles were fitted to observations in an iterative procedure summarised in Fig. 5.2. The final atmospheric parameters $T_{\rm eff}$ and $\log g$, projected rotational velocities $v \sin i$, and micro- and macroturbulent velocities (ξ, ζ) coincide with those derived from C II/III and C II/III/IV ionization equilibria (Chapter 6). The parameters are summarised in Table 5.1. They are are also able to reproduce the IUE fluxes and Johnson and 2MASS magnitudes, displayed in Fig. 5.3. The observed fluxes are dereddened by the values indicated using a reddening law according to Howarth (1983) and Seaton (1979) assuming a ratio $R_V = A_V/E(B-V) = 3.1$ as typical for the local ISM. They were degraded to the resolution of the ATLAS9 model fluxes. The models are normalised to the observed Johnson V magnitudes and shifted for clarity relative to each other.

The impact of stellar parameter variations on non-LTE profile fits to Hγ, He I λ4026 Å, and He II λ5411 Å in the hot giant HR 3055 is visualised in Fig. 5.4. Two values for the parameter variations are adopted, according to the uncertainties of 300 K/0.05 dex in $T_{\rm eff}/\log g$ and typical values from the more recent literature (1000 K/0.10 dex). All other hydrogen Balmer and helium lines react in a similar way. The sensitivity of the hydrogen and He I lines to parameter variations is low, such that the uncertainties cannot be reduced much below the

Table 5.1: Atmospheric parameters of the programme stars

	τ Sco	HR 3055	HR 1861	HR 2928	HR 5285	HR 3468
$T_{\rm eff}$ (K)	32 000	31 200	27 000	26 300	21 500	22 900
$\pm$	300	300	400	400	400	400
$\log g$ (cgs)	4.30	3.95	4.12	4.15	4.20	3.60
$\pm$	0.05	0.05	0.05	0.05	0.05	0.05
ξ (km s^{-1})	5	8	3	3	4	5
$\pm$	1	1	1	1	1	1
$v \sin i$ (km s^{-1})	4	29	12	14	18	11
$\pm$	2	5	1	1	1	3
ζ (km s^{-1})	4	37	...	20	...	20
$\pm$	2	1	...	2	...	2
y (by number)	0.089	0.080	0.089	0.089	0.089	0.089
$\pm$	0.01	0.01	0.01	0.01	0.01	0.01

typical values even for high-S/N observations like the ones presented here. Only the He II lines are highly sensitive to changes in $T_{\rm eff}$ and, to a lesser degree, in $\log g$. However, by taking metal ionization equilibria into consideration (e.g. C II/III or C II/III/IV), which are even more sensitive than He II lines, the parameters can be constrained more accurately.

Projected rotational velocities, micro- and macroturbulence values have also been verified by fitting the carbon lines. Note that the comparatively high macroturbulence in HR 3055 amounts to less than twice the sound speed in the atmospheric plasma. The microturbulence values are typically lower than found in previous work (e.g. Kilian 1992). Differences in $T_{\rm eff}$ and $\log g$ are also found. Solar helium abundances y (by number) are found in all cases.

5.3.1 Visual

Synthetic profiles for a selection of 6 hydrogen Balmer and 18 He I/II lines in the visual are compared with observation for the sample stars in Figs. 5.5 and C.1-C.5 (in Appendix C). They constitute the best simultaneous fits to the measurable H and He lines in the available spectra achieved in this work. Preference for this selection has been given to (mostly) unblended features with good broadening data. A summary of all available lines is given in Table B.1, where blending species are also identified. The hybrid non-LTE approach (ADS) allows us to reproduce the hydrogen Balmer and He I/II lines in the visual more precisely, with few (well-understood) exceptions. The ionization equilibrium of He I/II puts tight constraints on $T_{\rm eff}$ in the two hotter stars. For the hottest dwarf of the sample, τ Sco, a very good match between model and observation is achieved (Fig. 5.5), except for the cores of Hα and He II λ4686 Å. This is because of the neglect of

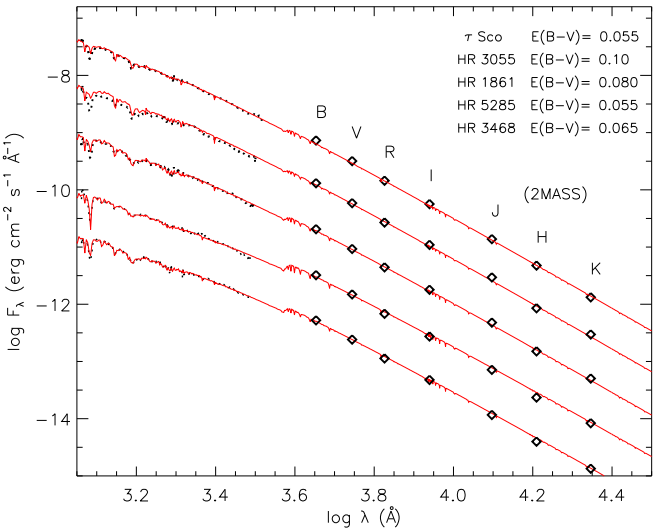

Figure 5.3: Best fits of theoretical energy distributions to measurements by IUE (dotted lines) and Johnson and near-infrared 2MASS photometry (diamonds) from the UV to the near-IR. For atmospheric parameters see with Table 5.1.

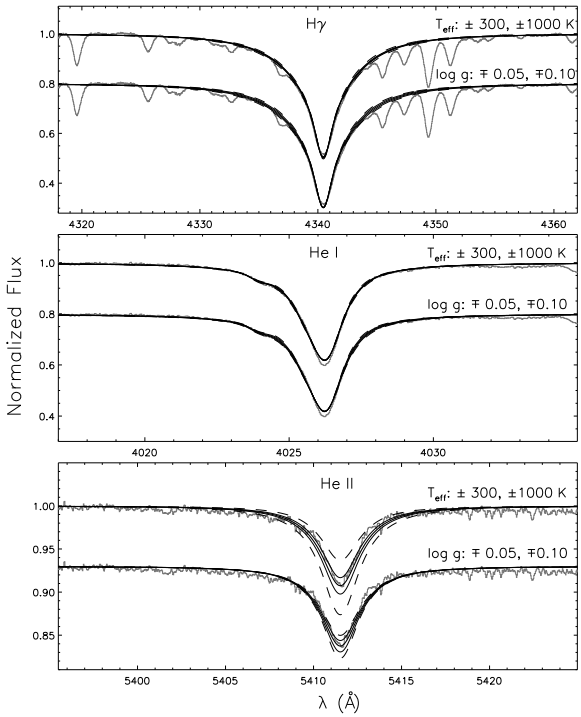

Figure 5.4: Impact of stellar parameter variations on non-LTE profile fits, exemplarily for Hγ, He I λ4026 Å, and He II λ5411 Å in HR 3055 (B0 III). Synthetic spectra for the final parameters (see Table 5.1, thick line) and varied parameters (thin lines for the uncertainty estimates and dashed lines for values typically found in the literature) are compared to observation.

the stellar wind; see Przybilla & Butler (2004) and Mokiem et al. (2005) for results of hydrodynamic computations. The discrepancies in He I λ4121 Å occur because of blends with metal lines (O II, C III, and Fe III; unaccounted for in the present computations), which can be nicely resolved at this low $v \sin i$. An improved fit to He I λ4921 Å may be obtained with better broadening data for the forbidden component.The spectral region around Hα suffers from artifacts introduced by CCD defects that can only partially be compensated in the data reduction process.

Line fits to the hot giant HR 3055 are displayed in Fig. C.1. Excellent agreement between theory and observation is also found in this case, with a significantly improved fit quality of Hα and He II λ4686 Å, because of an apparently weaker wind. This star shows a higher $v \sin i$ and ζ than τ Sco. Therefore the He I λ4121 Å blend is no longer resolved, leading to an apparently worse fit.

He II λ4686 Å is the only visible (weak) feature of He II in the intermediate temperature stars HR 1861 and HR 2928; see Figs. C.2 and C.3. Good fits are obtained for this line and the features of He I (i.e. establishing the ionization equilibrium) and hydrogen. Lines of He II are absent at even lower temperatures, HR 3468 and HR 5285 in the sample; see Figs. C.4 and C.5.

5.3.2 Near-IR

Additional spectra are available in the near-IR for two stars. An excellent fit to the higher Paschen series is obtained for HR 1861 in non-LTE, despite the relatively low S/N and the presence of telluric lines[1], see Fig. 5.6. Good agreement between the non-LTE spectrum synthesis and observation can also be obtained for the He I λ 2.058 μm feature and practically perfect agreement for the λ2.11 μm lines in τ Sco, see Figs. 5.7 and 5.8. Note that the λ 2.058 μm transition is situated in an atmospheric window with a series of strong telluric lines, therefore its shape is highly sensitive to the detailed approach in the data reduction process (see e.g. Zaal et al. 1999). The two different observations in Fig. 5.7 may exemplify the difficulty of accurate telluric line removal in the data reduction process (or alternatively an intrinsic time variability of the feature). Good agreement with the synthetic spectra is obtained in the case of the higher-resolution UKIRT/CGS4 spectrum. The LTE approach is not even able to reproduce the observation qualitatively. The line fits in the near-IR are based on the same atmospheric parameters (Table 5.1) as used for the modelling of the optical spectra.

Non-LTE effects can be amplified in the Rayleigh-Jeans part of the spectral energy distribution, as demonstrated in this case. See e.g. Przybilla & Butler (2004) for a discussion and for line fits to Brγ in the K-band and to additional Brackett and Pfund lines in this star. The case of He I λ10 830 Å has been discussed by Przybilla (2005).

[1]Lines or bands in the spectrum of an astronomical object that are due to absorption by gases such as molecular oxygen, water vapour, or carbon dioxide in Earth's atmosphere.

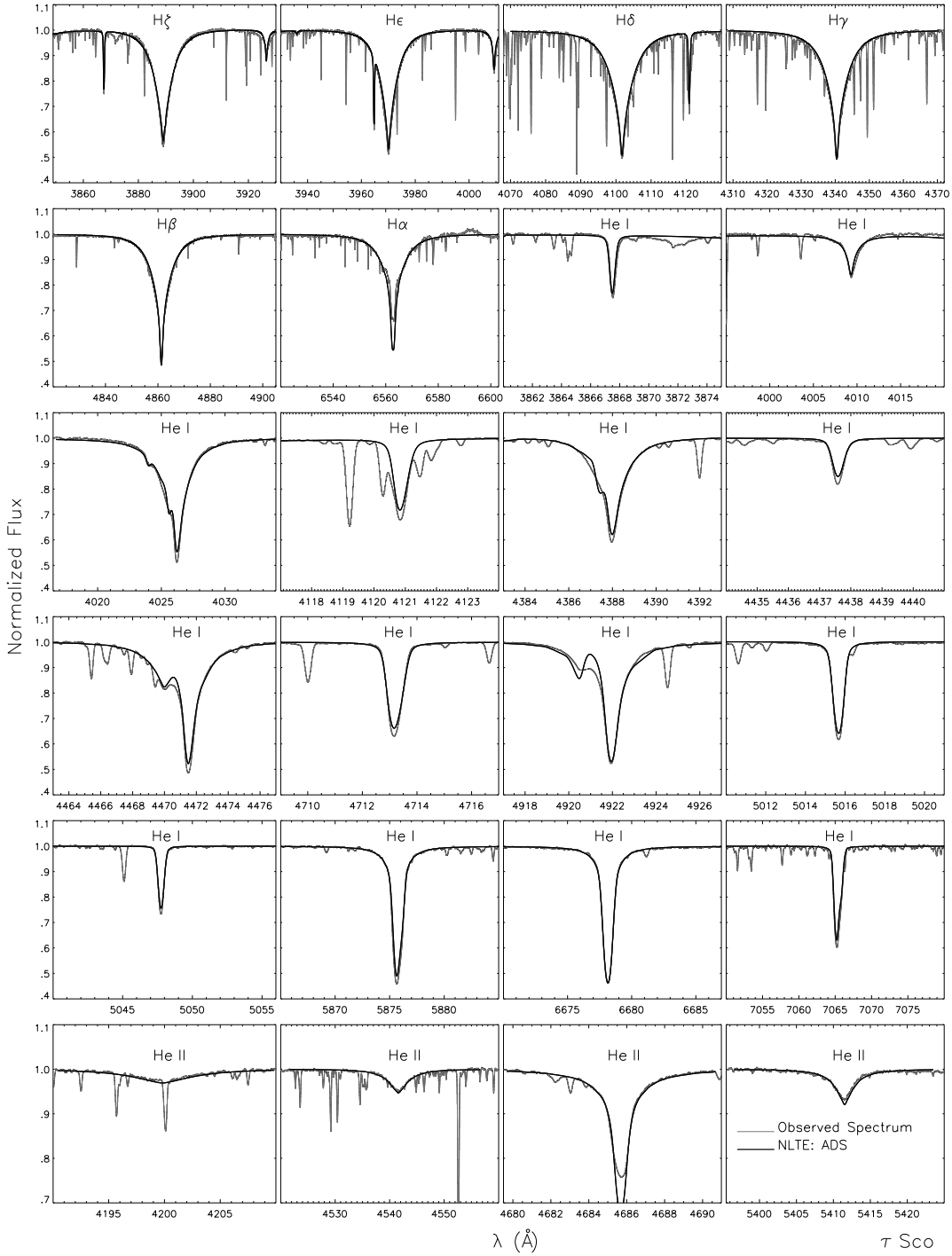

Figure 5.5: Non-LTE line fits to observed hydrogen and helium features in τ Sco (B0.2 V), based on the atmospheric parameters summarised in Table 5.1.

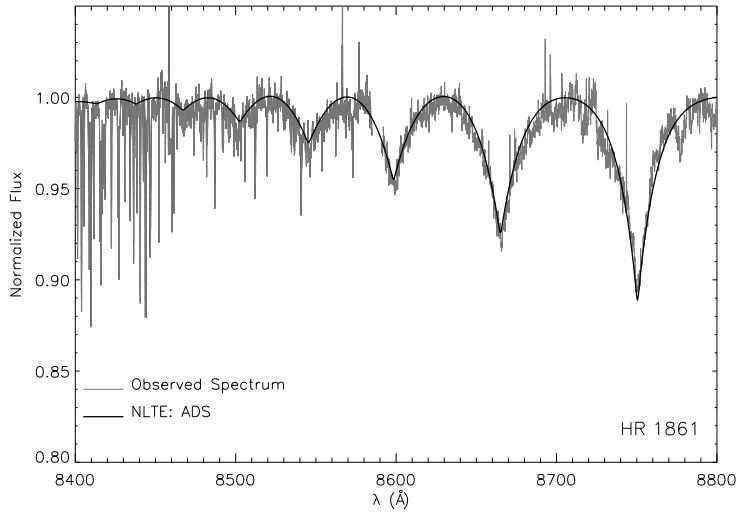

Figure 5.6: Modelling of the Paschen series of HR 1861 with the non-LTE (ADS) approach. Note the presence of numerous sharp telluric H_2O lines. All theoretical spectra in the near-IR have been computed with the same atmospheric parameters than the models in the visual.

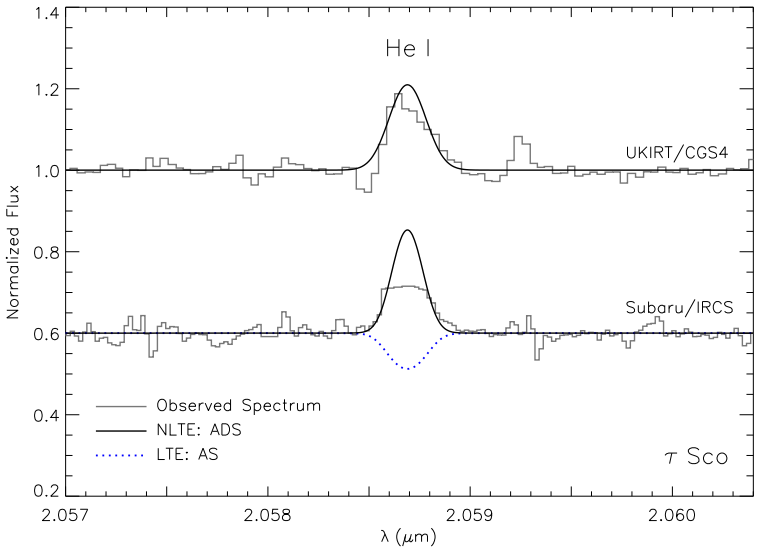

Figure 5.7: Modelling of the He I $\lambda 2.058\,\mu$m singlet line in τ Sco.

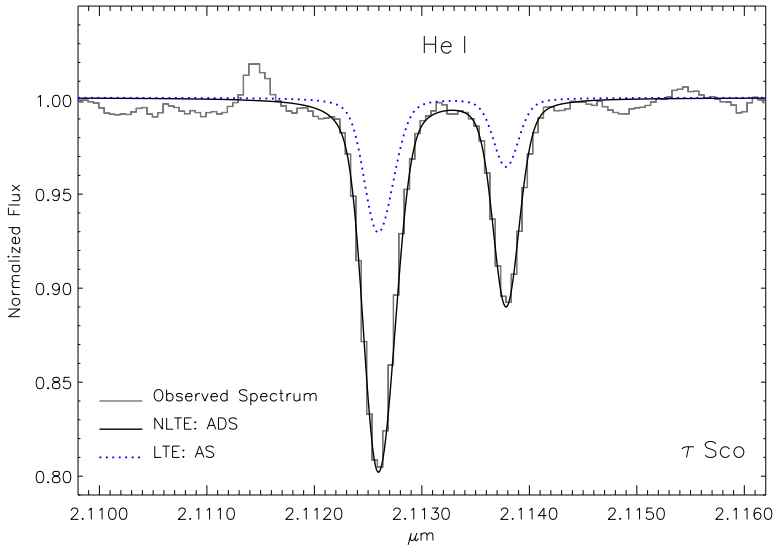

Figure 5.8: Modelling of the He I $\lambda 2.11\,\mu$m singlet and triplet feature in τ Sco. As also shown in Fig. 5.7, these near-IR transitions experience stronger non-LTE effects than the spectral lines in the visual.

5.4 Comparison to Other Model Predictions

In this section, the hybrid non-LTE computations (ADS) are compared with four other approaches. Two of them are available grids from the literature, and to understand their discrepancies to the ADS computations, additional non-LTE and LTE models are calculated.

i) The ATLAS9 models are replaced by line-blanketed, plane-parallel, and hydrostatic non-LTE model atmospheres taken from the publically available OSTAR2002 grid (Lanz & Hubeny 2003, LH03) and the non-LTE line-formation calculation is performed with DETAIL and SURFACE as described above.

ii) Non-LTE calculations provided in the OSTAR2002 grid (TLUSTY and non-LTE line formation with SYNSPEC) and published by LH03 are taken.

iii) LTE spectra based on ATLAS9 atmospheres and subsequent LTE spectrum synthesis with SURFACE (AS) are computed.

iv) The Padova grid (Munari et al. 2005) is considered. These computations are based on ATLAS9 atmospheres and LTE spectrum synthesis performed with the SYNTHE code (Kurucz & Avrett 1981; Kurucz 1993c).

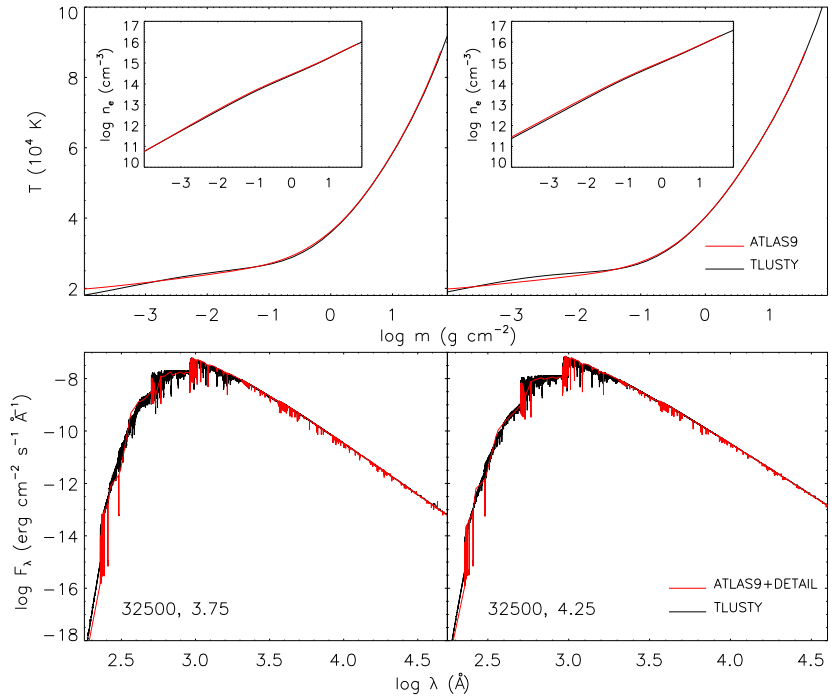

Figure 5.9: Upper panel: Comparison of ATLAS9 and TLUSTY temperature structures and electron densities (insets) as function of column mass. The computations have been performed for giant and dwarf models. Lower panel: Comparison of spectral energy distributions, the radiation field computed by DETAIL on the basis of the ATLAS9 atmospheric structure vs. TLUSTY.

5.4.1 Atmospheric Structures, SEDs: LTE vs. non-LTE

A comparison of LTE (ATLAS9) and non-LTE (TLUSTY) atmospheric structures and of spectral energy distributions (SEDs) computed with ATLAS9+DETAIL and TLUSTY is made in Fig. 5.9. Models for a hot giant and a dwarf ($T_{\rm eff} = 32\,500$ K, $\log g = 3.75$ and 4.25, respectively) are considered, approximately delineating the upper temperature boundary of the observations (τ Sco). Reduced non-LTE effects can be expected for cooler models.

Excellent agreement is found for the temperature and density structures. This is a basic requirement for successful application of the hybrid non-LTE approach for spectrum synthesis. The temperature structures deviate by less than 1% in the inner atmosphere, including the regions where the weaker lines and the wings of the stronger features are formed ($\log m \gtrsim -1$; see Sect. 5.4.3). At the formation depths of the cores of the stronger H and He lines ($-3 \lesssim \log m \lesssim -1.5$) the differences may increase to $\lesssim$2–3%. Stronger deviations may occur only in the outermost parts of the atmosphere, outside the line-formation depths. Note that this good a match is obtained only if the effects of metal line-blanketing

are correctly accounted for. In particular, the computations should be made for identical metal abundances. This is complicated by the fact that the ODFs of Kurucz (1993a) were computed assuming scaled solar abundances from Anders & Grevesse (1989), while the TLUSTY computations assume abundances from Grevesse & Sauval (1998). The most important difference is a downward revision of the iron abundance by $\sim$0.2 dex in the later work. Consequently, ODFs with correspondingly 'sub-solar' metallicity are used in order to correct for the discrepancies in the line opacities, with [Fe/H] as a metallicity substitute. See also Przybilla et al. (2006a) for a discussion of such 'empirical' corrections. We should note that, while the differences are small at (near-)solar abundances, the non-LTE effects on the atmospheric structure will increase with decreasing metallicity. Nevertheless, this hybrid non-LTE methodology for OB star analyses should be applicable down to SMC metallicity, as indicated by an analogous comparison for models at $1/5 \times$ solar abundances.

The SEDs computed with ATLAS9+DETAIL and TLUSTY show excellent agreement over almost the entire wavelength range. Small differences occur in the EUV, most notably in the He II continuum. This is a significant improvement over the comparison of TLUSTY with ATLAS9 model fluxes (not shown here), which predict much lower fluxes in the Lyman and helium continua. The LTE computations neglect the non-LTE overionization of the hydrogen and He I ground states. This overionization reduces the bound-free continuum opacity; see Sect. 5.4.3 for a more comprehensive discussion.

5.4.2 Spectra: Hybrid non-LTE vs. non-LTE and LTE

Comparisons of synthetic profiles of several strategic lines of hydrogen and He I/II are made for three test cases, where models are available from the published grids. These frame the parameter space studied in the present paper. The test cases comprise a hot dwarf model ($T_{\rm eff} = 35\,000$ K, $\log g = 4.5$), at slightly higher $T_{\rm eff}$ than covered by the observations[2], shown in Fig. 5.11; a hot giant model (32 500, 3.75), with similar temperature to τ Sco, see Fig. 5.12; a cool giant model (20 000, 3.00), with both $T_{\rm eff}$ and $\log g$ lower than covered by the observations, Fig. 5.13. In order to be consistent with the published grids, the present computations consider solar metal abundances (Grevesse & Sauval 1998) and solar helium abundance. Our synthetic spectra and those of the OSTAR2002 grid are degraded to the highest resolution ($R = 20\,000$) available from the Padova grid. Note that metal lines are neglected when the emergent spectrum is calculated, but they are considered indirectly via line blanketing/blocking effects.

i) ADS vs. TLUSTY-DS. This comparison allows effects caused by differences in the model atmosphere structures to be disentangled. A practically perfect match

[2]This approach is expected to be valid at slightly hotter temperatures, at least in main sequence stars where the stellar wind does not influence the photospheric layers strongly.

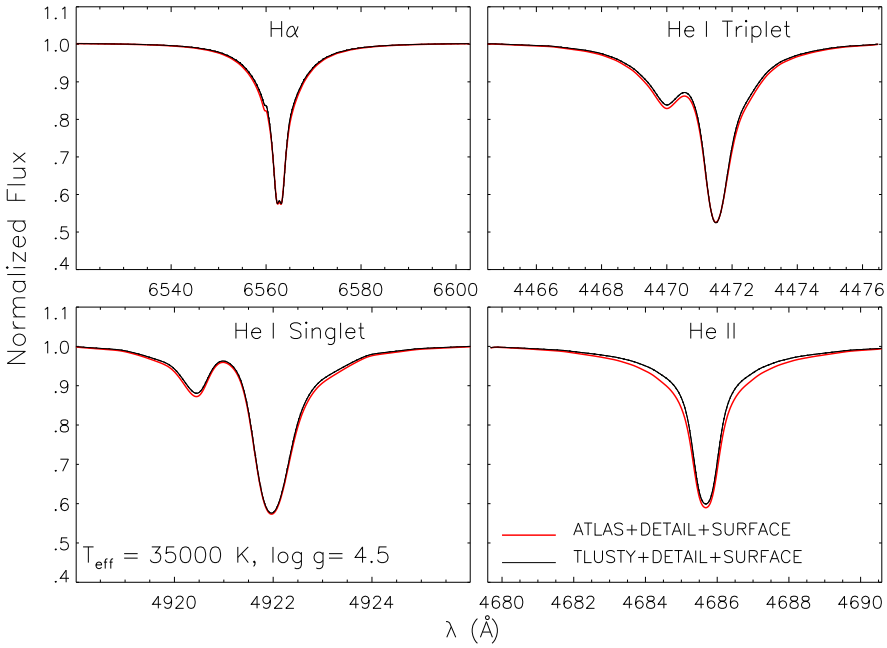

Figure 5.10: Comparison of the most discrepant hydrogen and He I/II line profiles from the hybrid non-LTE approach (ADS) and a TLUSTY-DS calculation for a hot main-sequence model. Practically perfect agreement is obtained, with small discrepancies occurring only in the wings of He II λ4686 Å.

for the (35 000,4.5) model (see Fig. 5.10) is obtained in the ADS and TLUSTY-DS computations, which share the same model atom. This indicates good agreement of the LTE and non-LTE atmospheric structures at even slightly higher temperatures than discussed in Fig. 5.9. The discrepancies are even smaller at lower temperatures.

II) ADS vs. TLUSTY+SYNSPEC (LH03). These results are obtained using two independent methods (model atmospheres, model atoms, numerical solution). Nonetheless, good agreement is found on the whole for the (35 000,4.5) and (32 500,3.75) models from an inspection of Figs. 5.11 and 5.12, respectively. Notable differences between ADS and TLUSTY+SYNSPEC occur in the line cores of the Balmer lines (the latter filled in by emission) and in the He I singlet lines, which are systematically weaker in the case of TLUSTY+SYNSPEC, in contrast to observation (see Figs. 5.5 and C.1). The He I triplet lines derived from both approaches agree well. Small discrepancies occur in the line wings of the He I lines because of different broadening data. A good match is also obtained for the He II lines, with small differences arising in He II λ4686 Å.

From the comparison of the TLUSTY+SYNSPEC and TLUSTY-DS results, which match ADS, we can conclude that the aforementioned discrepancies arise because of subtle differences in solving the statistical equilibrium and radiative transfer problem. While the present approach uses LTE line opacities averaged over

the ODF wavelength bins, the TLUSTY+SYNSPEC computations employ a more sophisticated non-LTE opacity sampling technique. This, however, introduces a strong dependency on the model assumptions for Fe IV[3] (a highly complex ion), which has lines overlapping with an He I resonance transition (Najarro et al. 2006)[4]. The same model atmosphere (TLUSTY) is used and both model atoms should be sufficiently robust for modelling the lines in the visual; see Przybilla & Butler (2004) and Przybilla (2005) for a discussion of this.

III) ADS vs. ATLAS9+SURFACE. LTE computations with AS produce narrower Balmer lines for the (35 000,4.5) and (32 500,3.75) models (the differences reducing progressively from Hα to the higher series members), which leads to overestimated surface gravities in that case. At the same time, *all* He I lines are too shallow in LTE, the trend increasing from blue to red and showing larger discrepancies at lower gravity. On the other hand, rather good agreement is found for the He II lines, the LTE predictions being slightly weaker than ADS for the hot giant. In Fig. 5.13 a comparison of the hybrid non-LTE with our pure LTE prediction is made for a (20 000,3.0) model with a temperature slightly below than the lower limit of the programme stars, and at significantly reduced surface gravity. Here, the wings of the Balmer lines show much better agreement than at higher temperatures (cf. Fig. 5.11), as well as the He I $\lambda\lambda$ 4437 and 4713 Å lines. The line cores are also discrepant, increasingly so from Hδ to Hα. Many of the He I lines experience significant non-LTE strengthening, in particular those in the red. The line broadening data is the same in ADS and AS, so the He I wings are very similar. The forbidden components are also accounted for in both approaches.

IV) ADS vs. ATLAS9+SYNTHE (Munari et al. 2005). The differences of these approaches were quantified for the (35 000,4.5) model, when possible. The Balmer lines from the Padova model present similar characteristics as the LTE AS approach (in Fig. 5.11 they coincide), resulting in lower equivalent widths by up to $\sim$30% relative to ADS. When using the Hγ wings as a surface-gravity indicator, this translates to a systematic error in $\log g$ by $\sim$0.2 dex, implying even larger errors for fits to the Hβ and Hα wings. The He I lines are generally too weak, by up to a factor of more than 2 in equivalent width, and the He II lines too narrow. For the most part, these discrepancies stem from the neglect of non-LTE effects on the line-formation process, as the differences in the atmospheric structures are practically insignificant.

[3]In particular on the oscillator strengths of the Fe IV transitions involved. A reduction of the gf-values may alleviate the discrepancy between the He I singlet and triplet line strengths, seen, for example, in the OSTAR2002 grid.

[4]As a further test we have calculated synthetic spectra for the (35 000,4.5) and (32 500,3.75) models on the basis of unified, line-blanketed non-LTE model atmospheres (FASTWIND, Puls et al. 2005). Excellent agreement with ADS results is found for both the He I singlet and triplet lines. Note that FASTWIND also uses an approximate treatment of line blocking.

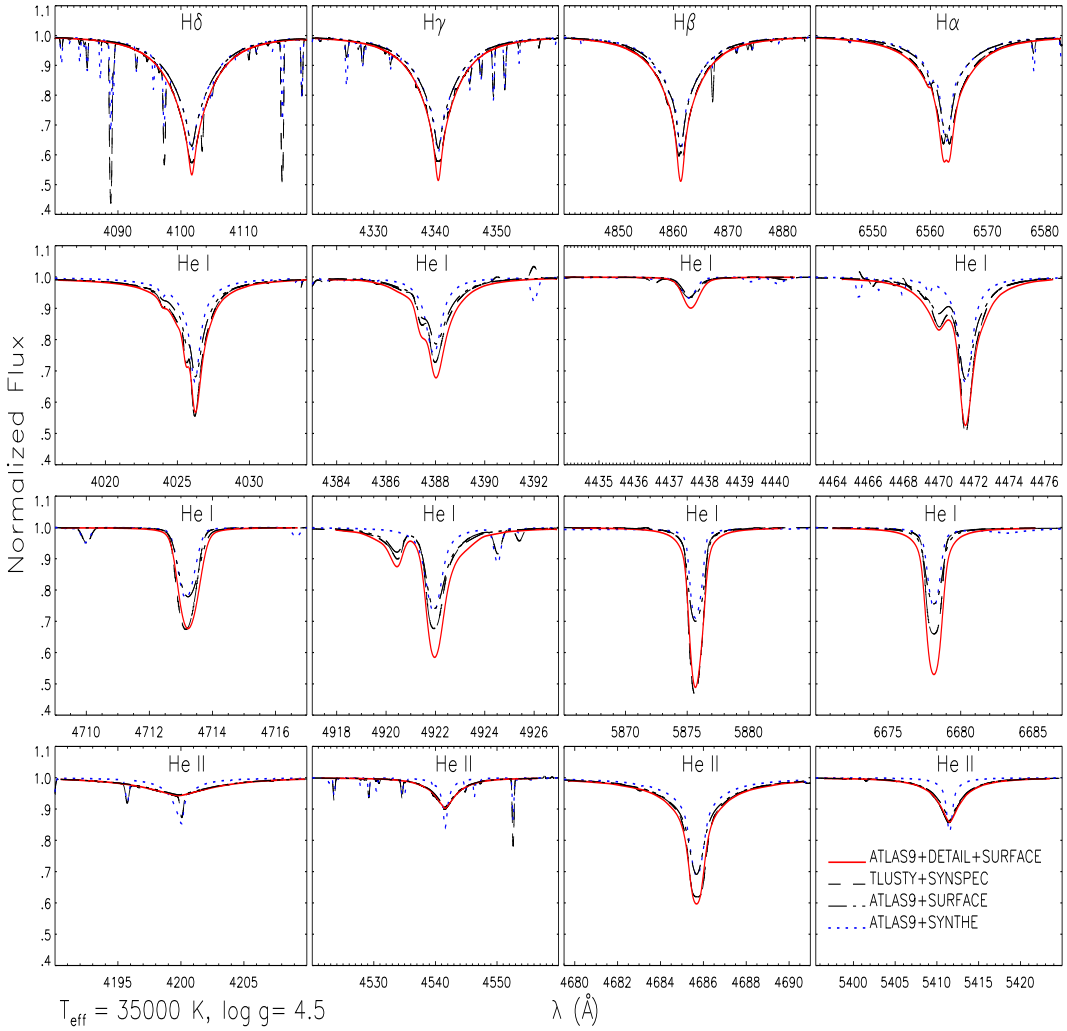

Figure 5.11: Comparison of selected H and He I/II line profiles from the hybrid non-LTE approach (ADS), non-LTE computations from TLUSTY+SYNSPEC, and two LTE calculations (ATLAS9+SURFACE and ATLAS9+SYNTHE) for a hot main-sequence model.

Another limiting factor of the ATLAS9+SYNTHE computations is the use of insufficient Stark broadening data (Voigt profile with constant Stark damping parameter). The AS and ADS approaches improve on this, as realistic broadening data is used (see Table B.1). In the ATLAS9+SYNTHE approach, it will not be possible to obtain reasonable agreement for the He I and He II spectra at the same time. For the (20 000,3.0) model, the Padova profiles are more similar to the AS approach. However, the diffuse He I lines still suffer from inappropriate broadening data, in particular the forbidden components are unaccounted for. The He I lines are affected by non-LTE strengthening, increasing to the red. Only few

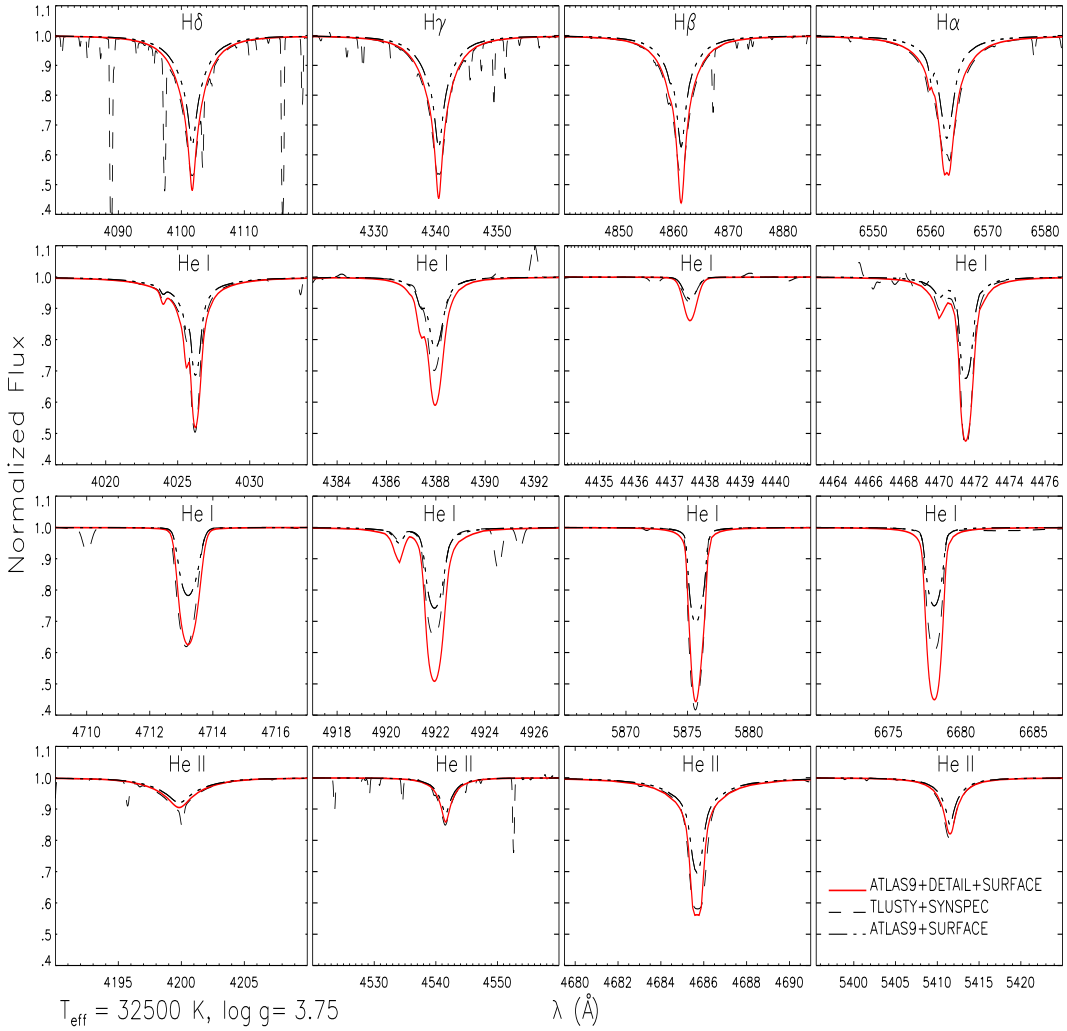

Figure 5.12: Comparison of selected H and He I/II line profiles from the hybrid non-LTE approach (ADS), the non-LTE computations with TLUSTY+SYNSPEC and the LTE approach ATLAS9+SURFACE for a hot giant model. Here, HR 3055 may act as observational discriminator, indicating our results to be appropriate (see Fig. C.1).

He I lines are quite similar in the three approaches: $\lambda\lambda$4437 and 4713 Å match quite well, as do $\lambda\lambda$3867, 4121 (despite blends with metallic lines) and 5015 and 5047 Å, not displayed here.

The published libraries of synthetic spectra were computed with different values of microturbulent velocity (OSTAR2002: $10\,\mathrm{km\,s^{-1}}$; Padova: $2\,\mathrm{km\,s^{-1}}$). The ADS and TLUSTY-DS calculations with $\xi = 10\,\mathrm{km\,s^{-1}}$ were adopted for the comparison in Fig. 5.11. Tests with a reduced $\xi = 2\,\mathrm{km\,s^{-1}}$ were made, resulting in only small changes in the He II profiles – the most sensitive to modifications of ξ.

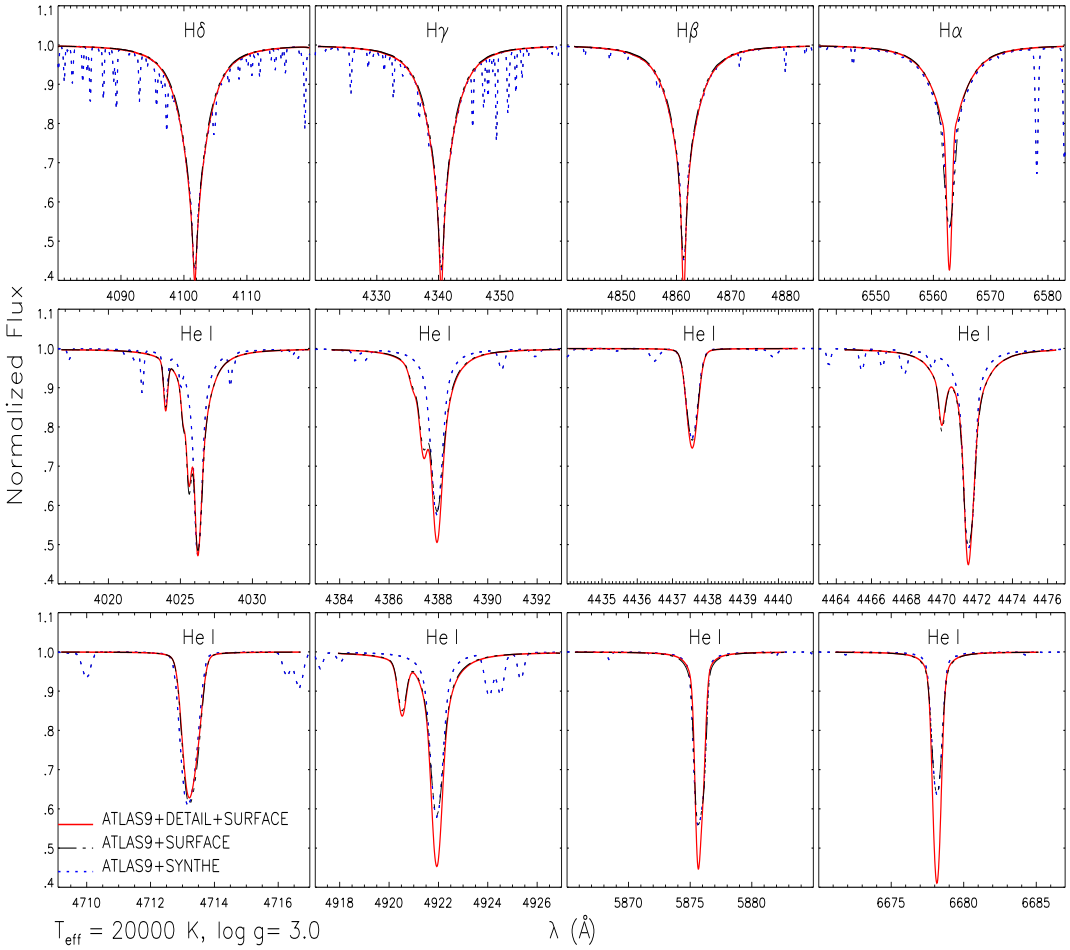

Figure 5.13: H and He I profiles for a cool giant model: the hybrid non-LTE approach (ADS) vs. the LTE (ATLAS9+SURFACE) and the corresponding Padova model (ATLAS9+SYNTHE); see Fig. C.4 for the closest observational analogue.

The differences between the Padova grid and the other approaches are indeed due to the neglect of non-LTE effects and to additionally insufficient broadening data and not because of discrepant microturbulences. The ADS and AS computations in Figs. 5.12 and 5.13 were performed using the ξ of the respective libraries.

5.4.3 Line Formation: Hybrid non-LTE vs. Full non-LTE

The physical reasons for the differences in the non-LTE line profiles of hydrogen and helium in the last comparisons are studied by a closer study of the underlying line-formation processes. For this, non-LTE departure coefficients and line source functions are investigated for three representative hydrogen and six He I/II lines, as derived in ATLAS9+DETAIL and the TLUSTY computations. The same

models as discussed in Fig. 5.9 are chosen. For the (32 500, 3.75) model, a direct comparison with the resulting line profiles is facilitated by inspection of Fig. 5.12.

For the levels involved in the transitions of interest and the hydrogen and helium ground states, departure coefficients b_i (referred to the ground state of the next higher ion) are displayed in Fig. 5.14. The non-LTE effects on the level occupations give rise to departures of the line source function S_l from the Planck function B_ν; see Fig. 5.15 for a comparison of S_l/B_ν (see Eqn. 2.43) from the ATLAS9+DETAIL and TLUSTY computations. For a given T_eff the non-LTE effects are strengthened with decreasing surface gravity, implying lower particle densities and thus larger mean-free-paths between photon absorptions.

Hydrogen. Three hydrogen lines are studied, Hα, Hβ and Hγ. Departure coefficients for levels $n > 5$ behave similarly to those for $n = 5$, which already traces the behaviour of the continuum closely. Consequently, the line source functions for the higher Balmer lines are similar to that of Hγ. The non-LTE depopulation of the H ground state (Fig. 5.14) reduces the Lyman continuum opacity, giving rise to higher EUV fluxes than in LTE. The Lyman lines are expected to experience non-LTE weakening. Note that the TLUSTY calculations indicate a slightly stronger non-LTE depopulation of the ground state at continuum formation depths than in our case. Good agreement of the departure coefficients for $n = 2$ is found, which is overpopulated at line formation depths. In combination with the higher H states being close to LTE, this explains the non-LTE strengthening of the Balmer lines. At the formation depths of the line cores, in particular for Hα, the TLUSTY results show a less pronounced overpopulation, eventually leading to an underpopulation of the $n = 2$ state in the outer atmosphere. This explains the shallower lines from the TLUSTY computations relative to ADS, which is a consequence of the upturn of S_l/B_ν (Fig. 5.15). The effect decreases from Hα to the higher Balmer lines, as the core formation depths shift to deeper atmospheric layers.

He I Singlets. Two representative features are investigated: $\lambda\lambda$4921 and 6678 Å. In general, the departure coefficients for most of the levels show rather good agreement, in qualitative behaviour as well as quantitatively. Notable differences in the ground-state overionization occur in the outer atmosphere. More relevant is the behaviour of the $2\mathrm{p}\,{}^1\mathrm{P}^\mathrm{o}$ level, the lower level of practically all He I singlet transitions in the visual. The non-LTE overpopulation in the TLUSTY results is far less-pronounced than in our case (Fig. 5.14), in particular for the giant model. This gives rise to discrepant line source functions (Fig. 5.15) and consequently differing line profiles (Fig. 5.12) in the two approaches, with the ADS computations correctly predicting the non-LTE strengthening and thus reproducing observation (Sect. 5.3). The states at higher excitation energies ($n \geq 4$) are in LTE relative to the He II ground state at line-formation depths.

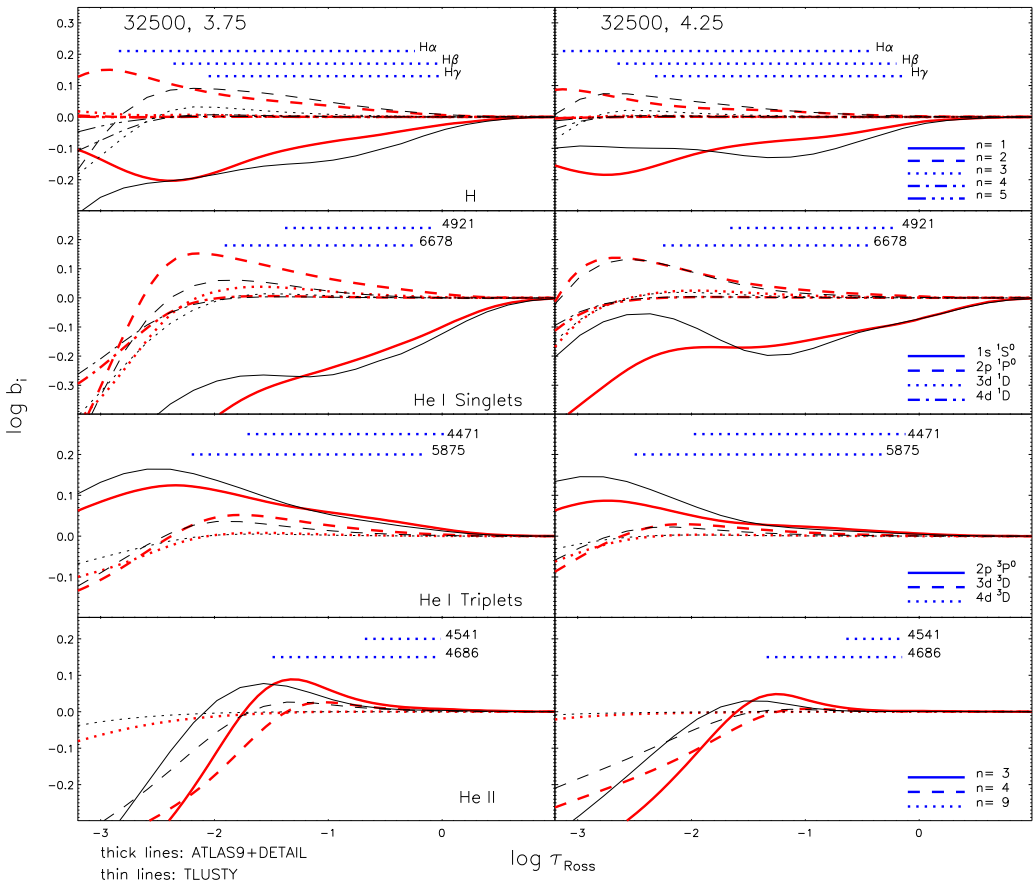

Figure 5.14: Departure coefficients b_i of some strategic hydrogen and helium levels as a function of Rosseland optical depth $\tau_{\rm Ross}$. The comparison is made for the giant (left) and dwarf atmospheric models (right column) already discussed in Fig. 5.9, for the hybrid non-LTE approach (ATLAS9+DETAIL, thick lines) and the results of LH03 (TLUSTY, thin lines). Each level is coded by different line styles; see the legend in the corresponding panels. Line-formation regions (from core to wing) corresponding to our calculations are indicated. See the text for further discussion.

He I Triplets. Two representative lines are studied: $\lambda\lambda$4471 and 5875 Å. The departure coefficients from the two approaches differ only slightly at line-formation depths (Fig. 5.14). As a consequence, the source functions (Fig. 5.15) are also similar, resulting in negligible differences of the line profiles (Fig. 5.12). Again, the states with $n \geq 4$ are in detailed balance relative to the He II ground state at depths relevant for the line formation.

He II. Two features are analysed: $\lambda\lambda$4541 and 4686 Å. The higher He II levels are close to LTE with the continuum state at line-formation depths. Only the

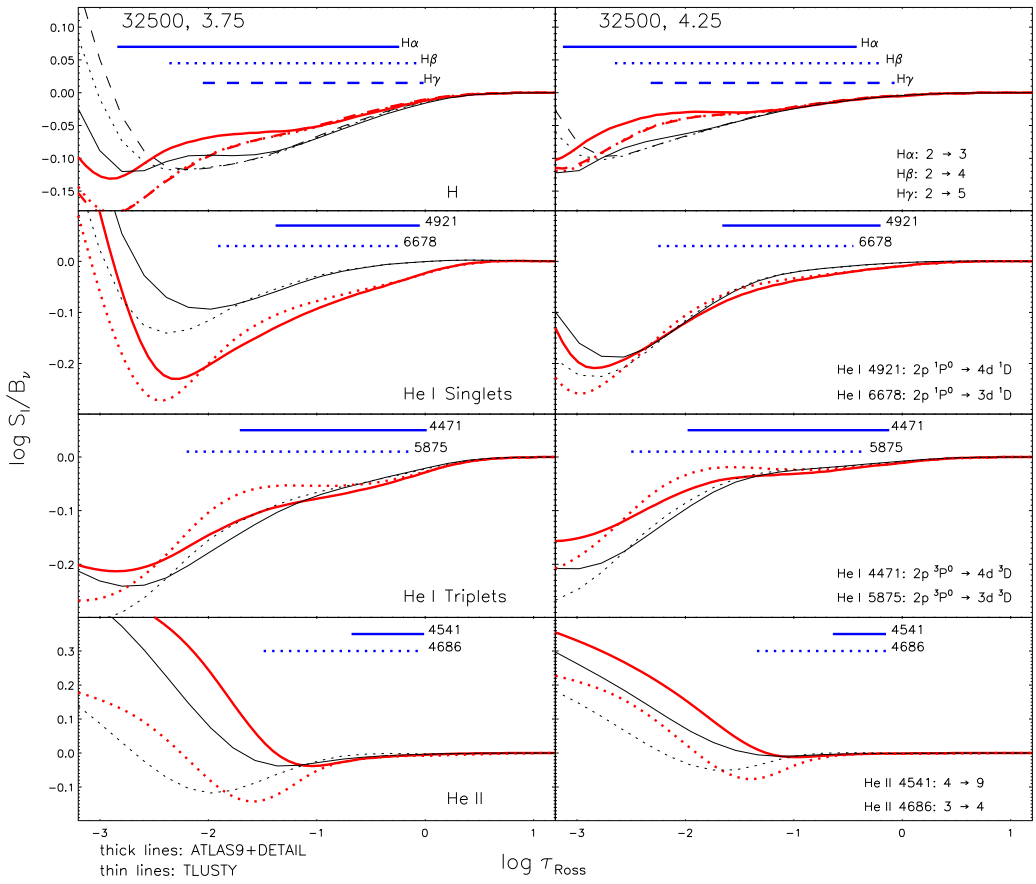

Figure 5.15: Ratio of line source function S_l to Planck function B_ν at line centre as a function of τ_Ross for selected spectral lines of hydrogen and helium. The comparison is made in analogy to Fig. 5.14, for our approach (ATLAS9+DETAIL, thick lines) and LH03 (TLUSTY, thin lines). The individual spectral lines are encoded by the different line styles indicating the line-formation depths. See the text for further discussion.

$n = 3$ level shows a relevant overpopulation, resulting in a non-LTE strengthening of the λ4686 Å line. The differences in the ADS and TLUSTY departure coefficients give slightly shallower profiles for this line in the OSTAR2002 model (Fig. 5.12). The source function for $\lambda\,4541$ Å is essentially Planckian in the relevant region.

5.5 Summary

The suitability of the hybrid non-LTE line-formation computations was studied for quantitative analyses of the hydrogen and helium line spectra of OB dwarf and giant stars. These computations *simultaneously* reproduce the line spectra

throughout the visual and near-IR (where available) at high quality, as well as the measured spectral energy distributions from the UV to near-IR. The only exceptions in the observational sample are the cores of Hα and He II λ4686 Å in τ Sco, because the calculations do not account for stellar winds. For two He I lines blueward of the traditionally analysed spectral region (∼4000–5000 Å), appropriate Stark broadening data is unavailable at present (see Table B.1).

The comparison of state-of-the-art line-blanketed non-LTE and LTE models confirms that the atmospheric structure of OB dwarf and giant stars is described well under the assumption of LTE, but not their spectral energy distribution and also not their line spectra. For these stars in the range $20\,000\,\mathrm{K} \leq T_{\mathrm{eff}} \leq 35\,000\,\mathrm{K}$ and $3.0 \leq \log g \leq 4.5$ (far from the Eddington limit), the hybrid non-LTE approach is equivalent to full hydrostatic non-LTE computations (as partially covered by the OSTAR2002 grid, Lanz & Hubeny 2003). It succeeds also in providing synthetic spectra that correctly reproduce the observed He I singlet lines, avoiding inconsistencies recently reported in the literature.

Computations in LTE from the Padova grid, on the other hand, systematically predict too shallow and/or too narrow line profiles. In particular, the differences in the Hγ wings – a common surface gravity indicator – result in systematically overestimated gravities by up to ∼0.2 dex in LTE (for fixed T_{eff}). The differences in the equivalent widths of the H lines can amount to up to ∼30% and in the He I/II lines up to a factor >2 compared to our non-LTE calculations, with the discrepancies increasing with effective temperature. Nevertheless it is not possible to quantify the differences in effective temperature determinations from non-LTE and LTE ionization equilibria of He I/II, as some of the profiles of the Padova grid do not reproduce observations even qualitatively.

In terms of parameter range and the underlying physics, the hybrid non-LTE approach is certainly restricted. It may be of limited use at higher temperatures (early and mid-O-type stars), lower gravities (early B-type and O-type supergiants), stars with strong winds, or extremely low metallicities. Nevertheless, the hybrid non-LTE approach is sufficient for studying normal OB dwarfs and giants, as it allows the observed line spectra to be reproduced in the visual and near-IR over a wide range of atmospheric parameters. Here it has advantages over other more sophisticated non-LTE techniques: I) it allows highly robust and detailed model atoms to be implemented and to be tested efficiently (i.e. concentration on atomic data while avoiding further complications like stellar winds), e.g. for metals with hundreds of levels and thousands of transitions; and II) the model calculations are fast: the computation of one H & He I/II model with DETAIL+SURFACE takes only a few minutes on a modern PC (as of 2006).

Chapter 6

Non-LTE Line Formation for Carbon: Self-Consistent Analysis

Carbon is a primary element created in the fundamental 3α-process and as such it provides the seed for the subsequent synthesis of all heavier elements (Burbidge et al. 1957; Cameron 1957). Carbon is an essential catalyst for the nucleosynthesis of H into He through the CNO cycle in massive and intermediate-mass stars. The element also constitutes the basis of all organic chemistry.

Carbon abundances derived from early-type stars were the subject of numerous studies over the past decades, with rising improvements in the quality of observed data and the complexity and consistency of the model calculations and spectral analyses. A crucial step in this was to abandon the approximation of local thermodynamic equilibrium (LTE) in line-formation calculations and allow for deviations (non-LTE). Several non-LTE model atoms have been discussed in literature (Lennon 1983; Eber & Butler 1988; Grigsby et al. 1992; Sigut 1996; Lanz & Hubeny 2003, 2007). In particular the model atom of Eber & Butler found wide application for abundance analyses of mostly unevolved early-type stars in the solar neighbourhood (e.g. Gies & Lambert 1992; Kilian 1992; Cunha & Lambert 1994; Gummersbach et al. 1998; Daflon et al. 1999, 2001ab).

Only few optical transitions may be used for abundance determinations of carbon in many (extragalactic/fast-rotating) early-type stars because of S/N-constraints or rotational smearing. This includes the strong C II $\lambda\lambda$6578/82 Å and in particular the 4267 Å multiplet, which is known to pose a challenge to non-LTE line-formation calculations (e.g. Lambert 1993; Sigut 1996). These two multiplets usually fail to reproduce observation consistently (e.g. Grigsby et al. 1992; Hunter et al. 2007), and they are reported to give systematically lower abundances than derived from other, weaker C II lines (Gies & Lambert 1992). Observed trends for C III lines may also be poorly matched by model calculations (Grigsby et al. 1992). A further complication is the failure to establish the C II/III ionization equilibrium. Differences in abundance from the two ions can amount up to a factor $\sim$5–10 (Daflon et al. 2001b; Hunter et al. 2007). However, there

are even more inconsistencies with published carbon abundances from early-type stars in a broader context that require other explanation, as most of the published studies avoid the lines sensitive to non-LTE effects.

A comparison of the available studies of early B-type stars indicates that present-day carbon abundances in the solar vicinity are highly inhomogeneous (even for stars within a single cluster) and largely sub-solar. This is in contrast to the findings of a uniform abundance in the gas-phase of the interstellar medium (ISM) within 1.5 kpc of the Sun (Sofia & Meyer 2001, and references therein). It cannot be understood from current stellar and Galactochemical evolution models either. Young massive stars that form out of a molecular cloud within a short timescale can be expected to show a homogeneous carbon abundance, which also coincides with that of their surrounding H II nebula. Moreover, this abundance is expected to be higher than that of objects from previous generations of star formation in their neighbourhood, like young ($\leq$2 Gyr) F and G stars, and that of the Sun. In reality, significant systematic differences exist (see e.g. Sofia & Meyer 2001; Herrero 2003), sheding doubt on the reliability of carbon abundances derived from early B-type stars.

In this Chapter a robust C II-IV model atom, empirically calibrated with six apparently slow-rotating early B-type stars from the solar vicinity is presented. The focus lies on the critical selection of the appropriate atomic input data and on a self-consistent derivation of the fundamental atmospheric parameters of the sample stars from ionization equilibria. This results on derived abundances with unprecedented accuracy. As a consequence, it is possible to provide a precise determination of the present-day carbon abundance in the solar neighbourhood.

The Chapter is organised as follows: Section 6.1 describes the model calculations including a description of the carbon model. Section 6.2 describes the empirical model calibration via an extensive and self-consistent iteration and the sensitivity of carbon line-formation calculations to atomic data and atmospheric parameter variations. Section 6.3 summarises the final results for parameters and carbon abundances of individual lines for the sample stars. Section 6.4 provides a comparison of the present results to previous studies. The conclusions on the present-day carbon abundance in the solar neighbourhood are discussed in Sect. 6.5. A summary is given in Sect. 6.6.

6.1 The C II/III/IV Model Atom

The non-LTE line-formation computations for carbon follow the hybrid non-LTE approach, as discussed in Chapter 5. The computational efforts can thus be concentrated on robust non-LTE line-formation calculations.

Non-LTE level populations and model spectra are obtained with DETAIL and SURFACE. Continuous opacities due to hydrogen and helium (for actual abundances) are considered in non-LTE. Line blocking is accounted for in LTE via

Kurucz' ODFs. Microturbulence is consistently accounted for in both steps with DETAIL and SURFACE. Non-LTE level populations for hydrogen and He I/II are computed as explained in Chapter 4. This is a prerequisite for modelling metal lines which overlap with the (broad) hydrogen or helium features. In particular, the C II $\lambda\lambda$6578/82 Å doublet is affected in the present case.

A short summary of the input atomic data for the construction of the C II/III/IV model atom is given in this section. A more detailed description of the motivation for choosing these atomic data will be given in Section 6.2, as this turned out to be critical for the realistic modelling of the observed spectra.

C II. This model ion considers *LS*-coupled terms up to principal quantum number $n = 10$ and angular momentum $\ell = 9$ (66 levels) explicitly in the non-LTE calculations, with all fine-structure sub-levels combined into one. Additional levels up to $n = 14$ are computed in LTE relative to the ground state of C III. Level energies are adopted from Moore (1993), Sigut (1996) and Quinet (1998). The doublet and quartet spin systems are treated simultaneously.

Oscillator strengths (gf-values) from three sources are considered: fine-structure data from *ab-initio* computations using the multiconfiguration Hartree-Fock method in the Breit-Pauli approximation of Froese Fischer & Tachiev (2004, FFT04), data from application of the Breit-Pauli R-matrix method (Nahar 2002a, N02a) and results obtained in the Opacity Project (OP) from the R-matrix method assuming LS-coupling (Yan, Taylor & Seaton 1987). The primary source of gf-values is FFT04, followed by OP and N02a for the remaining transitions. Intercombination transitions are neglected because of very small oscillator strengths.

Photoionizations cross-sections are adopted from the OP (Yan & Seaton 1987) for levels up to $n = 9$ and $\ell = 3$ with a correction of the threshold frequencies to observed values. For the remainder, data from Nahar (2002b: N02b) are used.

Effective collision strengths for electron impact excitation among the lowest 16 LS-states are adopted from R-matrix computations of Wilson, Bell & Hudson (2005, 2007). An empirical increase by a factor two was applied to the $3s\,^2S$–$3p\,^2P^o$ data (see Sect. 6.2.2). Collisional excitation for transitions without data are treated using the Van Regemorter (1962) approximation – in the optically allowed case – and via the semi-empirical Allen (1973) formula in the optically forbidden case. Collision strengths Ω varying between 0.01 ($\Delta n \geq 4$) to 100 ($\Delta n = 0$) are employed, as suggested by evaluation of the detailed data from *ab-initio* computations of Wilson et al. (2005, 2007).

Collisional ionization rates are evaluated according to the Seaton (1962) approximation. Threshold photoionization cross-sections are adopted from OP and N02b, allowing for an empirical correction of one order of magnitude higher for the $6f\,^2F^\circ$ and $6g\,^2G$ levels – corresponding to the upper levels of the C II $\lambda\lambda$6151 and 6462 Å transitions, respectively.

C III. This model accounts for LS-terms up to $n = 7$ and $\ell = 7$ (70 levels) explicitly in the statistical equilibrium calculations. In a similar way to C II, levels up to $n = 14$ are computed in LTE relative to the ground state of the next ionization stage. The two spin systems (singlet and triplet) are treated simultaneously. Level energies are taken from the NIST database[1] and energies for 9 of the highest levels are adopted from N02a. Two sources are considered for oscillator strengths: N02a and additional values from Eber (1987). Intercombination transitions are also implemented when their values are non-negligible ($f > 10^{-4}$). Photoionization cross-sections are taken from S. Nahar's webpage[2]. Maxwellian-averaged collision strengths for electron impact excitation among the lowest 24 terms are adopted from the R-matrix computations of Mitnik et al. (2003). Collisional excitation for the remaining transitions and collisional ionization are treated in analogy to the C II ion, using appropriate gf-values and threshold photoionization cross-sections.

C IV. LS-terms up to $n = 10$ and $\ell = 9$ (53 levels) are treated explicitly. Additional levels up to $n = 14$ are computed in LTE relative to the ground state of C V. Oscillator strengths from *ab-initio* calculations using the Breit-Pauli R-matrix method (Nahar 2002c) are adopted. Photoionization cross-sections are also taken from Nahar's webpage. Effective collision strengths for electron impact excitation of transitions among the lowest 24 fine-structure levels are taken from Aggarwal & Keenan (2004) and subsequently co-added. All remaining transitions, as well as collisional ionization, are treated in analogy to C II.

The resulting C II/III/IV model atom accounts for more than 1300 radiative and more than 5300 collisional transitions, ∼200 LS-coupled energy levels and over 20 000 frequency points – the latter allow the detailed resonance structure of the photoionization cross-sections to be considered. Accuracies of the atomic data can range from a typical 10-20% for *ab-initio* computations to orders of magnitude for approximation formulae. Finally, Voigt profiles are adopted in the formal solution using SURFACE. Wavelengths and oscillator strengths of most of the observed transitions are taken from Wiese et al. (1996). For C II $\lambda\lambda$6151.3/5 and 6461.9 Å the line transition data are adopted from Kurucz & Bell (1995).

Radiative damping parameters are calculated from OP lifetimes and coefficients for collisional broadening by electron impact are adopted from Griem (1974, for the C II λ4267 Å doublet) or computed according to Cowley (1971). Detailed tabulations from quantummechanical computations for Stark broadening of several C IV transitions (Schöning 1993) are also used. The spectral lines used for abundance analysis are listed later in Table 6.3.

[1] http://physics.nist.gov/PhysRefData/ASD/indices.html
[2] http://www-astronomy.mps.ohio-state.edu/∼nahar/px.html

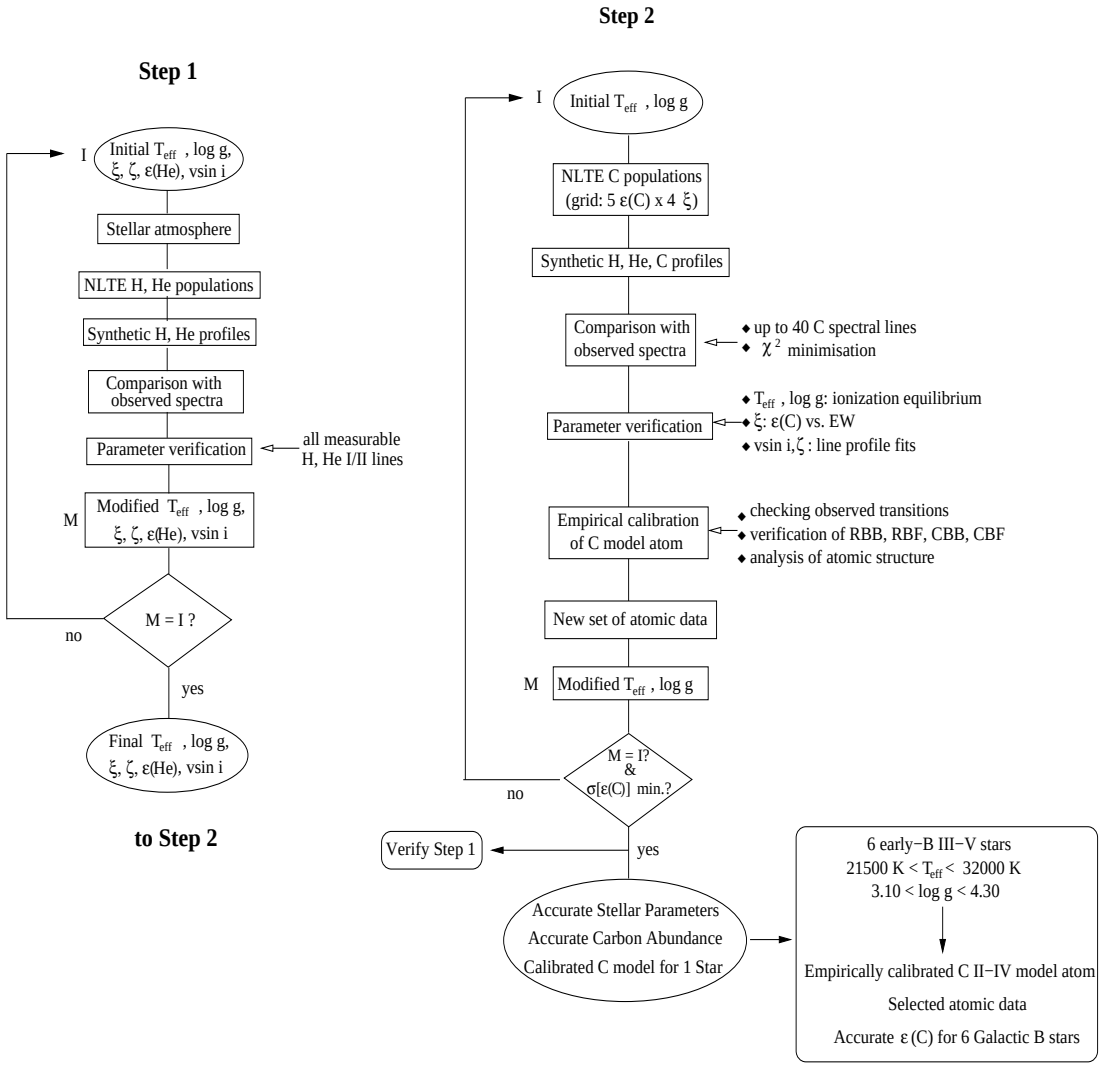

Figure 6.1: Flux diagram of the extensive iterative procedure, as applied to each programme star. The procedure allows the following to be achieved: I) a simultaneous derivation of highly accurate stellar parameters, II) a critical selection of input atomic data from different sources, III) the calibration of the C II-IV model atom and IV) a determination of precise C abundances, with highly reduced systematic errors. RBB/CBB: Radiative/Collisional Bound-Bound, RBF/CBF: Radiative/Collisional Bound-Free transition data. Step 1 is discussed in Chapter 4. See the text for details.

6.2 Model Atom Calibration

Model atoms can be empirically calibrated for non-LTE calculations by demanding that the model reproduce the observations reliably over the entire parameter space of relevance. A basic requirement for a proper model atom calibration is an accurate knowledge of the atmospheric parameters of the test sample stars.

These should be free of systematic errors in order to prevent one from being mislead when optimising the input atomic data. Unfortunately, the parameters of stars are *a priori* not known, they also need to be inferred by interpretation of observation. Consequently, a *simultaneous* solution for all stellar parameters and an optimal set of input atomic data needs to be found. At the same time, those parameters should also allow the hydrogen and helium spectra to be reproduced.

6.2.1 Extensive Iteration on Fundamental Variables

The atmospheric parameter derivation and selection of input atomic data are simultaneously performed in an extensive iteration process. When possible, the effects of the fundamental parameters and the atomic data on the synthetic spectra – the basis for the comparison with observation – are disentangled in order to achieve a better understanding of the problem. This is facilitated by boundary conditions, like the ionization balance (all ionization stages of an element are required to indicate the same abundance) or the rules and regularities of atomic physics.

The iteration is performed on effective temperature $T_{\rm eff}$ and surface gravity $\log g$, as well as micro-, macroturbulent and projected rotational velocities (ξ, ζ and $v \sin i$, respectively), helium and carbon abundances (hereafter ϵ(He) and ϵ(C), respectively) and different sets of atomic data. Only the metallicity is fixed to a standard solar value (Grevesse & Sauval 1998), a not too critical assumption which is furthermore validated *a posteriori* (Przybilla et al. 2007, in preparation). This comprises an enormous number of variables (atmospheric parameters and atomic data) in the iterative scheme summarised as a flux diagram in Fig. 6.1.

The first step concerning the H/He spectrum is solved in Chapter 5. There, the He I/II ionization equilibrium is the main indicator for $T_{\rm eff}$ (for the hotter stars), *all* Balmer lines for $\log g$, the He II lines for ξ and all He lines for ζ and $v \sin i$. The second step, involving carbon, is required for a fine tuning of the atmospheric parameter determination since the metal lines are more sensitive to parameter variations than the hydrogen and helium lines. Therefore it is possible to derive them with a better precision than only from hydrogen and helium but at the same time consistently within the error limits. Effective temperature and $\log g$ are refined by establishing the C II/III/IV ionization equilibrium in the hotter stars and the C II/III ionization balance in the cooler stars. The microturbulent velocity is inferred in the standard way by demanding the carbon abundances of the individual lines to be independent of equivalent width. Macroturbulent and projected rotational velocities are determined by detailed fitting of the carbon line profiles. Line fits are performed on the basis of small grids of synthetic spectra with different ξ and ϵ(C) via χ^2-minimisation.

Since different sets of atomic data are available, they are intercompared and their reliability to minimise the uncertainties in the ϵ(C)-determination is judged. Starting from an initial model atom (based on input data that are supposed to

be the most accurate) a careful analysis of the atomic structure of the model ions and the reactions of the spectrum synthesis to parameter variations is performed. Examples of this are given in the next subsections.

The atmospheric parameters derived from C ionization equilibrium in Step 2 are verified by re-iterating Step 1 as a final check for consistency. By application of the procedure to all programme stars it is possible to calibrate the C II-IV model empirically over the entire parameter range ($21\,500 \leq T_{\rm eff} \leq 32\,000$ K, $3.10 \leq \log g \leq 4.30$, for dwarfs and giants), resulting in a final reference set of atomic data. As a consequence, highly accurate carbon abundances are obtained for the stars of the calibration sample, essentially unbiased by systematic errors.

Note that the high-quality spectra are essential for this success. They allow the analysis of a wide variety of carbon lines to be performed, many of which have never been considered before in the study of early B stars. Some weak lines turned out to be highly sensitive to non-LTE effects and/or to atmospheric parameter variations, namely the C IV lines and C II $\lambda\lambda$6151 and 6462 Å, which change from absorption to emission at higher temperatures. The reproduction of the observed trends despite this high sensitivity puts strong constraints on the robustness of the final model atom. Note also that the presence of lines from three ionization stages, in hotter stars of the sample, allows $T_{\rm eff}$ and $\log g$ to be derived from the ionization equilibrium alone, independent of any other indicators.

To summarise here, the strength of this empirical calibration lies in the simultaneous analysis of the large number of C lines of different ionization stages in stars covering a wide parameter range. In this way it is possible to constrain a final set of atomic data *independent* of any specific stellar atmosphere environment. This reference model can be used in further applications with a simplified iterative scheme, where the only remaining variables are the atmospheric parameters and the C abundance.

6.2.2 Sensitivity of C Lines to Atomic Data

As explained in previous chapters, two kinds of processes produce transitions from one state of an atom to another. Collisions act towards establishing detailed equilibrium *locally*, while radiative processes are *non-local* in character (photons may travel wide distances before interacting with the plasma). LTE is therefore established only when either collisions dominate the plasma or the radiation field is isotropic and Planckian. Such conditions prevail deep in stellar atmospheres, but the strict validity of LTE can not be assumed for the observable layers.

The *line formation* in early B-type stars requires such deviations from LTE to be accounted for in detail. A statistical equilibrium is established, with the radiation field coupling the plasma conditions at each depth in the atmosphere. The non-linear interdependency of radiation field and level populations is the essence of the non-LTE problem. It requires an iterative solution.

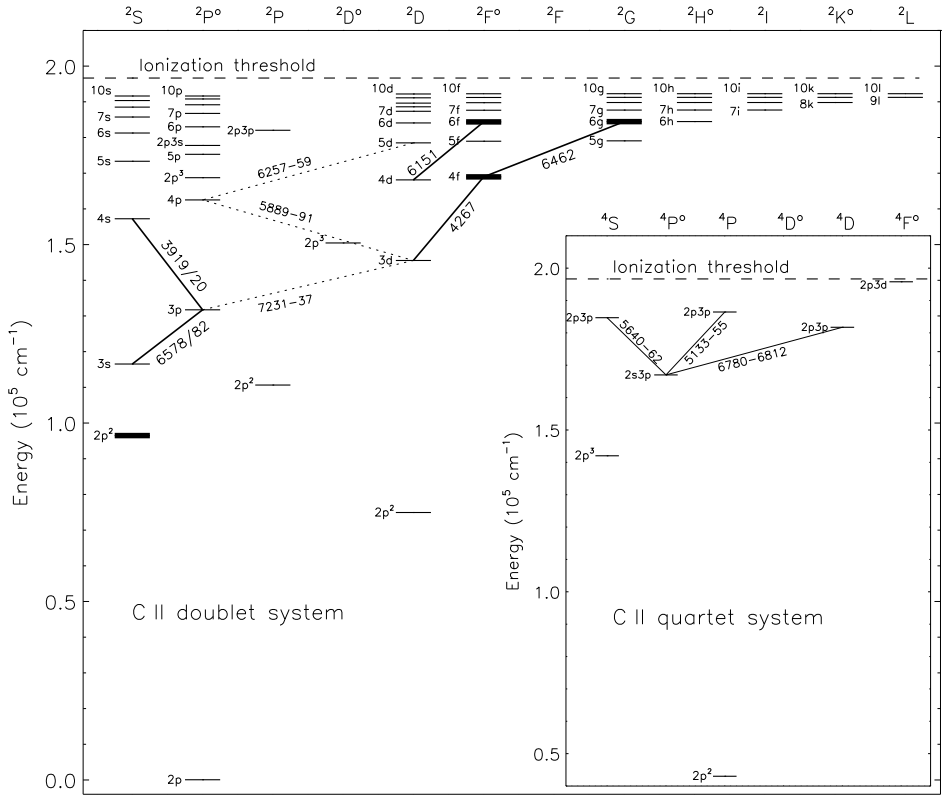

Figure 6.2: Grotrian diagram for the C II doublet and quartet spin systems. Only the observed multiplets in the spectra are identified. *Levels*: those marked in bold correspond to levels discussed in Figs. 6.3 and 6.6. *Multiplet transitions*: those marked by thick lines are highly sensitive to variations of input data for photoionization and collisional cross-sections and for collisional excitation (discussed in Figs. 6.4, 6.6 and 6.7, respectively). The latter and those marked by thin lines are considered in the linelist (Table 6.3) for abundance derivation. Those marked by dotted lines are excluded from the analysis because of contamination with telluric lines ($\lambda\lambda$6257-59, 7231-37 Å) or they are too weak even at low $T_{\rm eff}$ (λ5889-91 Å). Nevertheless they are accounted for in the calculations of the level populations. Autoionizing levels above the ionization threshold are not treated explicitly, but are considered in the statistical equilibrium computations via resonances in the photoionization cross-sections.

The coupled problem of the radiative transfer (Eqn. 2.5) and the statistical equilibrium (Eqn. 2.26) equations allows reliable level populations (a prerequisite for an accurate analysis) to be obtained *only* under strict conditions. I) The local temperatures and particle densities are known (i.e. the atmospheric structure) *and* II) the radiation field is realistic *and* III) all relevant processes are taken into account *and* IV) high-quality atomic data are available (i.e. accurate cross-

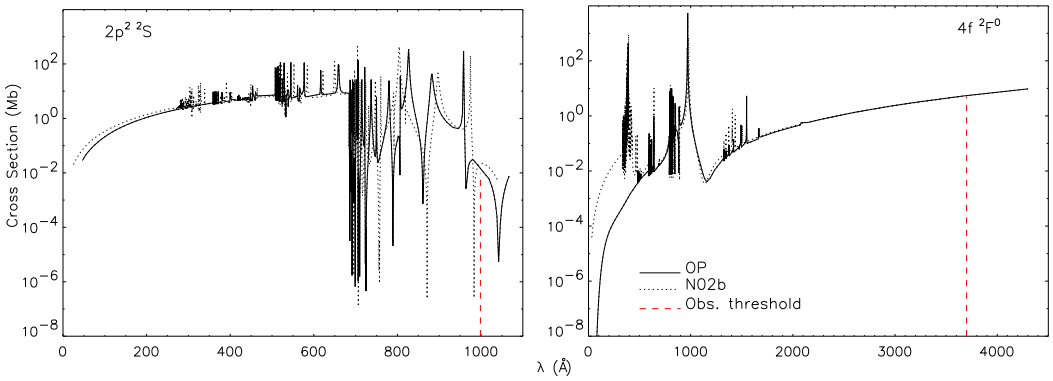

Figure 6.3: Comparison of C II photoionization cross-sections from the Opacity Project (Yan & Seaton 1987) and Nahar (2002b) for $2p^2\ ^2S$ and $4f\ ^2F^o$ as a function of wavelength. See the text for a discussion.

sections for the transitions). In particular, I) and II) require a realistic physical model of the stellar atmosphere (see Chapter 5 for a discussion of the hybrid non-LTE approach in the context of this) and an accurate atmospheric parameter determination. Items III) and IV) are related to the model atoms for the non-LTE calculations. Shortcomings in any of I)–IV) result in increased uncertainties/errors of the analysis.

Because of the interdependency of all transitions (over 6000 in this case) and the non-local character of the radiation field, even a restricted non-LTE problem like the one investigated here becomes highly complex. In particular, it is impossible to quantify *a priori* the sensitivity of the spectral lines to variations of some of the atomic input data. Therefore, one of the few remaining reasons for the large spread of carbon abundances found in literature (see Sect. 6.4) may be different realisations of model atoms (levels/transitions considered, atomic data, approximations). Choosing an optimum set of input atomic data is not trivial and the construction of reliable model atoms for non-LTE calculations requires an empirical calibration, guided by extensive comparisons with observation. In the following a summary addressing relevant examples is given.

The actual choice of radiative and collisional data turned out to be a critical factor for line-formation computations of non-LTE-sensitive transitions in C II, which is known to be problematic from the literature (e.g. Lambert 1993; Sigut 1996). A few comparisons of atomic data available from the literature and the influence of input atomic data on selected C II lines is provided. These transitions are highlighted in the Grotrian diagram of the C II model (Fig. 6.2), which will help to illustrate some of the channels leading to the marked non-LTE sensitivity. The Grotrian diagram also gives an overview of the levels involved in the formation of the observed transitions.

Photoionization cross-sections. The strength of a spectral line can be

strongly influenced by photoionizations which may impact the level populations decisively. On the other hand, photoionization rates depend implicitly on the level populations, $R_{ij} = R_{ij}(\alpha_{ij}, J_\nu[n])$, i.e. from the coupling of Eqns. 2.5 & 2.26.

The largest contribution to the integral in R_{ij} (Eqn. 2.27) comes from frequencies with large flux and large cross-section. The flux maximum in early B stars is located longward of the Lyman jump at 912 Å. Examples of the behaviour of photoionization cross-sections are given in Fig. 6.3.

The ionization of C II is essentially determined by the rates from the highly-populated ground state and the low-excitation levels. Their relative importance may be strengthened in cases where the ground state ionization potential coincides with that of a major opacity contributor, He I in the present case. Photoionizations from the ground state may then be less efficient because of the reduced stellar flux shortward of the ionization edge. Recombinations, on the other hand, are important for the population of high-excitation levels (preferentially at high ℓ, i.e. states with large statistical weight), which couple to the low-lying states via recombination cascades. For the case of C II this implies: i) an increased sensitivity of the C II/III ionization balance to the exact run of the photoionization cross-sections of levels at low excitation energies and ii) an increased sensitivity of transitions like C II $\lambda\lambda$6151, 6462 and in particular 4267 Å to non-LTE effects because of their participation in the recombination cascade.

A comparison of photoionization cross-sections from OP (Yan & Seaton 1987) and N02b for two levels (marked in the Grotrian diagram, Fig. 6.2) is given in Fig. 6.3. The first term, $2p^2\ ^2S$, is not directly involved in the formation of the C II $\lambda\lambda$ 4267, 6151 and 6462 Å transitions. However, it is populated considerably and therefore contributes to the C II/III ionization balance. Note the wavelength shifts in the resonance structures of both data. This results in different contributions of the region between the threshold and the Lyman edge to the integral in R_{ij} (Eqn. 2.27), which affect the photoionization rates considerably. On the other hand, the photoionization cross-sections for $4f\ ^2F^0$ agree well, except for the resonance structure at shortest wavelengths where the stellar flux becomes negligible. Consequently, both data (and many others for highly-excited levels) are exchangable without showing consequences for the spectrum synthesis computations. Note that experimental threshold wavelengths are adopted. On the other hand, for $2p^2\ ^2S$ and other levels at lower excitation energy there is a non-negligible effect on the $\lambda\lambda$4267 and 6151 Å transitions when exchanging both data, as can be seen in Fig. 6.4. In an extreme case, accounting for photoionization cross-sections from N02b for all levels results in a very strong C II $\lambda\lambda$4267 Å line. A reduction of the C abundance by up to $\sim$0.8 dex is required to fit the observed line profile in the calibration stars with such a model atom. Preference to the OP data over the cross-sections of N02b is given in the final model atom ('model of reference'), which help to reproduce observation over the entire parameter range consistently.

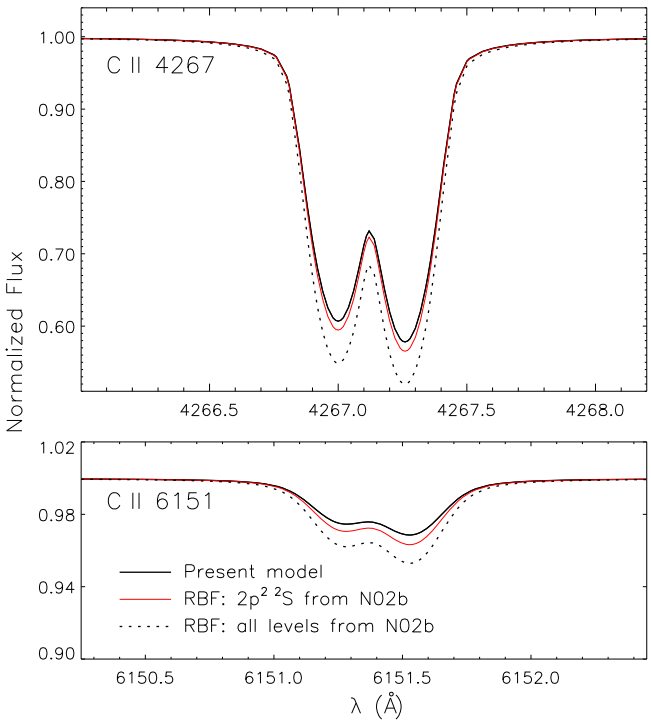

Figure 6.4: Sensitivity of line profiles of two C II transitions to variations of photoionization cross-sections. The calculations are made for three different model atoms using the same model atmosphere (as appropriate for HR 5285): the reference model atom, with cross-sections for $2p^2\ ^2S$ from N02b, and the reference model atom with all photoionization data replaced by values from N02b. The profiles are not convolved for effects of rotation or instrumental broadening.

Oscillator strengths. Comparisons between multiplet f-values from three sources of *ab-initio* computations are shown in Fig. 6.5: data based on I) FFT04, II) N02a and III) the Opacity Project (Yan et al. 1987). The primary source of f-values is FFT04, which should be most accurate. The preference for the OP over the N02a data is motivated by the good agreement of the former with FFT04 (with two exceptions), while oscillator strengths from N02a may show significant differences for several lines. Data from N02a is therefore adopted only in the cases where the other sources do not provide information.

Collisional ionization cross-sections. High-excitation levels of C II can couple collisionally to the C III continuum. The line-formation calculations for C II $\lambda\lambda$4267, 6151 and 6462 Å are also highly sensitive to the choice of collisional ionization cross-sections, as shown in Fig. 6.6. The approximation of Seaton (1962) is used to evaluate the collisional ionization rates because of a lack of any data from *ab-initio* computations. Threshold cross-sections for the 6f $^2F^o$ and 6g ^2G levels, that are involved directly in the formation of C II $\lambda\lambda$6151 and 6462 Å,

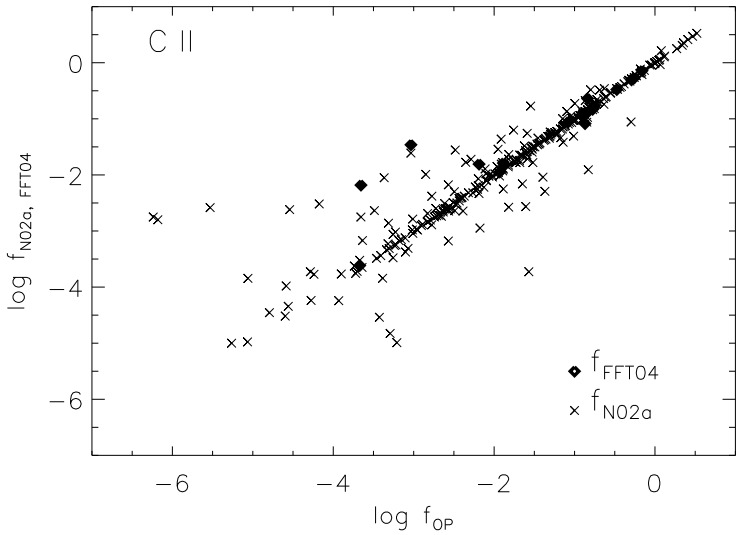

Figure 6.5: Comparison of oscillator strengths from Nahar (2002a: N02a) and Froese Fischer & Tachiev (2004: FFT04) vs. values from the Opacity Project (Yan et al. 1987: OP).

and indirectly of C II λ4267 Å (see Grotrian diagram, Fig. 6.2) are scaled with different factors, i.e. increasing the collisional rates (Eqn. 2.29). The effects on abundance analyses can also be drastic, as in the previous example. The empirical calibration indicates an increase of the OP data for these two levels by a factor 10 to be appropriate for reproducing observation over the entire parameter range in a consistent way.

Collisional excitation cross-sections. Cross-sections for excitation via electron collisions, which are proportional to the collision strength Ω_{ij}, can show complex behaviour with impact energy. In practice, the cross-sections will be weighted by a Maxwell distribution (see Eqn. 2.29), such that data from *ab-initio* calculations are often tabulated already in thermally-averaged form as effective collision strengths

$$\Upsilon_{ij} = \int_0^\infty \Omega_{ij} \exp(-E_j/kT)\, \mathrm{d}(E_j/kT)\,, \tag{6.1}$$

where E_j is the energy of the outgoing electron, k the Boltzmann constant and T the temperature.

Larger collision strengths facilitate a tighter collisional coupling and therefore promote the establishment of LTE. Consequently, the collisional data used in a model atom will have an influence on the predicted line profiles.

Accurate data from *ab-initio* calculations for larger sets of transitions have become available only recently. Effective collision strengths of Wilson et al. (2005, WBH05) are employed to construct the C II model. A later revision of part of the data (Wilson et al. 2007, WBH07) had negligible influence on the predicted line profiles of almost all observable transitions, except for C II $\lambda\lambda$ 3918/20 and

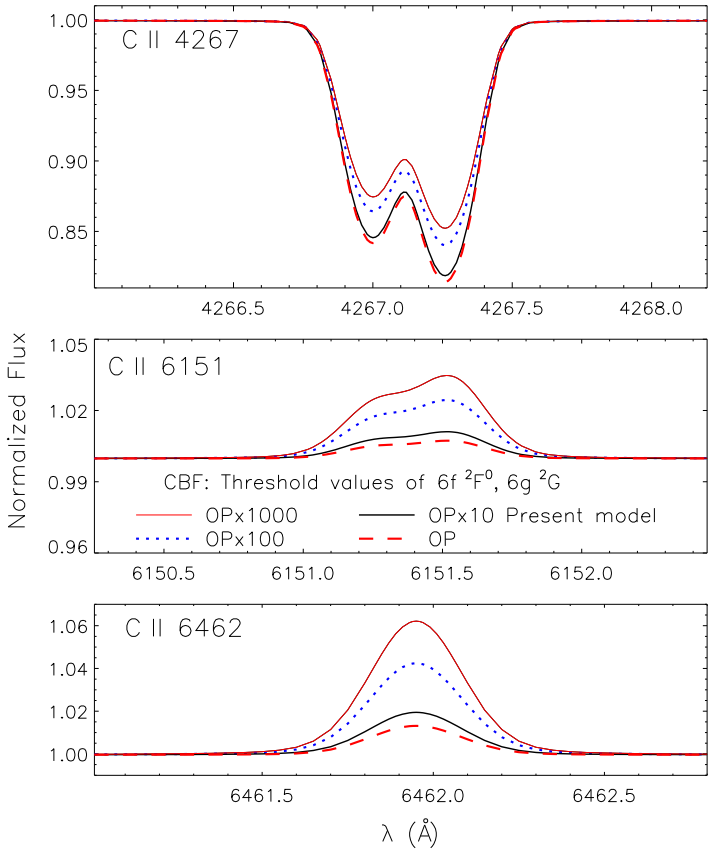

Figure 6.6: Reactions of three highly non-LTE-sensitive lines to changes of collisional ionization cross-sections. The modifications are made for two energy levels which are directly involved in the formation of C II $\lambda\lambda$6151 and 6462 Å and indirectly in C II λ4267Å. The calculations are made for different model atoms with specific values of the reaction cross-section at threshold and the same set of atmospheric parameters (as appropriate for τ Sco).

6578/82 Å, see Fig. 6.7 for an example. The good agreement of abundances derived from these four with other transitions was broken when using the improved WBH07 data, requiring abundance adjustments of up to ∼0.3 dex to match observation. The situation may be improved for the stars of the calibration sample by increasing the effective collision strength for the 3s ^{2}S–3p ^{2}P^o transition by an empirical factor of two, see Fig. 6.7. This is larger than the typical uncertainty of such *ab-initio* data, which amounts to an estimated 10-20%. However, a closer inspection of the energy-dependent collision strength for this transition shows that resonances dominate Ω in the region near threshold. The positions and strengths of the resonances are sensitive to the details of the atomic data calculations, in particular to the assumptions made for constructing the target. The near-threshold region in turn contributes most to the integral in Eqn. 6.1. Con-

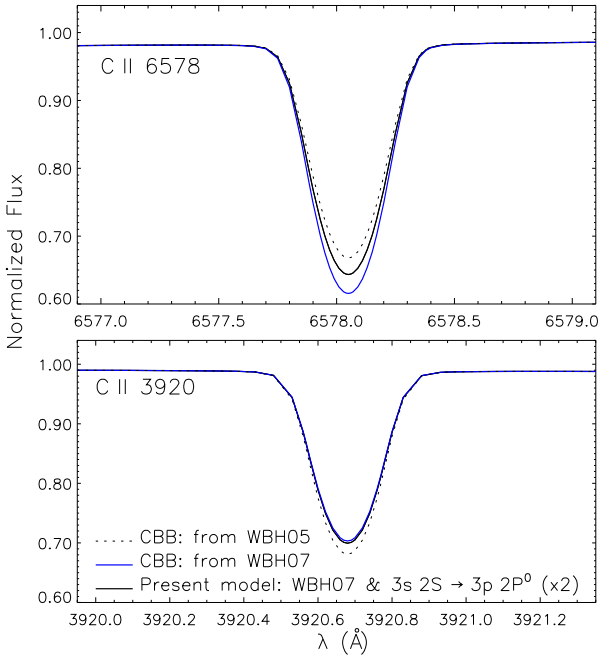

Figure 6.7: Effect of employing different effective collision strengths on the C II $\lambda\lambda$ 6578 and 3920 Å lines (for HR 1861). Only variations of the data from *ab-initio* calculations (Wilson et al. 2005, 2007) are considered.

sequently, more comprehensive *ab-initio* computations are required to investigate this in detail. However, these are beyond the scope of the present work.

Collisional data from *ab-inito* calculations are typically available only for transitions between relatively low-lying energy levels. In the case of C II the dataset is complete for levels up to principal quantum number $n = 4$. Therefore, for the bulk of the transitions approximation formulae have to be applied. However, trends and regularities from the *ab-inito* data may be used to improve on the standard approximations made for these, e.g. dropping the assumption of an energy-independent $\Omega = 1$ for the evaluation of the Allen (1973) formula (see Sect. 6.1).

In practice, simple approximations *are* used to describe collisional processes in most of the model atoms available for non-LTE calculations at present. One can ask what the effects on synthetic profiles will be from such a simplification. This is shown in Fig. 6.8 for selected lines in two of the programme stars. Notable corrections in abundance would be required to reproduce the results from the reference model, an increase in some of the lines but also a decrease in others. The overall good agreement with observation (Sect. 6.3) would be destroyed: the non-LTE sensitive lines and the lines 'in LTE', which are unaffected by such modifications, would indicate widely different abundances. Note that the effects vary from star to star.

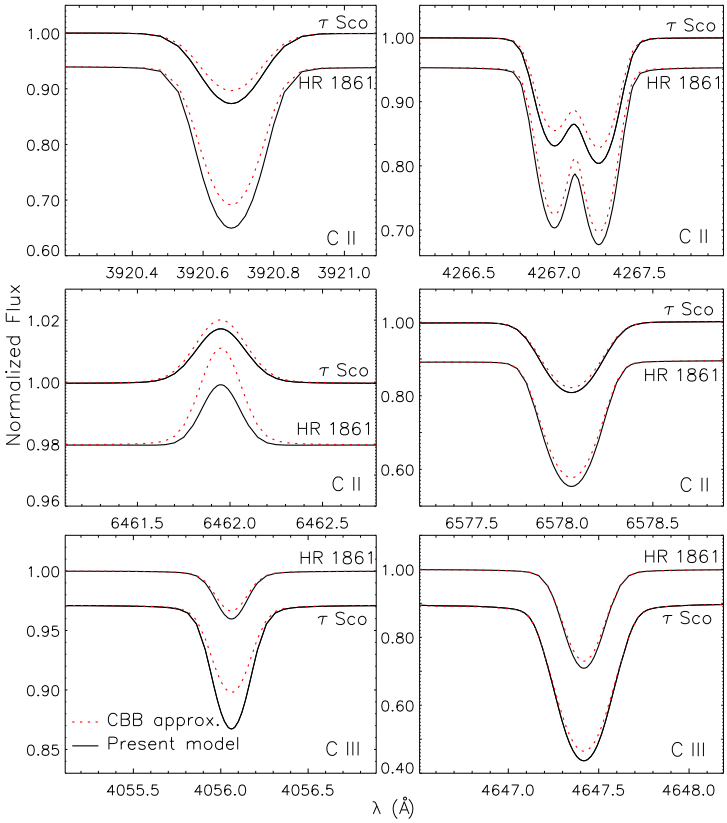

Figure 6.8: Comparison of synthetic C II/III line profiles for two of the sample stars using different model atoms. One calculation uses the reference model atom and the other adopts standard approximation formulae for evaluating collisional rates for all transitions.

The discussion on the impact of atomic data on line-formation calculations is concluded in Fig. 6.9. Here, the differences in abundance derived with the initial model atom (built from the supposedly 'best' available homogeneous set of atomic data, N02ab) and with the model of reference (after the empirical calibration) are quantified for the entire sample of stars. Abundances from the strong and non-LTE-sensitive C II $\lambda\lambda$4267 and 6578 Å transitions are compared to abundances derived from the weaker C II λ5145 Å line, which is almost insensitive to the details of the model atom (i.e. it is 'in LTE'). The relative abundance is displayed as a function of effective temperature for each star (see Section 6.3 for final results). Pronounced systematic trends exist when the initial model atom is used, correlating with the strength of the lines (i.e. stronger lines show a larger sensitivity to non-LTE effects and therefore to the input atomic data). These trends and abundance differences from C II $\lambda\lambda$4267 and 6578 Å almost vanish when the model of reference is used. The remaining small differences may be reduced even further when improved atomic data, in particular for collisions

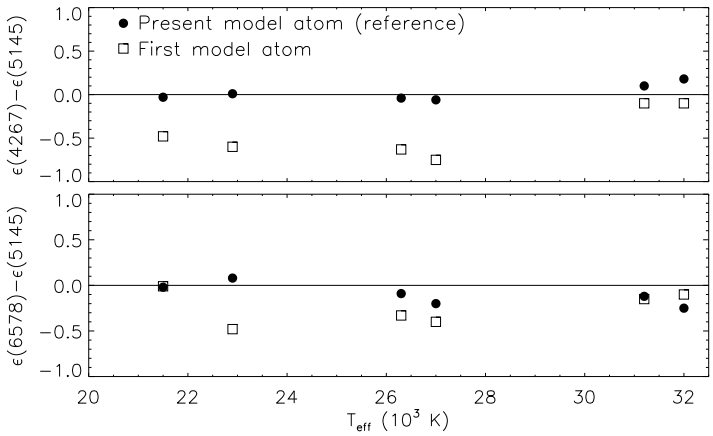

Figure 6.9: Abundance differences from the analysis of C II $\lambda\lambda$4267 and 6578 Å (highly sensitive to the input atomic data) and C II λ5145 Å ('in LTE'). Displayed are results for the six sample stars, as a function of effective temperature. A comparison of the initial model atom (all radiative transition data for C II from N02ab) and the final model atom after the empirical calibration is shown. See the text for details.

involving high-excitation levels, become available. Note, that the C II λ6582 Å line (not displayed here) shows a trend similar to that of λ6578 Å. The whole multiplet centered on C II λ5145 Å also behaves consistently. This kind of test has been made for all C II-IV lines for every set of input atomic data in the empirical calibration process of the model atom.

The comparison of observation with model spectra for C III and C IV, as computed with the initial model ions based on the most sophisticated input data available, reveals little need for improvement. Both ions are relatively simple, showing (earth)alkali electron configurations, which pose little challenge to *ab-initio* computations. Further empirical testing of the C IV model may be desirable, involving more transitions. However, this is beyond the scope of the present work, as markedly hotter plasma environments need to be considered, where the hybrid non-LTE approach may reach its limitations (see the discussion in Chapter 5).

This detailed study of non-LTE and LTE abundances in Sect. 6.3 helps to identify the 'lines in LTE' for the different atmospheric parameters under analysis. These may provide good starting points for further analyses when one desires to avoid non-LTE effects.

6.2.3 Line-Formation Details

A closer study of the underlying line-formation processes allows the nature of the non-LTE effects to be understood. This is facilitated by Fig. 6.10 for some representative transitions of C II/III/IV in the programme star τ Sco.

Departure coefficients $b_i = n_i^{\rm NLTE}/n_i^{\rm LTE}$ are displayed in the left panel of Fig. 6.10 for the levels involved in the transitions of interest and the ion ground

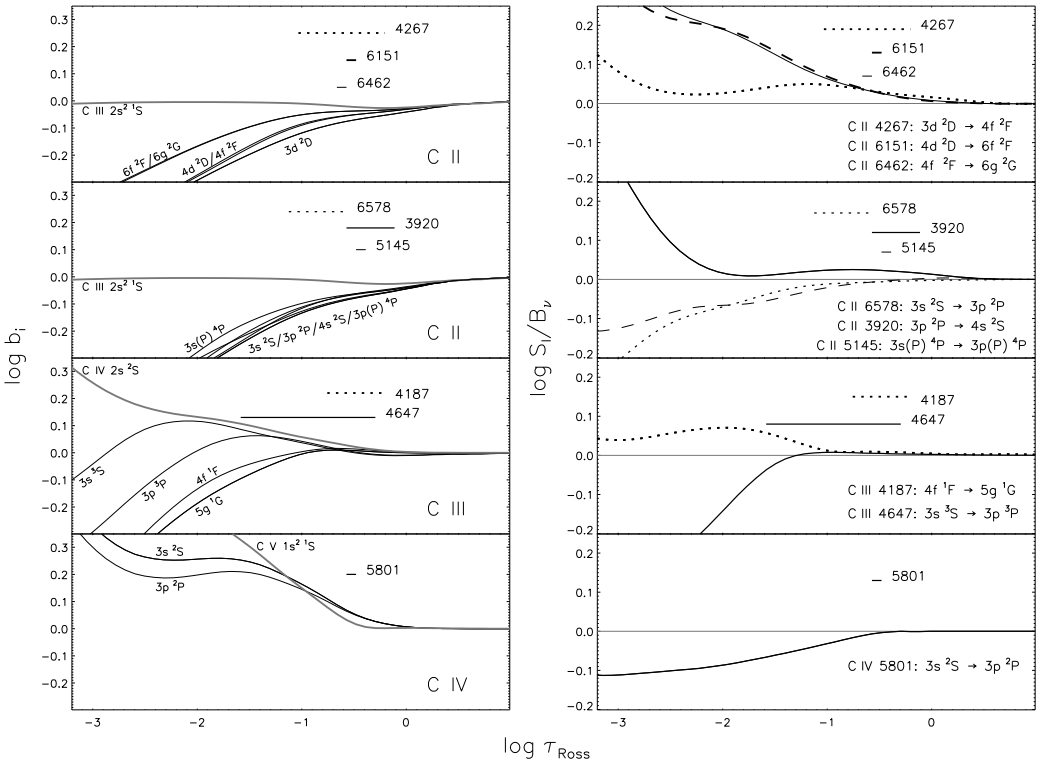

Figure 6.10: Departure coefficients b_i and ratio of line source-function S_l to Planck function B_ν at line centre as a function of τ_Ross for selected carbon lines in τ Sco. The spectral lines are encoded by the different line styles indicating the line-formation depths. Thin grey lines on the right-hand panel correspond to S_l=B_ν.

states. Values of $b_i > 1$ imply an overpopulation relative to detailed equilibrium and $b_i < 1$ an underpopulation. Non-LTE departures of the level occupations impact the line source function S_l. The ratio of S_l (Eqn. 2.43) to the Planck function B_ν is shown for selected transitions in the right panel of Fig. 6.10, and can be expressed as

$$\frac{S_\mathrm{l}}{B_\nu} = \frac{\exp\left(h\nu_{ij}/kT\right) - 1}{b_i/b_j \exp\left(h\nu_{ij}/kT\right) - 1} \ . \tag{6.2}$$

As can be seen from Eqn. 6.2, S_l/B_ν is determined by the ratio of the departure coefficients for the lower and upper levels (i, j). An overpopulation of the upper level relative to the lower (i.e. $S_\mathrm{l}/B_\nu > 1$) results in non-LTE weakening of the line and may lead to emission in cases of pronounced overpopulation, while the inverse gives non-LTE strengthening.

The level populations reach detailed equilibrium values deep in the atmosphere, where large collisional rates and small mean-free paths between photon absorptions (both because of the high densities of the plasma) enforce this inner boundary condition. Double-ionized carbon is the main ionization stage at

the temperatures of τ Sco - the C III ground state is close to LTE. Single-ionized carbon is overionized at line-formation depths, therefore the levels are underpopulated relative to LTE, and C IV and the C V ground state are overpopulated.

In general, level populations in C II depart most from detailed equilibrium in the low-excitation states and approach LTE values gradually with increasing excitation energy, as collisions facilitate coupling with the C III ground state. Therefore, most of the non-LTE-sensitive transitions in C II have upper levels that are overpopulated relative to the lower level, so that the lines experience slight (λ 3920 Å) to notable weakening (λ 4267 Å) relative to LTE and may even turn into emission ($\lambda\lambda$ 6151, 6462 Å). The $\lambda\lambda$ 6578/82 Å doublet experiences non-LTE strengthening for lower effective temperatures, while in hotter objects like τ Sco the lines are found to be close to LTE. The other observable C II lines arise in the quartet spin system. They are weaker (C II λ 5145 Å is the strongest), i.e. they are formed deeper in the atmosphere, and their formation involves high-excitation levels which are coupled collisionally at these depths, such that these lines are essentially in LTE. Note that the behaviour of $S_{\rm l}/B_\nu$ for λ 4267 Å is in good agreement with the findings of Sigut (1996). On the other hand, notable differences exist for the $\lambda\lambda$ 6578/82 Å doublet in particular at higher $T_{\rm eff}$. The reasons for this will be discussed in the next section (but see also Fig. 6.15).

The C III transitions can also experience both, non-LTE weakening (like the strong λ 4187 Å) and non-LTE strengthening (like the strong triplet 4647-4651 Å). The C IV doublet $\lambda\lambda$ 5801/12, which becomes observable only in the hottest stars, shows a pronounced non-LTE strengthening.

6.2.4 Sensitivity of ϵ(C) to Parameter Variations

Spectral lines of carbon, like many other metal lines, can react sensitively to variations of the stellar atmospheric parameters. This property is a powerful tool for the atmospheric parameter and abundance determination, using the iteration scheme (Fig. 6.1). This is a non-trivial and crucial step in the analysis, which must be performed carefully in order to avoid systematic error. The consequences of systematically biased atmospheric parameters on carbon line profiles and the derived abundances are investigated in the following.

The offsets for the parameters (effective temperature $\Delta T_{\rm eff}$=−2000 K, surface gravity $\Delta \log g$= +0.2 dex and microturbulent velocity $\Delta \xi$= +5 km s^{-1}) are representative for systematic discrepancies between the final values and those from previous studies (and also in between these studies). Note that they are much larger than the statistical uncertainties derived in this work. Such discrepancies may be caused by several factors, among others: I) photometric effective temperature calibrations based on model atmospheres with insufficient line blanketing[3], II) spectroscopic ionization equilibria based on predictions of incomplete

[3]An important but underestimated source of systematic error are abundance 'standards'.

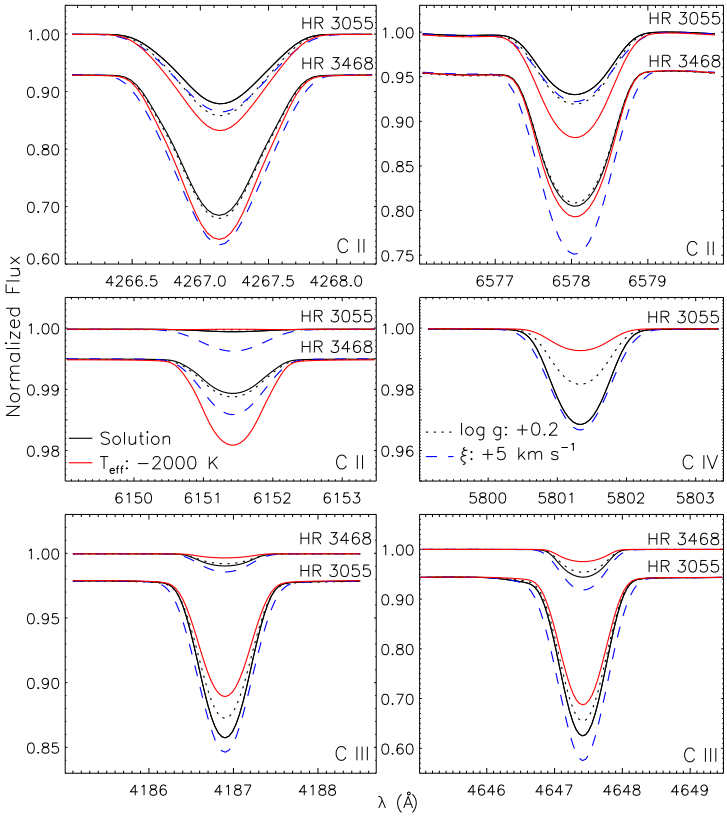

Figure 6.11: Sensitivity of selected C II/III/IV lines to atmospheric parameter variations in two giants: HR 3055 (hotter, B0 III) and HR 3468 (cooler, B1.5 III). The present solution corresponds to the final parameters from Table 5.1 and a constant value of ϵ(C) for all lines. The parameter offsets are typical for statistical and systematic uncertainties from published values. The theoretical spectra are convolved with a rotational profile for $v \sin i = 20$ km s^{-1}. The present solution establishes the ionization equilibrium. HR 3468 is too cool to show C IV lines.

model atoms, iii) the assumption of LTE for the computation of Balmer line profiles, which may cause a systematic overestimate of $\log g$ by up to 0.2 dex (Chapter 5).

Figure 6.11 shows the sensitivity of selected C II/III/IV lines in two giants of

E.g., the widely used classical Kurucz (1993a) ODFs were computed on the basis of (scaled) solar abundances according to Anders & Grevesse (1989), which indicated a high abundance for the most important line opacity source, iron ($\log \mathrm{Fe/H} + 12 = 7.67$). A later revision (Grevesse & Sauval 1998) lead to employ ODFs with appropriately reduced metallicity for the present model atmosphere calculations (see Chapter 5 for a discussion). This changes the atmospheric temperature structure notably via a reduced backwarming effect, giving lower temperatures in the line-formation region by up to ∼500 K, i.e. slightly higher than the uncertainties in $T_{\rm eff}$ derived in this work.

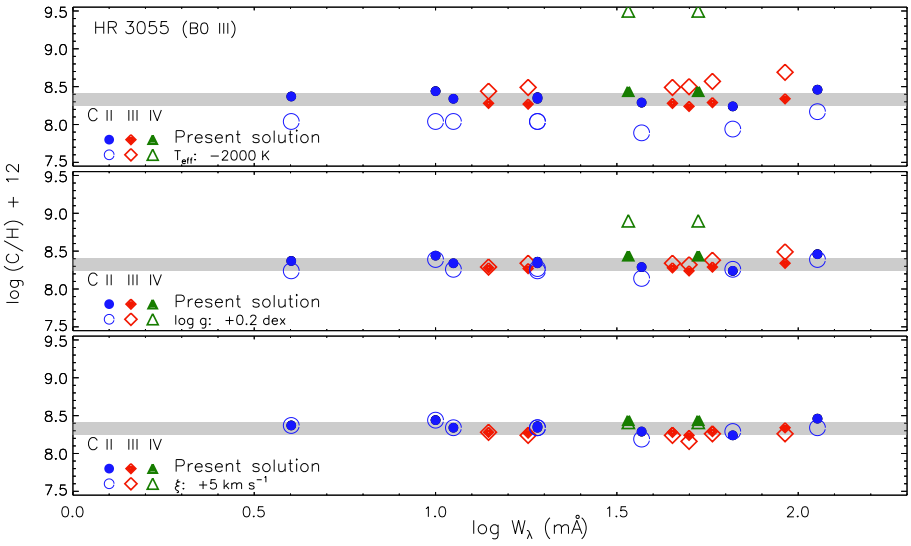

Figure 6.12: Sensitivity of carbon abundances to stellar parameter variations: $T_{\rm eff}$ (upper panel), log g (mid panel) and microturbulent velocity (lower panel). The offsets of the parameters are displayed in the lower left part of each panel. Note the resulting large spread in abundance from individual lines of the three ionization stages, in particular for variations of $T_{\rm eff}$ (upper panel). Note also the implications of using only few lines of one ionization stage for abundance determinations in the presence of systematic errors in the atmospheric parameters. The grey bands correspond to 1σ-uncertainties of the stellar carbon abundance in the final solution (summarised in Table 6.2).

the sample (HR 3055 and HR 3468) to variations of basic atmospheric parameters like $T_{\rm eff}$, log g and ξ. The profiles accounting for these variations are compared with those computed with the final atmospheric parameters and an averaged carbon abundance. The sensitivity to parameter variations differs from line to line. For the hotter star, the C IV and – when strong enough – the C II $\lambda\lambda$ 6151 and 6462 Å lines (the latter not displayed in Figure 6.11) are ideal indicators for both $T_{\rm eff}$ and log g, while the rest of the lines is mostly sensitive to changes in $T_{\rm eff}$ and the strong C III lines also to changes in ξ. The C II $\lambda\lambda$ 6151 and 6462 Å lines are too weak to be measured in this case; however, one can still distinguish between emission and absorption (in τ Sco they are strong enough to be used in the analysis). For the cooler star, the C II $\lambda\lambda$ 4267, 6151 and 6462 Å lines are highly sensitive to variations of $T_{\rm eff}$ and ξ, the rest of the lines are mostly sensitive to $T_{\rm eff}$ and the strong C II lines also to ξ.

The response to variations in log g can be amplified for C II $\lambda\lambda$ 6578/82 Å at higher gravities, because they are formed on the red wing of Hα. The local continuum and therefore the line-formation depths may change as a consequence, impacting the non-LTE effects. A correct treatment of the hydrogen Balmer

Table 6.1: Systematic uncertainties in carbon abundances (in dex, relative to the final results, Table 6.3) caused by atmospheric parameter variations and the assumption of LTE for the line-formation calculations.

	HR 3055	$\Delta T_{\rm eff}$	$\Delta \log g$	$\Delta \xi$	LTE
		-2000 K	$+0.2$ dex	$+5$ km s^{-1}	
C II	4267.2	-0.33	-0.11	-0.16	-0.40
	5133.3	-0.30	-0.10	0.00	0.00
	5143.4	-0.40	-0.05	0.00	0.00
	5145.2	-0.32	-0.09	-0.02	0.00
	5151.1	-0.30	-0.08	0.00	0.00
	5662.5	-0.33	-0.13	0.00	0.00
	6578.0	-0.40	-0.15	-0.10	-0.01
	6582.9	-0.30	$+0.02$	$+0.05$	$+0.03$
C III	4056.1	$+0.21$	$+0.06$	-0.04	$+0.08$
	4162.9	$+0.28$	$+0.09$	-0.03	$+0.25$
	4186.9	$+0.35$	$+0.15$	-0.08	$+0.07$
	4663.5	$+0.22$	$+0.07$	-0.03	$+0.22$
	4665.9	$+0.26$	$+0.08$	-0.08	$+0.35$
	5272.5	$+0.16$	$+0.01$	0.00	0.00
C IV	5801.3	$+1.06$	$+0.46$	-0.03	$+0.39$
	5811.9	$+1.06$	$+0.46$	-0.03	$+0.39$

line-opacity therefore plays an important rôle in this context. Non-LTE effects strengthen the Balmer line wings in particular at higher temperatures (Chapter 5). This might be one of the reasons why Sigut (1996) found problems in reproducing observed trends for the C II $\lambda\lambda$ 6578/82 Å doublet at $T_{\rm eff} > 25\,000$ K: Hα was assumed to be formed in LTE in that work.

For HR 3055 the systematic effects exemplified in Fig. 6.11 are quantified (note that C III λ4647 Å is blended and C II λ6151 Å is too weak in this case) by deriving non-LTE carbon abundances for the modified values of $T_{\rm eff}$, $\log g$ and ξ and comparing them to the final solution for individual lines. This is summarised in Table 6.1 and visualised in Fig. 6.12. Table 6.1 also shows systematic offsets that arise from the assumption of LTE for the line-formation calculations. This comparison helps to identify the relative importance of atmospheric parameters/non-LTE effects for some key spectral lines. Note that the C IV lines are extremely sensitive to changes in $T_{\rm eff}$ and $\log g$ at this temperature (31 200 K), with discrepancies amounting to up to $\sim$+1.0 dex in abundance for $\Delta T_{\rm eff} = -2000$ K[4]. The C II/III ionization balance is also never established for a

[4]Even larger offsets in $T_{\rm eff}$ are found with respect to the literature, up to $\Delta T_{\rm eff} \simeq -4000$ K,

Table 6.2: Carbon abundances of the programme stars.

	τ Sco Sco Cen	HR 3055 Field	HR 1861 Ori OB1	HR 2928 Field	HR 5285 Sco Cen	HR 3468 Field
ϵ(C) (dex)	8.30 ± 0.12	8.33 ± 0.08	8.33 ± 0.08	8.27 ± 0.07	8.29 ± 0.05	8.37 ± 0.10
# C lines	32	19	30	22	22	19

variation of these parameters (abundance changes down to -0.40 dex for C II and up to $+0.35$ dex for C III when compared to the present solution). An expected reduction of the abundances from strong lines is obtained for an increased microturbulence. Note that the systematic variations of carbon abundance with ξ for some lines are significant considering the high accuracy we are aiming at, despite smaller effects in general than for $T_{\rm eff}$ and $\log g$ variations.

The solutions for the modified atmospheric parameters are characterised by a large scatter of carbon abundances from individual lines (an increase of the statistical 1-σ uncertainties by up to $\sim$0.4 dex), despite similar average values. These similar averages are however accidental. Note that variations of $T_{\rm eff}$ show by far the largest effects.

The use of only a few spectral lines from one ionization stage for carbon abundance determinations – which is common practice in the literature – may have serious implications on the accuracy of the results. Possible systematic discrepancies, as indicated here, may remain unrecognised. Moreover, the opportunity to improve on the atmospheric parameter determination by establishing the highly parameter-sensitive ionization balance may be missed in such cases. This high sensitivity of the carbon lines to atmospheric parameter variations can be used as an important tool for precise quantitative spectral analyses of this kind of star when applying the calibrated model atom in the future.

Some lines are practically unaffected by non-LTE effects, as indicated by Table 6.1 (see also Sect. 6.2.2). This implies that they are almost insensitive to any reasonable choice of model atom. On the other hand, they are highly sensitive to the choice of atmospheric parameters. This property is highly useful for the model atom calibration because it helps to disentangle effects due to non-LTE from those due to inaccuracies in the stellar parameters, facilitating a reduction of systematic errors. A central conclusion is that typical systematic uncertainties in the atmospheric parameters can have a similar or even higher impact on the carbon abundance determination than a neglect of non-LTE effects.

see Sects.4.1 and 6.4.

6.3 Results

Accurate atmospheric parameters and carbon abundances are derived from line-profile fitting by χ^2 minimisation, which puts tighter constraints than matching only equivalent widths. The parameters are summarised in Table 5.1 and the abundances in Table 6.2 for the six programme stars (as obtained from the iterative process, Fig. 6.1). The uncertainties of $T_{\rm eff}$ and log g are estimated from the extremely sensitive carbon ionization equilibrium. They are lower for hotter stars because of the additional restrictions imposed by the presence of lines from three ionization stages. For velocities, the 1σ-uncertainties from the analysis of the entire line ensemble are provided. Projected rotational velocity and (radial-tangential) macroturbulence (Gray 1992, p. 407ff.) were simultaneously derived allowing for small line-to-line variations in order to obtain an optimum fit (see Ryans et al. 2002 for the case of B supergiants).

It is important to emphasise that the final set of atmospheric parameters as derived from the C II/III/IV ionization balance is in agreement with those from previous quantitative analyses of these stars in Chapter 5. In particular, a simultaneous match is achieved for I) the H and He lines in the visual and (where available) in the near-IR, including the He I/II ionization equilibrium in the hotter stars and II) the spectral energy distributions from the UV to the near IR. A similar degree of consistency is typically not obtained in comparable studies of early-type stars.

A large quantity of carbon lines is analysed for the first time, giving consistent abundances for all of them. The excellent quality of the observed spectra combined with the present improved analysis technique allow such precise results. The 1σ-uncertainties from the line-to-line scatter are typically of the order 0.05–0.10 dex. The systematic uncertainties due to remaining errors in atmospheric parameters and atomic data are estimated to be of the order 0.10–0.15 dex, taking Table 6.1 and the present experiences from Sect. 6.2.2 as a guidline.

Details on the analysis of individual lines can be found in Table 6.3. This summarises line identifications, level designations, $\log gf$ values, excitation potential of the lower level χ_l, and for each star equivalent widths W_λ and the derived non-LTE and LTE abundances. Note that as many lines as possible are analysed per star, excluding only features with strong blends by other chemical species. This helps to follow the behaviour of each line and the quality of the modelling at different temperatures and gravities (see the previous section). Transitions involving autoionizing states are not accounted for explicitly in the spectrum synthesis (however, they are considered via resonances in the photoionization cross-sections). These are lines like C II $\lambda\lambda$ 4075 (a blend with O II), 4318 (a blend with S II), 4374.3, 4375.1, 4376.6, 4411.2/5 and 4627.4 Å, which have sometimes been used for abundance determinations in previous studies.

Table 6.3: Carbon abundance analysis for the programme stars. bl: blend with other line;... : too weak or absent;XX: LTE does not reproduce the emission.

					τ Sco			HR 3055			HR 1861			HR 2928			HR 5285			HR 3468		
Ion	λ(Å)	l − u	log gf	χ_l (eV)	W_λ	NLTE	LTE	W_λ	NLTE	LTE	W_λ	NLTE	LTE	W_λ	NLTE	LTE	W_λ	NLTE	LTE	W_λ	NLTE	LTE
C II	3919.0	$3p\,^2P$ – $4s\,^2S$	−0.53	16.33		bl			bl			bl			bl		90	8.21	8.04		bl	
	3920.6	”	−0.23	16.33	29	8.23	7.98	35	8.40	8.15	68	8.30	8.04	69	8.30	8.09	97	8.21	8.04	123	8.34	8.34
	4267.0/2	$3d\,^2D$ – $4f\,^2F^0$	0.56/0.74	18.04	102	8.45	7.88	113	8.46	8.06	135	8.34	7.64	161	8.25	7.59	220	8.26	7.98	230	8.33	7.92
	5133.0/3	$(^3P^0)3s\,^4P^0$ – $(^3P^0)3p\,^4P$	−0.21/−0.18	20.70	19	8.29	8.28	19	8.34	8.34	52	8.41	8.41	42	8.27	8.27	52	8.30	8.30	71	8.35	8.33
	5137.3	”	−0.91	20.70		...			...		9	8.46	8.44	6	8.39	8.29	12	8.44	8.44		...	
	5139.2	”	−0.71	20.70	5	8.38	8.34		...		14	8.46	8.42	10	8.39	8.27	13	8.34	8.34	15	8.34	8.34
	5143.4	”	−0.22	20.70	11	8.33	8.31	10	8.44	8.44	27	8.39	8.39	26	8.33	8.30	28	8.34	8.34	35	8.36	8.33
	5145.2	”	0.19	20.71	22	8.27	8.29	19	8.36	8.36	50	8.40	8.40	39	8.29	8.28	43	8.29	8.24	62	8.32	8.31
	5151.1	”	−0.18	20.71	14	8.33	8.33	11	8.34	8.34	32	8.36	8.44	22	8.32	8.32	27	8.29	8.30	40	8.36	8.32
	5648.1	$(^3P^0)3s\,^4P^0$ – $(^3P^0)3p\,^4S$	−0.42	20.70	6	8.27	8.27		...		18	8.44	8.41	11	8.39	8.37	19	8.34	8.38	28	8.34	8.34
	5662.5	”	−0.25	20.71	7	8.27	8.27	4	8.37	8.37	19	8.38	8.36	16	8.34	8.29	21	8.34	8.36	31	8.34	8.29
	6578.0	$3s\,^2S$ – $3p\,^2P^0$	−0.03	14.45	50	8.02	8.01	66	8.24	8.24	138	8.20	8.51	115	8.20	8.37	150	8.27	8.77	230	8.40	8.84
	6582.9	”	−0.33	14.45	31	7.94	7.97	37	8.29	8.34	108	8.20	8.34	94	8.20	8.25	125	8.28	8.56	165	8.40	8.74
	6779.9	$(^3P^0)3s\,^4P^0$ – $(^3P^0)3p\,^4D$	0.02	20.70		...			...		19	8.19	8.26	36	8.12	8.14	33	8.24	8.26	60	8.21	8.24
	6780.6	”	−0.38	20.70		...			...		11	8.19	8.26		bl			bl			bl	
	6783.1	”	0.30	20.71		...		12	8.22	8.14	41	8.24	8.37	5	8.19	8.31	36	8.24	8.33	65	8.24	8.39
	6787.2	”	−0.38	20.70		...			...		11	8.24	8.34	11	8.19	8.29	12	8.29	8.36	30	8.34	8.39
	6791.5	”	−0.27	20.70		...			...		13	8.24	8.31	18	8.19	8.29	20	8.29	8.34	20	8.26	8.29
	6800.7	”	−0.34	20.71		...			...		10	8.27	8.36	12	8.34	8.36	10	8.24	8.26		...	
	6151.3/5	$4d\,^2D$ – $6f\,^2F^0$	−0.15/0.02	20.84	−8	8.29	XX		...			...			...		22	8.34	7.89	18	8.60	7.84
	6461.9	$4f\,^2F^0$ – $6g\,^2G$	0.42	20.95	−18	8.39	XX		...		−9	8.34	XX		...		28	8.29	7.81	14	8.60	7.84
C III	4056.1	$4d\,^1D^0$ – $5f\,^1F$	0.27	40.20	33	8.44	8.44	45	8.28	8.36	10	8.36	8.36	6	8.27	8.19		...			...	
	4152.5	$(^3P^0)3p\,^3D$ – $5f\,^3F^0$	−0.11	40.06	28	8.37	8.54		bl		7	8.37	8.37		...			...			...	
	4162.9	”	−0.84	40.06	46	8.33	8.57	58	8.29	8.54		bl			bl			...			...	
	4186.9	$4f\,^1F$ – $5g\,^1G$	0.92	40.01	67	8.57	8.41	92	8.34	8.41	20	8.32	8.24	15	8.24	8.20		...		14	8.49	8.45
	4515.8	$4p\,^3P$ – $5s\,^3S$	−0.28	39.40	18	8.21	8.24		bl		4	8.40	8.40		...			...			...	
	4516.8	”	−0.06	39.40	19	8.23	8.25		bl		6	8.37	8.33		...			...			...	
	4647.4	$3s\,^3S$ – $3p\,^3P$	0.07	29.53	188	8.30	≥9.0		bl		89	8.29	8.64	68	8.26	8.54	9	8.26	8.25	54	8.44	8.84
	4650.2	”	−0.15	29.53	153	8.34	≥9.0		bl		66	8.33	8.59	54	8.28	8.59	9	8.34	8.34		bl	
	4651.5	”	−0.63	29.53	113	8.44	9.00		bl		43	8.39	8.54	35	8.28	8.54		bl			bl	
	4663.5	$(^3P^0)3s\,^3P^0$ – $(^3P^0)3p\,^3P$	−0.61	38.22	13	8.17	8.44	18	8.27	8.49	5	8.37	8.40		...			...			...	
	4665.9	”	−0.03	38.22	37	8.16	8.60	50	8.24	8.59	13	8.38	8.62		...			...			...	
	5253.6	$(^3P^0)3s\,^3P^0$ – $(^3P^0)3p\,^3S$	−0.71	38.22	9	8.29	8.39		...			...			...			...			...	
	5272.5	”	−0.49	38.23	19	8.32	8.42	14	8.28	8.28		...			...			...			...	
	5695.9	$3p\,^1P$ – $3d\,^1D$	0.02	32.10	82	8.22	8.29		bl		10	8.34	8.34		bl			...			...	
	6731.0	$(^3P^0)3s\,^3P^0$ – $(^3P^0)3p\,^3D$	−0.29	38.22	11	8.37	8.18		...			...			...			...			...	
	6744.3	”	−0.02	38.23	11	8.33	8.09		...			...			...			...			...	
	8500.3	$3s\,^1S$ – $3p\,^1P$	−0.48	30.64	84	8.21	8.59	145	8.40	8.65		bl			bl			...			...	
C IV	5801.3	$3s^2S$ – $3s^2P^0$	−0.19	37.55	13	8.34	8.59	53	8.45	8.84		...			...			...			...	
	5811.9	$3s^2S$ – $3s^2P^0$	−0.49	37.55	12	8.34	8.59	34	8.45	8.84		...			...			...			...	

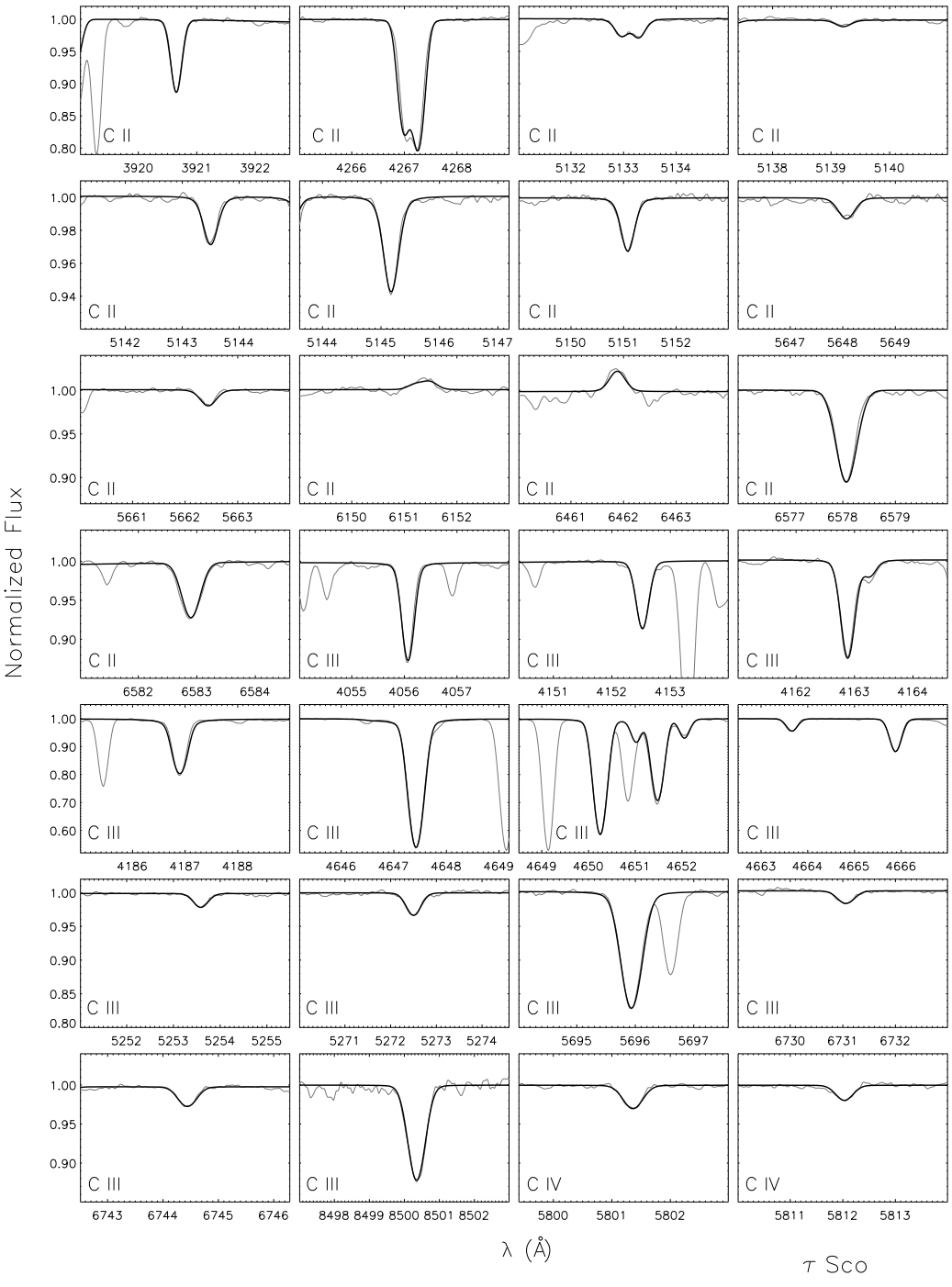

Figure 6.13: Examples of line profile fits (black line) to the observed high-quality spectrum (grey line) of τ Sco.

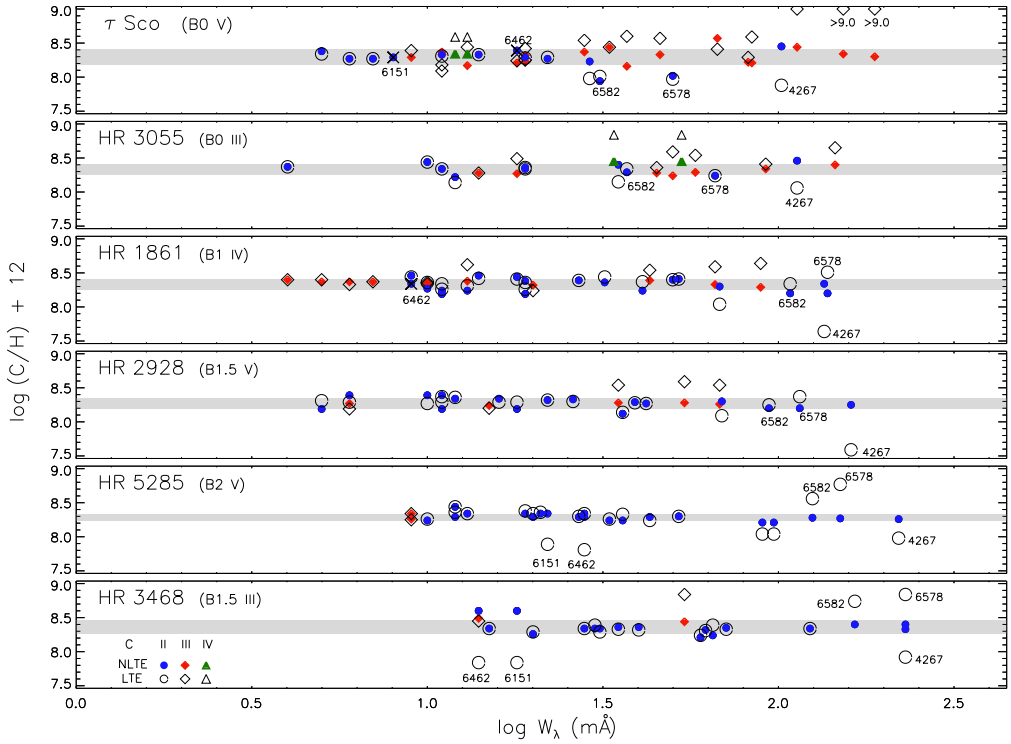

Figure 6.14: Non-LTE and LTE abundances derived from line profile fits to individual C II-IV lines in the programme stars as a function of equivalent width. The ID of the stars and the spectral classification is given in the upper left corner of each panel. The grey rectangles correspond to 1σ-uncertainties of the stellar carbon abundance from the line-to-line scatter. Identification of lines with high sensitivity to non-LTE effects is displayed. Emission lines are marked by crosses (C II $\lambda\lambda$6151 and 6462 Å in τ Sco and λ6462 Å in HR 1861): LTE calculations are not able to reproduce them even qualitatively.

The high quality of the line fits to the observed spectrum of τ Sco is demonstrated in Fig. 6.13, for almost all the analysed transitions. Similar information for the other programme stars can be found in Figs. D.1–D.5 in Appendix D. Of central importance is that the abundances derived from the individual lines show a small scatter in each sample star. Good fits to individual lines can almost always be obtained, however this does not imply consistency in the entire analysis. An example are the abundances from Fig. 6.12, which were also derived from high-quality line fits, but which show inconsistencies, expressed as a large line-to-line scatter, nonetheless. Another example from many other studies are discrepant lines that are excluded from the analysis in order to reduce the statistical uncertainties. The present work improves on this because the underlying physics is solved in a more consistent way.

A single exception to the overall good line fits is found: the doublet C II $\lambda\lambda$4267.0/2 Å in τ Sco, where the fine-structure components are resolved (Fig. 6.13). The synthetic profile is slightly broader than the observed one, even when neglecting micro- and macroturbulent broadening. Such a detail cannot be observed in the other stars because of their higher $v \sin i$.

The data from Table 6.3 are visualised in Fig. 6.14, where abundances are shown as a function of W_λ. Excellent consistency is found in the case of the non-LTE analysis while the quality of the results is considerably degraded in LTE. Note that the sub-set of the strong lines provides non-LTE abundances that are in good agreement with those derived from the entire sample of lines. This proves that the reference carbon model is suited well for analyses of low-S/N spectra and fast-rotating stars, where only the strongest lines are measurable and where such a consistency check is not feasible. Note also that the non-LTE effects differ from line to line and also from star to star.

One case requires further discussion: the C II $\lambda\lambda$ 6578/82 Å doublet in τ Sco. The remaining problems may be an artifact from the data reduction. The location of the red wing of Hα coincides with a bad column of the CCD of FEROS (the spectral orders are oriented along columns in this spectrograph). A perfect correction for this cannot be provided. Different wavelengths are affected, depending on the radial velocity shifts of the object. Note that the region around C II $\lambda\lambda$ 6578/82 Å doublet has been normalised relative to the local continuum in Fig. 6.13.

6.4 Comparison with Previous Work

The main sources of systematic uncertainties that can bias abundance analyses, as identified in Sects. 6.2.2 & 6.2.4: atomic data, i.e. different model atoms, and stellar parameters, i.e. in particular effective temperature scales are discussed in this section. A more comprehensive comparison is too complex to be performed because of the large number of variables involved, which in some cases are not even documented. This includes numerous factors related to observation (e.g. quality of the analysed spectra, continuum rectification, equivalent width measurements, line blends), model atmospheres (e.g. codes, abundance standards/linelists considered for line blanketing) and line-formation calculations (e.g. treatment of line blocking, oscillator strengths, line broadening). A comparison of the present results on carbon abundances in the solar neighbourhood with previous studies will be made in an extra section, because of the wider implications.

6.4.1 Predictions from Different non-LTE Model Atoms

Non-LTE line profiles based on the model atom of reference and the Eber & Butler (1988, EB) model have been computed and compared with Sigut's (1996)

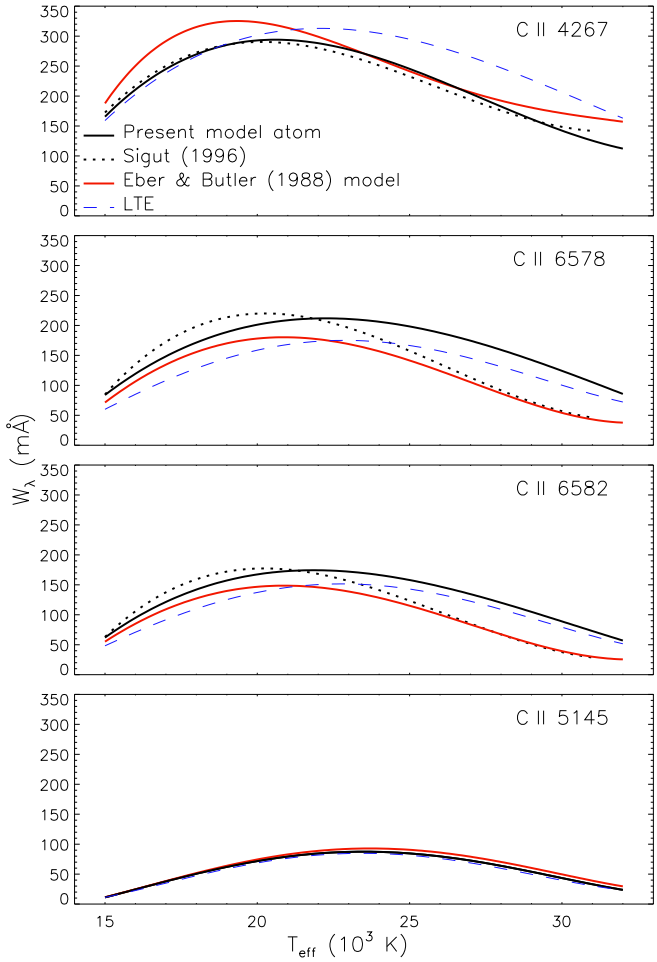

Figure 6.15: Predicted equivalent widths of some C II lines from different approaches as a function of $T_{\rm eff}$. All calculations were performed for $\log g = 4.0$, $\xi = 5\,{\rm km\,s^{-1}}$ and $\epsilon({\rm C}) = 8.55$, in order to facilitate a comparison with Sigut (1996).

non-LTE data and LTE results in Fig. 6.15. All models are calculated for the same set of atmospheric parameters and carbon abundances. Note that only one fundamental difference exists: the present computations account for non-LTE populations for hydrogen while Sigut assumes LTE. The consequences of this have been discussed in Sect. 6.2.4.

The model of EB is widely applied in the literature for non-LTE abundance determinations in OB stars. On the other hand, Sigut's alternative model improves somewhat on reproducing the observed behaviour of C II $\lambda\lambda$ 4267 and 6578/82 Å in OB stars. For this reason it constituted the starting point for other C II model atoms, by Korotin et al. (1999), by Przybilla et al. (2001) and the present work.

Consistent abundances from the application of the model atom of reference to observations are obtained for the C II λ 4267 Å transition, as shown in Sect. 6.3.

Consequently, the good agreement with Sigut's predictions indicates that his model atom is also highly useful for abundance determinations from this line. Note that Sigut compares his results (for $\epsilon(\mathrm{C}) = 8.55$) only qualitatively with observed equivalent widths from different sources, using stellar parameters derived in one of that studies, or from a photometric $T_{\rm eff}$-calibration. A reduction of carbon abundance and an improved determination of atmospheric parameters like proposed in the present work may bring observation in much better agreement with his predictions (his Fig. 1). In the region $\sim 22\,000\,\mathrm{K} \leq T_{\rm eff} \leq 28\,000\,\mathrm{K}$ good agreement is also found with the predictions of the EB model atom. However, this model provides too large equivalent widths and therefore lower abundances outside this region.

The analysis provided in the present work gives abundances from the $\lambda\lambda\,6578/82\,\text{Å}$ doublet consistent with that from other lines (τ Sco may be an exception, as discussed above). The trends predicted with the model atom of reference differ from the three other model calculations. The two other non-LTE predictions agree qualitatively up to $T_{\rm eff} \sim 22\,000\,\mathrm{K}$, Sigut's model indicating larger and EB smaller equivalent widths, respectively. However, the present model shows non-LTE strengthening throughout, approaching LTE at the high $T_{\rm eff}$-limit, while the two other models imply pronounced non-LTE weakening at $T_{\rm eff} \gtrsim 25\,000\,\mathrm{K}$. Note that this doublet experiences significant non-LTE effects only when the lines are strong, e.g. for high values of carbon abundance like those discussed in Fig. 6.15. The non-LTE effects are abundance-dependent, they get reduced with decreasing abundance.

Finally, the predicted equivalent widths for the widely used C II multiplet including $\lambda 5145\,\text{Å}$ are practically independent of the model assumptions. The lines are close to LTE. Any inconsistencies of carbon abundances based on this multiplet may be related to other effects, but not by the choice of the model atom. This multiplet, originated in the quartet spin system, was not analysed by Sigut.

6.4.2 Effective Temperatures

Abundance determinations can be systematically biased even in the case where a realistic non-LTE model atom is available. The atmospheric parameters need to be derived accurately as well. The effects of inappropriately chosen atmospheric parameters have been quantified in Sect. 6.2.4. Largely discrepant abundances are found from different ionization stages in particular for inaccurate effective temperatures. This difficulty had to be faced at the beginning of the present work, when effective temperatures derived from common photometric calibrations were adopted. It was not possible to establish the ionization equilibrium of C II/III even for the 'lines in LTE' in that case. In order to constrain all variables that are involved in the analysis simultaneously and in a self-consistent way an iterative approach was provided.

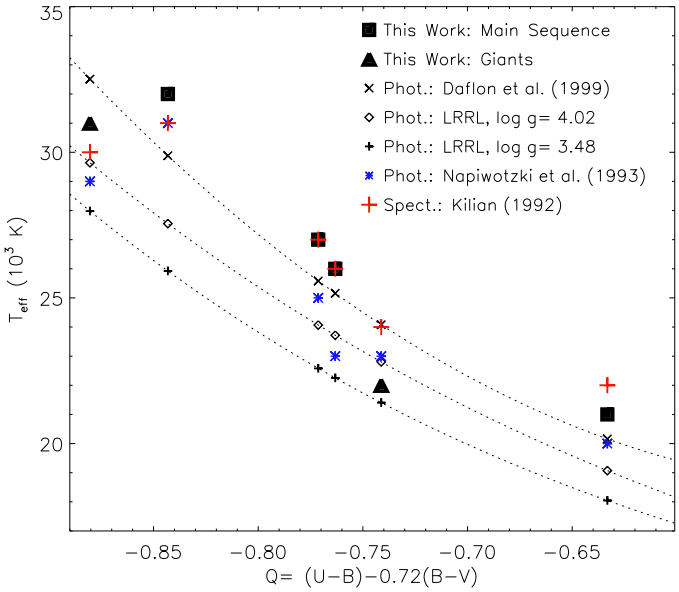

Figure 6.16: Comparison of the final $T_{\rm eff}$ for the sample stars with values derived from photometric calibrations: $T_{\rm eff}(Q)$ (Daflon et al. 1999; Lyubimkov et al. 2002: LRRL) and $T_{\rm eff}([u-b])$ (Napiwotzki et al. 1993). Photometric indices are computed from SIMBAD data. Spectroscopic temperatures according to Kilian (1992) are also displayed.

The final values of the present work for $T_{\rm eff}$ are compared with other derivations in Fig. 6.16. The comparison concentrates on widely employed photometric $T_{\rm eff}$-calibrations, which provide a fast determination of atmospheric parameters as required for the analysis of larger samples of stars. This includes methods using broad-band Johnson photometry, like the reddening-free Q index (Daflon et al. 1999; Lyubimkov et al. 2002) or small-band Strömgren photometry, as the $T_{\rm eff}([u-b])$ calibration of Napiwotzki et al. (1993). The required Johnson and Strömgren magnitudes for the individual stars are adopted from the SIMBAD database. The discrepancies can be large, amounting up to $\sim$4000 K. This can be much larger than the offsets studied in Sect. 6.2.4. The differences in abundance from C II and C III can then achieve factors $\gtrsim$5, similar to what is found in previous studies, e.g. Daflon et al. (2001b). The $T_{\rm eff}$-values of this work are typically higher than those from the photometric estimates. The sample of stars analysed here is too small to facilitate an improved empirical $T_{\rm eff}(Q)$-calibration on its own. However, there is an indication that giants have cooler atmospheres than main sequence stars at the same photometric index. This is qualitatively in agreement with the findings of Lyubimkov et al. (2002).

Spectroscopic $T_{\rm eff}$-determinations by Kilian (1992) are also shown in Fig. 6.16. Kilian based her study on line-blanketed LTE model atmospheres of Gold (1984), grids of non-LTE line profiles for hydrogen (Herrero 1987) and non-LTE ionization

equilibria of Si II-IV (using the model atom of Becker & Butler 1990). Therefore, her approach is conceptually the most similar to the present one despite considerable progress made over the past 15 years, and, as a consequence, gives the closest agreement with the values derived in this Thesis work (except for one giant).

The available photometric calibrations for $T_{\rm eff}$-determinations in early B-type stars allow $T_{\rm eff}$ values to be estimated. These can be used as starting points for a further refinement of the atmospheric parameters via well-understood spectroscopic indicators. In the optimum case the model should agree with all available indicators simultaneously: multiple H and He lines and metal ionization equilibria. All atmospheric parameters could then be tightly constrained. Such a step is essential if the 1σ-uncertainties in the abundance analysis are required to be smaller than a factor $\sim$2 ($\sim$0.3 dex).

6.5 The Stellar Present-Day C Abundance in the Solar Neighbourhood

Early-type stars can act as tracers for the present-day chemical composition in the solar neighbourhood. The small sample of stars analysed here is suited to address this topic, as the objects are randomly distributed over nearby OB associations (three stars, see Table 6.2) and the field (the other stars). A highly-homogeneous carbon abundance of $\epsilon({\rm C}) = 8.32\pm0.04$ (1σ statistical uncertainty) is found for the sample. In continuation of the discussion in the last section this value is compared with results from previous studies of early B-type stars in LTE and non-LTE. Mean abundances, statistical 1σ-uncertainties and the number of analysed stars in the individual studies are summarised in Table 6.4. A visualisation of the abundance distributions is provided in Fig. 6.17. All stars are located at distances shorter than $\sim$1 kpc from the Sun and at galactocentric distances $R_{\rm g}$ within up to 500 pc difference with respect to the location of the Sun $R_{\rm g}^{\odot}$.

LTE. The abundances from Kane et al. (1980) are much lower than the present values. They also show a large spread in abundance ($\sim$1.3 dex), which may be a consequence of the neglect of non-LTE effects for the line-formation calculations of C II λ4267 Å (the only line analysed) and of the use of a photometric $T_{\rm eff}$-scale (from Strömgren indices), see Sect. 6.4.2. Two stars of the present sample are discussed by Kane et al. as well. They derive $\epsilon({\rm C}) = 7.36$ for τ Sco and $\epsilon({\rm C}) = 7.97$ for HR 5285 (χ Cen), in contrast to the results derived in the present work: $\epsilon({\rm C}) = 8.30\pm0.12$ and 8.29 ± 0.05, respectively (see Table 6.2).

Two other LTE studies, not displayed in Fig. 6.17, also provide lower carbon abundances from early B-type stars in the solar vicinity. Barnett & McKeith (1988) base their effective temperatures on photometric calibrations and derive the carbon abundances from the C II $\lambda\lambda$ 6578/82 Å multiplet. Note that

they reject several stars, like τ Sco at $\epsilon(\mathrm{C}) = 7.24$, for computing their average value: $\epsilon(\mathrm{C}) = 8.2 \pm 0.2$ (all their stars are considered in Table 6.4). More recent LTE results by Rolleston et al. (2000) indicate the so far most depleted carbon abundances in the solar neighbourhood. Their results are obtained from the analysis of the non-LTE-sensitive C II $\lambda\lambda$ 3920 and 6578/82 Å lines. Their abundance of the Cep OB3 association is considered here.

Non-LTE. On the other hand, non-LTE analyses (based on the Eber & Butler model atom, using different linelists) find systematically higher abundances than the LTE studies. However, a large spread in abundance is found for each sample.

The present results can be directly compared with those of the purely spectroscopic study of Kilian (1992). She derived carbon abundances for stars in three OB associations (Ori OB1, Sco-Cen, Sgr OB1) and the field from up to 6 unblended C II transitions involving autoionization levels[5] in the spectral range between ∼4000 to 5000 Å. All the programme stars of the present work are included in Kilian's study, her carbon abundances for these six stars tracing almost the entire width of her total abundance distribution. A mean $\epsilon(\mathrm{C}) = 8.19 \pm 0.12$ is derived from the six stars when adopting her results. This comparison is highly important as it shows that a careful analysis may drastically reduce the statistical scatter and may also imply a considerable systematic shift of the mean abundance (towards a higher value in this case). Similar to Kilian, Gummersbach et al. (1998, not shown in Fig. 6.17) also performed a consistent spectroscopic analysis of five stars in the solar vicinity as part of their Galactic abundance gradient study with improved model atmospheres (ATLAS9). Only one C II line involving autoionization levels was used for the abundance analysis. Their results also indicate systematically lower abundances and a considerable spread.

Examples of non-LTE analyses for larger samples of stars based on effective temperatures derived from photometric calibrations are also displayed in Fig. 6.17. Gies & Lambert (1992) and Cunha & Lambert (1994) derived T_{eff} from calibrations based on Strömgren photometry and non-LTE abundances from the C II multiplet around λ5145 Å and where possible from C II $\lambda\lambda$5648/62 Å. Both multiplets originate in the quartet spin system and they are almost unaffected by non-LTE effects. For the comparison five supergiant stars have been excluded from the sample of Gies & Lambert (1992). These objects may expose nuclear-processed material at their surface to a much higher degree than main sequence and giant stars, and they are too far away to be considered members of the solar neighbourhood. Gies & Lambert (1992) have two stars in common with the present sample, indicating systematically lower abundances: for HR 2928 $\Delta\epsilon(\mathrm{C}) \simeq -0.3$ dex and for HR 1861 $\Delta\epsilon(\mathrm{C}) \simeq -0.2$ dex (from the same lines). They also consider the doublet C II $\lambda\lambda$6578/82 Å for several stars of their

[5]Unfortunately these lines are not included explicity in the presents spectrum synthesis, such that it is not possible to study sources of systematic discrepancies in more detail.

Table 6.4: Carbon abundances from OB stars in the solar neighbourhood.

Study	ϵ(C)	# stars
non-LTE		
present work	**8.32±0.04**	6
Kilian (1992)	8.23±0.15	20
Kilian (1992): present sample	8.19±0.12	6
Gies & Lambert (1992)	8.20±0.16	31
Cunha & Lambert (1994)	8.40±0.11	15
Gummersbach et al. (1998)	8.20±0.11	5
Andrievsky et al. (1999)	8.21±0.19	10
Daflon et al. (1999, 2001a)	8.22±0.13	9
LTE		
Kane at al. (1980)	7.77±0.32	28
Barnett & McKeith (1988)	8.15±0.33	12
Rolleston et al. (2000)	7.63±0.16	4

sample, but obtain even lower abundances compared to the lines from the quartet spin system (by approximately another −0.3 dex). Cunha & Lambert (1994) have only one star in common with us, HR 1861. They found a similar abundance for this star as Gies & Lambert (1992). More recently, Daflon et al. (1999, 2001a) derived temperatures from their calibration of the Johnson Q-parameter and non-LTE abundances from the C II multiplet around λ5145 Å. In the present comparison only stars in the Cep OB2, Cyg OB7 and Lac OB1 associations are considered, their other objects are too distant. None of the present programme stars is included in their sample. Finally, Andrievsky et al. (1999) estimated their atmospheric parameters ($T_{\rm eff}$, $\log g$) from photometry alone. Their carbon abundances are essentially based on the C II $\lambda\lambda$5122-5151 and the 6578/82 Å multiplets.

All the data on carbon abundances from early-type stars summarised above were derived from the physical interpretation of observation, which may be affected by many sources of systematic error (see Sect. 6.2). These data are interpreted in turn to test models of massive star evolution *and* the chemical evolution of the Galaxy. These in turn are anchor points for the interpretation of stellar and galactochemical evolution. Therefore it is important to analyse the conclusions drawn from a diagram like Fig. 6.17 in this context.

LTE abundance studies are excluded from the further discussion, as they have been shown to be systematically biased. Previous non-LTE studies all show a broad range of carbon abundances in the solar neighbourhood, spanning a factor of ∼10 in total. A cumulative value of ϵ(C) = 8.25±0.16 can be derived from

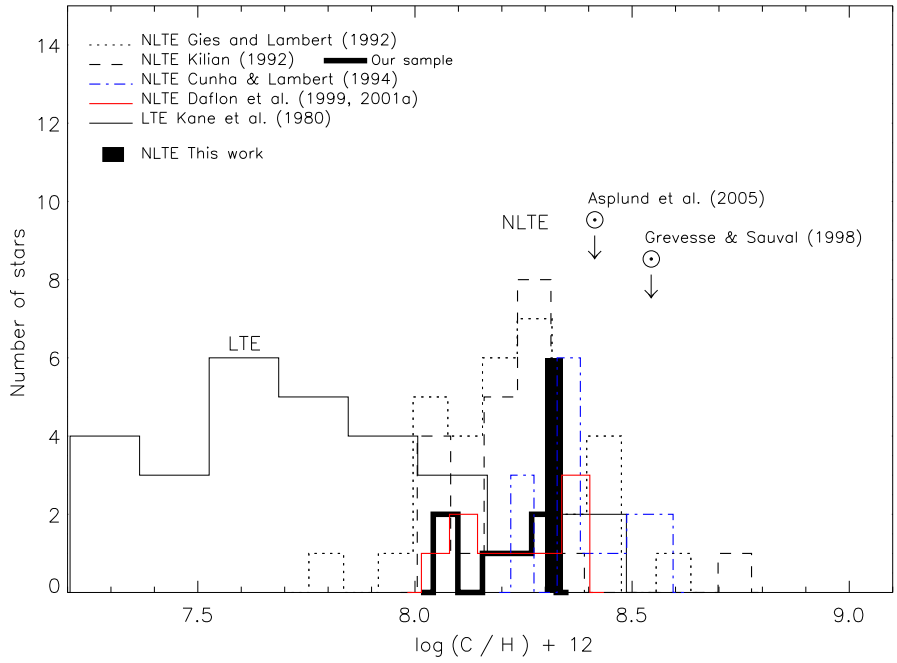

Figure 6.17: Comparison of carbon abundances derived from the present sample of early B-type stars in the solar vicinity with results from the literature for similar objects ($R_{\rm g} - R_{\rm g}^{\odot} \leq 500$ pc, the stars belong to the field and to OB associations) and with the most recent solar values. The binsize of the histograms is related to the statistical uncertainty of each sample. The present sample is not large enough for a statistical comparison, therefore a column with a thickness of the uncertainty is displayed. The programme stars coincide with six objects from Kilian (1992): her abundances show a larger spread for these. More objects need to be analysed in order to improve on the statistics. Note that the systematic effects on the carbon abundances due to rotational mixing in the course of stellar evolution and due to the Galactic abundance gradient should be only of the order of the uncertainty found here, see the text for details.

the 75 measurements discussed in Fig. 6.17, similar to that is derived by the individual studies.
If such large spread were realistic its physical description would require:
I) mechanisms that alter the atmospheric structure, such as sufficiently strong magnetic fields or diffusion/radiative levitation processes acting on short timescales and independent of atmospheric parameters and evolutionary age. This would imply that the basic assumption of homogeneity of the atmosphere may be no longer valid and as a consequence the modelling techniques applied so far may be inadequate; and/or
II) extremely efficient depletion mechanisms in the course of stellar evolution,

Table 6.5: Carbon abundances of different objects in the solar vicinity.

Objects	ϵ(C)	Source
B stars (pristine value)	**8.35±0.05**	present work
B stars	8.25±0.08	Herrero (2003)
Orion H II (gas)	8.42±0.02	Esteban et al. (2004)
Orion H II (gas+dust)	8.52±0.02	Esteban et al. (2004)
young F and G stars	8.55±0.10	Sofia & Meyer (2001)
ISM	8.15±0.06	Sofia & Meyer (2001)
Sun	8.39±0.05	Asplund et al. (2005)
Sun	8.52±0.06	Grevesse & Sauval (1998)

by one to two orders of magnitude larger than currently predicted (e.g. Meynet & Maeder 2003). Already on the Main Sequence mixing with matter from the stellar core would require a higher efficiency than currently predicted for convection during the first dredge-up. Eventually, also enrichment mechanisms may be required which contradict nucleosynthesis (the 3α-process is not active in OB dwarfs and giants, carbon is instead depleted by the CNO cycle); and/or
III) an enormous chemical inhomogeneity of the present-day interstellar material in the solar neighbourhood out of which the stars have been formed. This would require the possibility to change abundances practically instantly even within single clusters by amounts that are otherwise attributed to the past ∼12 Gyrs of Galactochemical evolution (e.g. Chiappini et al. 2003).

The present work avoids all these fundamental problems. It implies homogeneous abundances after improving the modelling *and* the analysis methodology, bringing all model aspects into agreement with high quality observed spectra at once, which was not achieved so far. It conforms with the finding of a *highly uniform* gas-phase carbon abundance in the interstellar medium (out to distances of 1.5 kpc from the Sun, e.g. Sofia & Meyer 2001, and references therein), despite a systematic offset of the absolute value because of the dust contribution. The uncertainties of that indicator (see Table 6.5) are determined by the accuracy to which the oscillator strengths of the resonance lines in the UV are known, and should not exceed more than ∼10%.

The present work also agrees with galactochemical evolution models, which predict homogeneous abundances in the solar neighbourhood (e.g. Chiappini et al. 2003). A variety of hydrodynamic processes should keep the ISM chemically well-mixed on small time-scales (Roy & Kunth 1995). The variation due to the Galactic abundance gradient should amount to up to ∼0.04–0.08 dex kpc^{-1} (one kpc is the maximum galactocentric distance sampled in our comparison). Another aspect concerns the notably sub-solar abundances from early-type stars found so far (e.g. Herrero 2003, with respect to the old solar standard, Grevesse

& Sauval 1998 – see Table 6.5). The present findings remedy the situation, in particular if accounting for the recently revised solar carbon abundance (Asplund et al. 2005, see also Table 6.5). Galactochemical evolution models predict an enrichment of the carbon abundance by ∼10-20% (0.04-0.08 dex) over the past 4.5 Gyrs since the birth of the Sun, depending on the model assumptions. The remaining discrepancies can now be explained much more easily by invoking the usual assumptions: the birth of the Sun in a slightly more metal-rich region of the Galaxy and subsequent orbit diffusion or a recent infall of metal-poor gas to the ISM in the solar neighbourhood.

Finally, rotationally-induced mixing with CN-processed material from the core may change the atmospheric composition. The effect is expected to increase with initial angular momentum of a star and with evolutionary age. Theory predicts a depletion of carbon by ∼0.03 dex for a star of 20 $M_{\odot}$ with initial rotational velocity 300 $km\,s^{-1}$ evolving from the zero-age Main Sequence to the end of the Main Sequence stage, reaching ∼0.15 dex in the supergiant stage (e.g. Meynet & Maeder 2003). The presence of a magnetic field may amplify rotational mixing (Maeder & Meynet 2005), however the effects on abundances are not expected to exceed a factor ∼2. As absolute rotational velocities of stars can be measured only for a few exceptionally cases, this topic can be addressed comprehensively only by a statistical approach. The sample of stars analysed in this work is not large enough for this. However, no significant trend of carbon abundances with evolutionary age is found for these apparently slow-rotating stars (only τ Sco is suggested to be a *real* slow rotator, Donati et al. 2006). The abundances derived may not correspond to the pristine values nonetheless, but it is unlikely that all the stars are very fast rotators seen pole-on. Small corrections by up to ∼+0.05 dex per star (depending on evolution stage) are predicted by theory for objects of average rotation. A correction of ϵ(C)=+0.03 dex for the average value of the present sample is derived from considering carbon and nitrogen simultaneously (Nieva & Przybilla 2007c). The nitrogen abundances have been obtained from ∼20–70 transitions per star using the same analysis methodology and the same atmospheric parameters as derived here, applying an updated model atom of Przybilla & Butler (2001). The correction to carbon allows us to derive an average pristine abundance.

This pristine C abundance derived from early B-type stars in the solar neighbourhood is compared with other indicators in Table 6.5. The value is not only in agreement with the revised solar abundance but also with the gas-phase abundance derived for the Orion nebula. The finding of a uniform abundance matches with a homogeneous interstellar medium abundance. A disagreement is found only with abundances from young F & G-type stars. This may be resolved when hydrodynamic 3D-analyses of late-type stars become routine, as the discrepancy is similar to the difference between the old and the revised solar standard, which is the result of such an improved analysis. The conclusion of Sofia & Meyer (2001) that B-type stars are not reliable proxies for present-day abundances in the solar

neighbourhood may need a revision in view of the present results.

Despite the small sample size analysed so far, the highly accurate results found here indicate that the sub-solar average value and the large scatter of carbon abundances in early-type stars found in previous non-LTE studies could be mostly a consequence of systematic uncertainties. These may be easily introduced by the choice of inappropriate atomic data and/or stellar parameters, as it was shown here. However, a confirmation of these findings from analysis of a larger sample of stars is required, also for other elements.

6.6 Summary

The motivation of this work was the solution of a long-standing problem in stellar astrophysics: the reliable determination of carbon abundances from early-type stars. For this purpose a sophisticated C II/III/IV model atom for non-LTE line-formation calculations was constructed, based on input atomic data that were carefully selected by an empirical calibration process. This was performed through an extensive iteration scheme that allow the input atomic data and simultaneously the atmospheric parameters of the programme stars to be constrained, which is the basis for all further studies. The calibration sample consists of six bright and apparently slow-rotating early B-type stars in the solar neighbourhood, with high-S/N, high-resolution spectra and a broad wavelength coverage.

The C II/III/IV ionization balance gives atmospheric parameters that are highly consistent with previous spectroscopic analyses: results from a non-LTE study of hydrogen and helium in the visual and in the near-IR, including the establishment of the He I/II ionization equilibrium in the hotter stars, and the reproduction of the spectral energy distributions from the UV to the near-IR (see Chapter 5). All carbon lines considered here, from up to three ionization stages, indicate similar abundances. The statistical 1σ-uncertainties of the carbon abundance in each star are of the order $\sim$0.05-0.10 dex. The systematic 1σ-uncertainties are estimated to be $\sim$0.10-0.15 dex. The resulting average carbon abundance from C II/III/IV in the sample stars is highly uniform, $\varepsilon(\mathrm{C}) = 8.32 \pm 0.04$.

These results of unprecedented precision provide important constraints for stellar evolution and the chemical evolution of the Galaxy, despite the small sample size: I) They suggest that carbon depletion due to rotational mixing in the course of stellar evolution is small for stars without excessive initial angular momentum (by $<$0.05 dex) up to the giant stage, in agreement with theoretical predictions. II) In consequence they suggest that the present-day carbon abundance in the solar neighbourhood is higher and much more homogeneous than indicated by previous work on early-type stars. This is consistent with the uniform abundance found in studies of the ISM and with predictions from models

of the chemical evolution of the Galaxy. Moreover,the re-evaluated stellar value is in agreement with the gas-phase abundance derived for the Orion H II region and the recently revised solar abundance.

It was also shown how important is the careful choice of input atomic data for non-LTE analyses. Not only accurate data for radiative transitions are required but also for collisional transitions. The carbon abundance analysis also turned out to react highly sensitively to the choice of atmospheric parameters, in particular to effective temperatures.

Chapter 7

Conclusions

The motivation of this work was to find a solution of a long-standing problem in stellar astrophysics: the reliable determination of carbon abundances from OB-type stars. For this purpose, improvements in the spectral modelling *and* in the quantitative analysis of observed spectra are made and further applied to a sample of six stars randomly distributed in the solar vicinity, covering a wide parameter range. The spectra have high-S/N, high resolution and broad wavelength coverage.

In a first step, a hybrid non-LTE approach, allowing for departures from local thermodynamic equilibrium LTE in the spectrum synthesis, has been *thoroughly* tested for H and He line-formation calculations in OB stars for the first time. Such approach is often employed in the literature for analyses of metal lines. The present analysis uses recently improved model atoms and is much more extensive than published work, which considered selected lines only. The synthetic spectra match simultaneously almost all measurable hydrogen and helium lines in the optical and (where available) also in the near-infrared spectral range of the programme stars, with only a few well-understood exceptions.

The comparison of state-of-the-art line-blanketed non-LTE (OSTAR2002 grid of Lanz & Hubeny 2003) and LTE (Padova grid by Munari et al. 2005) models confirms that the atmospheric structure of dwarf and giant OB stars is described well under the assumption of LTE, but their spectral energy distribution and, most importantly, their line spectra are not. For these stars in the range $20\,000\,\mathrm{K} \leq T_{\mathrm{eff}} \leq 35\,000\,\mathrm{K}$ and $3.0 \leq \log g \leq 4.5$, the present hybrid non-LTE approach is equivalent to full hydrostatic non-LTE computations. It succeeds also in providing synthetic spectra that correctly reproduce the observed He I singlet lines, avoiding inconsistencies recently reported in the literature. In contrast to this, pure LTE modelling based on the Padova grid (or equivalent computations with ATLAS9+SYNTHE) may give rise to considerable systematic errors in the atmospheric parameter determination (T_{eff}, $\log g$) and to subsequent elemental abundance studies for the hotter stars in particular.

In a second step, a sophisticated C II/III/IV model atom for non-LTE line-formation calculations was constructed, based on input atomic data carefully selected in an empirical calibration process. This was performed through a self-consistent quantitative spectrum analysis using an extensive iteration scheme which facilitated both the input atomic data and the atmospheric parameters of the calibration stars to be constrained accurately. The C II/III/IV ionization balance is successfully established for all analysed carbon lines of the sample, which provide similar abundances. The linelist includes 40 transitions suitable for analysis over a wide wavelength range. In particular, the strongest features, of highest importance for extragalactic applications, are also consistently modelled. The statistical 1σ-uncertainties of the carbon abundance in each star are of the order 0.05-0.10 dex. The systematic 1σ-uncertainties are estimated to be $\sim$0.10-0.15 dex. Typically, the systematic uncertainties of the abundance determination remain mostly undetermined in literature, and statistical uncertainties are of a factor $\sim$2–3.

Determinations of carbon abundances react highly sensitive to modifications of the atmospheric parameters. The importance of this was vastly underestimated in previous work. A self-consistent analysis provides atmospheric parameters with unprecedented accuracy and with reduced systematic error: for effective temperature the uncertainties are as low as $\sim$1% (literature: 5-10%), for surface gravity $\sim$10% (literature: $\sim$25%). The systematic uncertainties in literature are however found to be much larger than the statistical ones in the present work: up to $\sim$20% for temperatures and $\sim$50% for surface gravities. The atmospheric parameters derived from the carbon ionization equilibria are highly consistent with other indicators investigated in the present work: results from a non-LTE study of hydrogen and helium in the visual and in the near-IR, including an establishment of the He I/II ionization equilibrium in the hotter stars, and the reproduction of the spectral energy distributions from the ultraviolet to the near-infrared.

The resulting average carbon abundance for the sample stars is highly uniform, $\varepsilon(\mathrm{C}) = 8.32 \pm 0.04$. This result of unprecedented precision provides important constraints for stellar evolution and the chemical evolution of the Galaxy, despite the small sample size which requires improvement on the statistics.

I) It suggest that carbon depletion due to rotational mixing in the course of stellar evolution is small for stars without excessive initial angular momentum (by $<$0.05 dex) up to the giant stage, in agreement with theoretical predictions.

II) In consequence, this result suggests that the present-day carbon abundance in the solar neighbourhood is higher and much more homogeneous than indicated by previous work on early-type stars. This is consistent with the uniform abundance found in studies of the interstellar medium and with predictions from models of the chemical evolution of the Galaxy. Moreover, the carbon abundance derived from OB-stars is now in agreement with the gas-phase abundance of the Orion H II region and the recently revised solar abundance.

This work shows that one should not underestimate the importance of a careful choice of input atomic data for non-LTE analyses. Not only accurate data for radiative transitions are required but also for collisional transitions. The carbon abundance analysis also turned out to react highly sensitive to the choice of atmospheric parameters, in particular to effective temperatures. If not accounted for properly, both factors may result in systematic errors in the interpretation of observed spectra, which cannot be reduced by statistics, i.e. an increase of the sample size of stars to be analysed. Photometric calibrations for effective temperature determinations are found to provide only estimates. Those may be used as starting points in the iteration scheme, but they are not sensitive enough for reliable quantitative spectroscopic analyses. Detailed comparisons and calibrations of models with observed spectra are of highest importance, as these constitute the only empirical constraints for quantitative analyses. Only then can stellar and Galactochemical evolution models be verified in a meaningful way, and the studies be extended to stars in other galaxies.

The present work offers wide perspectives for future studies of chemical abundances from OB-type stars. A straightforward application may be the use of available sophisticated model atoms (N, O, Mg, Si, etc.) for the analysis of the programme stars in order to derive the present-day abundances in the solar vicinity and to verify other ionization equilibria. The calibrated carbon model atom allows a simplified iteration processes to be performed in other stars, i.e. concentrating only on the stellar parameter and abundance determination, since the atomic data are already selected. An analysis of a larger sample of stars in the solar vicinity can constrain the present findings with higher significance. Analyses of more distant stars can provide an accurate derivation of the Galactic abundance gradient. OB-type stars in the Magellanic Clouds and in other nearby galaxies in the Local Group may also be accurately studied using the present generation of large telescopes, with the limiting factor defined by the quality of the observed spectra. The next generation of telescopes, that are currently in the design phase, will allow even stars in more distant galaxies, of other types than currently accessible, to be analysed.

Appendix A

Basis of Échelle Data Reduction

Échelle means ladder in French. In astrophysics, it refers to a diffraction grating in which the lines are ruled much further apart than those of an ordinary grating. Spectrographs using a dispersing element like an ordinary diffraction grating or prism produce a single spectrum. The wavelength range covered by this type of instrument is limited by the size the CCD. An Échelle grating produces a spectrum of very high dispersion, but only over a short wavelength range in each order, implying that the high orders will overlap. In order to overcome this effect a cross-dispersing element is used to produce an order separation in the direction perpendicular to the dispersion. Figure A.1 shows a example of a CCD image of a 2-D spectrum taken with the FEROS (Fiber-fed Extended Range Optical Spectrograph) spectrograph at the MPG/ESO-2.2m telescope in La Silla (Chile). Some characteristic features can be seen in the figure: several absorption lines corresponding to the stellar spectrum, telluric lines (upper right corner), and extra signal due to the incidence of cosmic rays (bright dots). Orders in the upper part have longer wavelengths. For each order the wavelength increases to the right.

The idea of constructing Échelle spectrographs is to work at high orders with the highest efficiency. These instruments offer a reasonably high resolution and a wide wavelength coverage, optimum characteristics for the study of e.g. chemical abundances in stars, in particular for those which have sharp lines. Unfortunately, the data reduction process of an Échelle spectrum can be complex.

Different exposures are performed in an observing run: exposures with closed shutter (for bias elimination), a flat field (for corrections of the CCD pixel sensitivity), a comparison lamp (for wavelength calibration) and finally the stars. The reduction process of an Échelle spectrum from a set of images follows, in principle, a similar procedure than that of a single-order spectrum.

- Bias elimination. The bias reflects the detector electronics influence. It is related with the temperature of the detector.

- Flat fielding. A flat field is the result of illuminating the instrument with

Figure A.1: Example of a 2-D FEROS spectrum.

a uniform source for determining the relative sensitivity of the pixels. Flat fielding is the process of dividing the spectra by a normalised flat-field to remove these sensitivity variations of the system.

- Order detection and extraction. A modelling of the order location on the 2-D spectrum is performed. Then, the flux perpendicular to the dispersion direction is summed up, giving a (extracted) 1-D spectrum. An optimum extraction takes a weighted sum such that the S/N of the extracted spectrum is optimum, allowing the effects of cosmic rays to be reduced.

- Wavelength calibration. Fitting the dispersion relation from a comparison of the spectrum of a lamp of well-identified lines (e.g. Th-Ar).

- Normalization of continuum. Fitting of the blaze function which follows the shape of the 1-D spectrum and normalisation of the continuum to 1.

- Radial velocity correction. This step can be performed by comparison to an appropriate synthetic spectrum.

For Échelle spectra, additional complexity arises because there are more data to extract, the orders can have a more complex shape than those from a single-order instrument, the high dispersion used can make it difficult to distinguish between true spectral features and cosmic-ray events, flat fielding the data can be difficult. In some cases adjacent orders overlap slightly in the spatial direction making accurate background subtraction difficult. Several other sources

of complexity exist, depending on the instrument. For more details on general procedures for Échelle spectra reduction the reader can refer to the didactic description of Churchill (1995) and M. Clayton (www.star.ucl.ac.uk/∼mjc/echelle). The FEROS spectrograph and the reduction process is described in Kaufer et al. (1999), Stahl et al. (1999) and Hensberge (1996, 2001, 2004).

Appendix B

Atomic data for H and He

Important atomic data relevant to the hydrogen and helium line formation in the visual and the near-IR (NIR) are summarised in Table B.1. The data are composed by wavelengths, lower and upper levels involved in the transition, oscillator strengths $\log gf$, their accuracies and sources, also for the detailed Stark-broadening data and some comments.

Table B.1: Atomic data for H and He I/II line formation in the visual and NIR

λ (Å)	Transition	$\log gf$	Acc.	Src.	Broad.	Comment
H I:						
3797.90	2 – 10	−1.511	AA	GRC	SH	
3835.38	2 – 9	−1.362	AA	GRC	SH	
3889.05	2 – 8	−1.192	AA	GRC	SH	
3970.07	2 – 7	−0.993	AA	GRC	SH	blend with interstellar Ca II H
4101.73	2 – 6	−0.753	AA	GRC	SH	
4340.46	2 – 5	−0.447	AA	GRC	SH	
4861.32	2 – 4	−0.020	AA	GRC	SH	
6562.80	2 – 3	0.710	AA	GRC	SH	
8413.32	3 – 19	−1.823	AA	GRC	SH	
8437.96	3 – 18	−1.748	AA	GRC	SH	
8467.26	3 – 17	−1.670	AA	GRC	SH	
8502.49	3 – 16	−1.586	AA	GRC	SH	
8545.39	3 – 15	−1.495	AA	GRC	SH	
8598.39	3 – 14	−1.398	AA	GRC	SH	
8665.02	3 – 13	−1.292	AA	GRC	SH	
8750.47	3 – 12	−1.175	AA	GRC	SH	
He II:						
3796.34	4 – 20	−1.487	AA	GRC	G60, G67	blend with Hϑ
3813.50	4 – 19	−1.414	AA	GRC	G60, G67	
3833.81	4 – 18	−1.337	AA	GRC	G60, G67	blend with Hη
3858.08	4 – 17	−1.255	AA	GRC	G60, G67	
3887.45	4 – 16	−1.166	AA	GRC	G60, G67	blend with Hζ
3923.49	4 – 15	−1.071	AA	GRC	SB[a]	blend with He I
3968.44	4 – 14	−0.967	AA	GRC	SB[a]	blend with Hϵ
4025.61	4 – 13	−0.852	AA	GRC	SB[a]	blend with He I
4100.05	4 – 12	−0.725	AA	GRC	SB	blend with Hδ
4199.84	4 – 11	−0.582	AA	GRC	SB	blend with N III
4338.67	4 – 10	−0.417	AA	GRC	SB	blend with Hγ
4541.59	4 – 9	−0.223	AA	GRC	SB	
4685.70	3 – 4	1.181	AA	GRC	SB	
4859.32	4 – 8	0.014	AA	GRC	SB	blend with Hβ
5411.52	4 – 7	0.321	AA	GRC	SB	
6560.09	4 – 6	0.759	AA	GRC	SB	blend with Hα

[a] Unpublished, priv. comm.; [b] vacuum wavelengths

Accuracy indicators – uncertainties within: AA: 1%; A: 3%

Sources of gf-values: FTS: Fernley et al. (1987); GRC: Green et al. (1957); SPA: Schiff et al. (1971)

Sources for Stark broadening parameters: BCS69: Barnard et al. (1969); C: Cowley (1971); DSB: Dimitrijević & Sahal-Bréchot (1990); G60: Griem (1960); G64: Griem (1964); G67: Griem (1967); GBKO: Griem et al. (1962); S: Shamey (1969); SB: Schöning & Butler (1989); SH: Stehlé & Hutcheon (1999)

Table B.1. continued

λ (Å)	Transition	$\log gf$	Acc.	Src.	Broad.	Comment
He I:						
3819.60	$2p\,^3P^o - 6d\,^3D$	−0.931	A	FTS	DSB	forb. comp. missing
3819.61	$2p\,^3P^o - 6d\,^3D$	−1.153	A	FTS	DSB	...
3819.76	$2p\,^3P^o - 6d\,^3D$	−1.630	A	FTS	DSB	...
3867.47	$2p\,^3P^o - 6s\,^3S$	−2.037	A	FTS	DSB	
3867.48	$2p\,^3P^o - 6s\,^3S$	−2.260	A	FTS	DSB	
3867.63	$2p\,^3P^o - 6s\,^3S$	−2.737	A	FTS	DSB	
3888.60	$2s\,^3S - 3p\,^3P^o$	−1.668	AA	SPA	G64	near core of Hζ
3888.65	$2s\,^3S - 3p\,^3P^o$	−0.765	AA	SPA	G64	...
3926.54	$2p\,^1P^o - 8d\,^1D$	−1.652	A	FTS	DSB	blends by Si III & S II/III
3935.95	$2p\,^1P^o - 8s\,^1S$	−2.772	A	FTS	DSB	
3964.73	$2s\,^1S - 4p\,^1P^o$	−1.290	A	FTS	G64	in wing of Hϵ
4009.26	$2p\,^1P^o - 7d\,^1D$	−1.449	A	FTS	DSB	
4023.98	$2p\,^1P^o - 7s\,^1S$	−2.572	A	FTS	DSB	
4026.18	$2p\,^3P^o - 5d\,^3D$	−2.600	A	FTS	S	
4026.19	$2p\,^3P^o - 5d\,^3D$	−0.633	A	FTS	S	
4026.20	$2p\,^3P^o - 5d\,^3D$	−0.851	A	FTS	S	
4026.36	$2p\,^3P^o - 5d\,^3D$	−1.328	A	FTS	S	
4120.81	$2p\,^3P^o - 5s\,^3S$	−1.722	A	FTS	GBKO	blends O II, C III, & Fe III
4120.82	$2p\,^3P^o - 5s\,^3S$	−1.945	A	FTS	GBKO	...
4120.99	$2p\,^3P^o - 5s\,^3S$	−2.422	A	FTS	GBKO	...
4143.76	$2p\,^1P^o - 6d\,^1D$	−1.203	A	FTS	DSB	blends O II & N II
4168.97	$2p\,^1P^o - 6s\,^1S$	−2.332	A	FTS	DSB	strong blend with O II
4387.93	$2p\,^1P^o - 5d\,^1D$	−0.886	A	FTS	S	
4437.55	$2p\,^1P^o - 5s\,^1S$	−2.026	A	FTS	GBKO	cont. diff. interst. band
4471.47	$2p\,^3P^o - 4d\,^3D$	−0.210	A	FTS	BCS69	
4471.49	$2p\,^3P^o - 4d\,^3D$	−0.432	A	FTS	BCS69	
4471.68	$2p\,^3P^o - 4d\,^3D$	−0.909	A	FTS	BCS69	
4713.14	$2p\,^3P^o - 4s\,^3S$	−1.276	A	FTS	G64	
4713.16	$2p\,^3P^o - 4s\,^3S$	−1.498	A	FTS	G64	
4713.38	$2p\,^3P^o - 4s\,^3S$	−1.976	A	FTS	G64	
4921.93	$2p\,^1P^o - 4d\,^1D$	−0.442	A	FTS	BCS69	forb. comp. to be improved
5015.68	$2s\,^1S - 3p\,^1P^o$	−0.820	AA	SPA	G64	
5047.74	$2p\,^1P^o - 4s\,^1S$	−1.600	A	FTS	GBKO	
5875.60	$2p\,^3P^o - 3d\,^3D$	−1.511	A	FTS	G64	
5875.61	$2p\,^3P^o - 3d\,^3D$	0.480	A	FTS	G64	
5875.63	$2p\,^3P^o - 3d\,^3D$	−0.338	A	FTS	G64	
5875.64	$2p\,^3P^o - 3d\,^3D$	0.138	A	FTS	G64	
5875.97	$2p\,^3P^o - 3d\,^3D$	−0.214	A	FTS	G64	
6678.15	$2p\,^1P^o - 3d\,^1D$	0.328	A	FTS	G64	
7065.18	$2p\,^3P^o - 3s\,^3S$	−0.458	A	FTS	GBKO	weak telluric line cont.
7065.22	$2p\,^3P^o - 3s\,^3S$	−0.680	A	FTS	GBKO	...
7065.71	$2p\,^3P^o - 3s\,^3S$	−1.157	A	FTS	GBKO	...
7281.35	$2p\,^1P^o - 3s\,^1S$	−0.854	A	FTS	GBKO	strong telluric line cont.
10829.09	$2s\,^3S - 2p\,^3P^o$	−0.745	AA	SPA	G64	
10830.25	$2s\,^3S - 2p\,^3P^o$	−0.268	AA	SPA	G64	
10830.34	$2s\,^3S - 2p\,^3P^o$	−0.046	AA	SPA	G64	
20586.92[b]	$2s\,^1S - 2p\,^1P^o$	−0.424	AA	SPA	DSB	strong telluric line cont.
21125.79[b]	$3p\,^3P^o - 4s\,^3S$	−0.138	A	FTS	DSB	
21125.89[b]	$3p\,^3P^o - 4s\,^3S$	−0.360	A	FTS	DSB	
21127.09[b]	$3p\,^3P^o - 4s\,^3S$	−0.837	A	FTS	DSB	
21137.80[b]	$3p\,^1P^o - 4s\,^1S$	−0.527	A	FTS	DSB	

Appendix C

Linefits to H and He

Synthetic profiles for a selection of 6 hydrogen Balmer and 18 He I/II lines in the visual are compared with observation for HR 3055, HR 1861, HR 2928, HR 3468 and HR 5285 in Figs. C.1-C.5. These are the best simultaneous fits within the uncertainties of the parameters from Table 5.1, as obtained in the present work. For a discussion see Sect. 5.3.

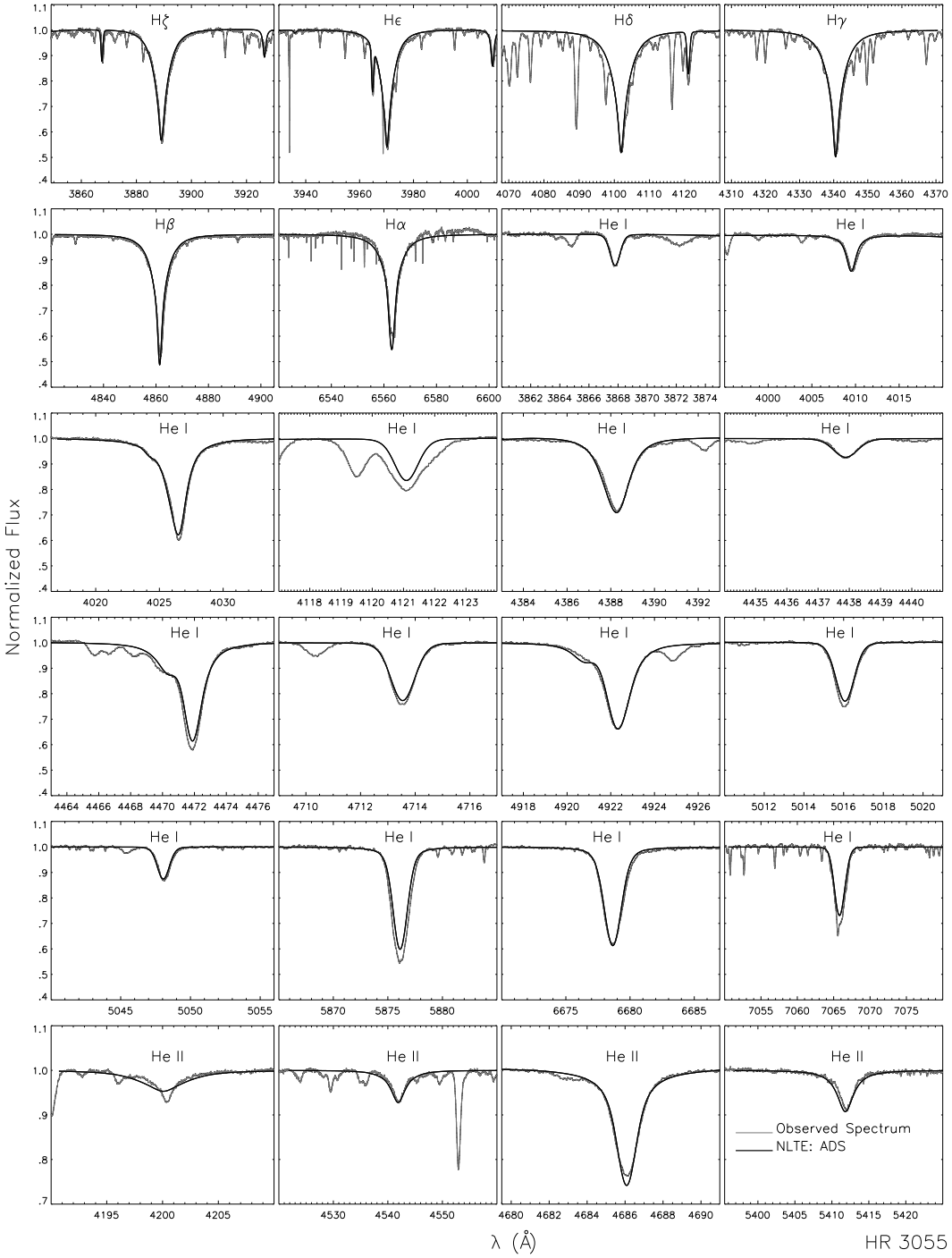

Figure C.1: Non-LTE line fits to observed hydrogen and helium features in HR 3055 (B0 III). Note that the quality of the line fits for Hα and He II λ 4686 Å in particular is better than for τ Sco apparently because of a weaker stellar wind, cf. Fig. 5.5.

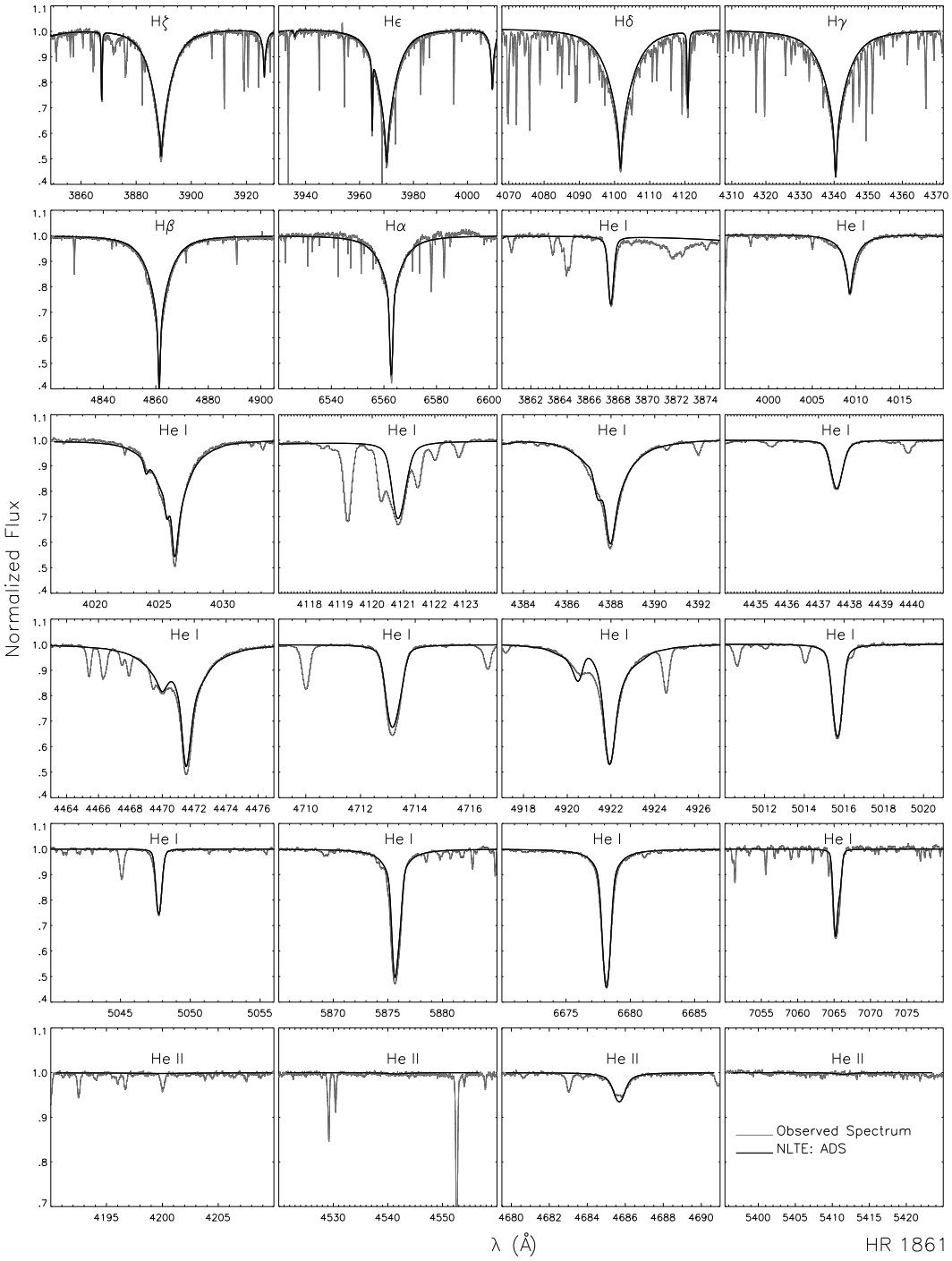

Figure C.2: Line fits for HR 1861 (B1 IV). For atmospheric parameters see Table 5.1, and for further discussion see the text.

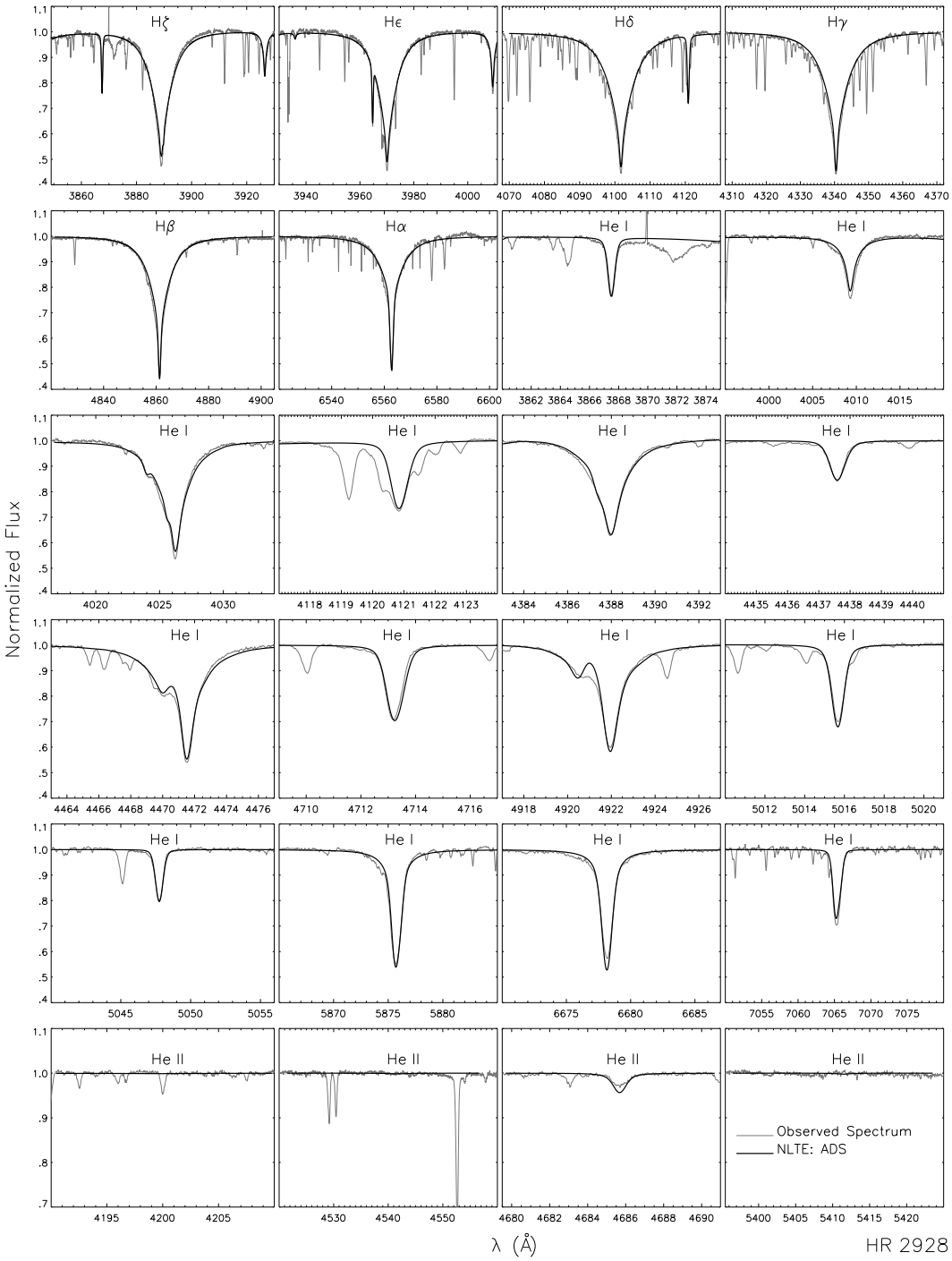

Figure C.3: As Fig. C.2, but for HR 2928 (B1 IV).

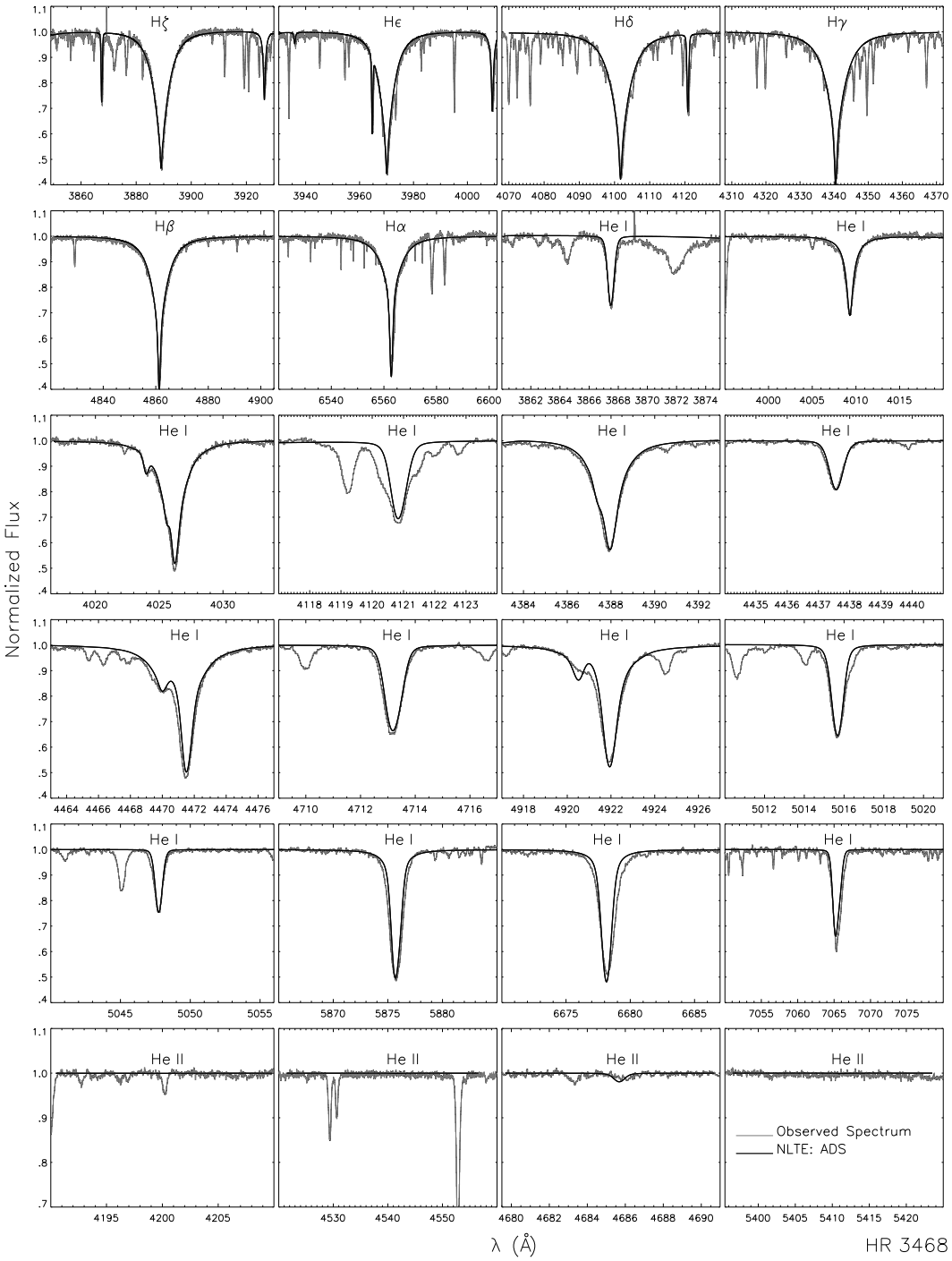

Figure C.4: As Fig. C.2, but for HR 3468 (B1.5 III).

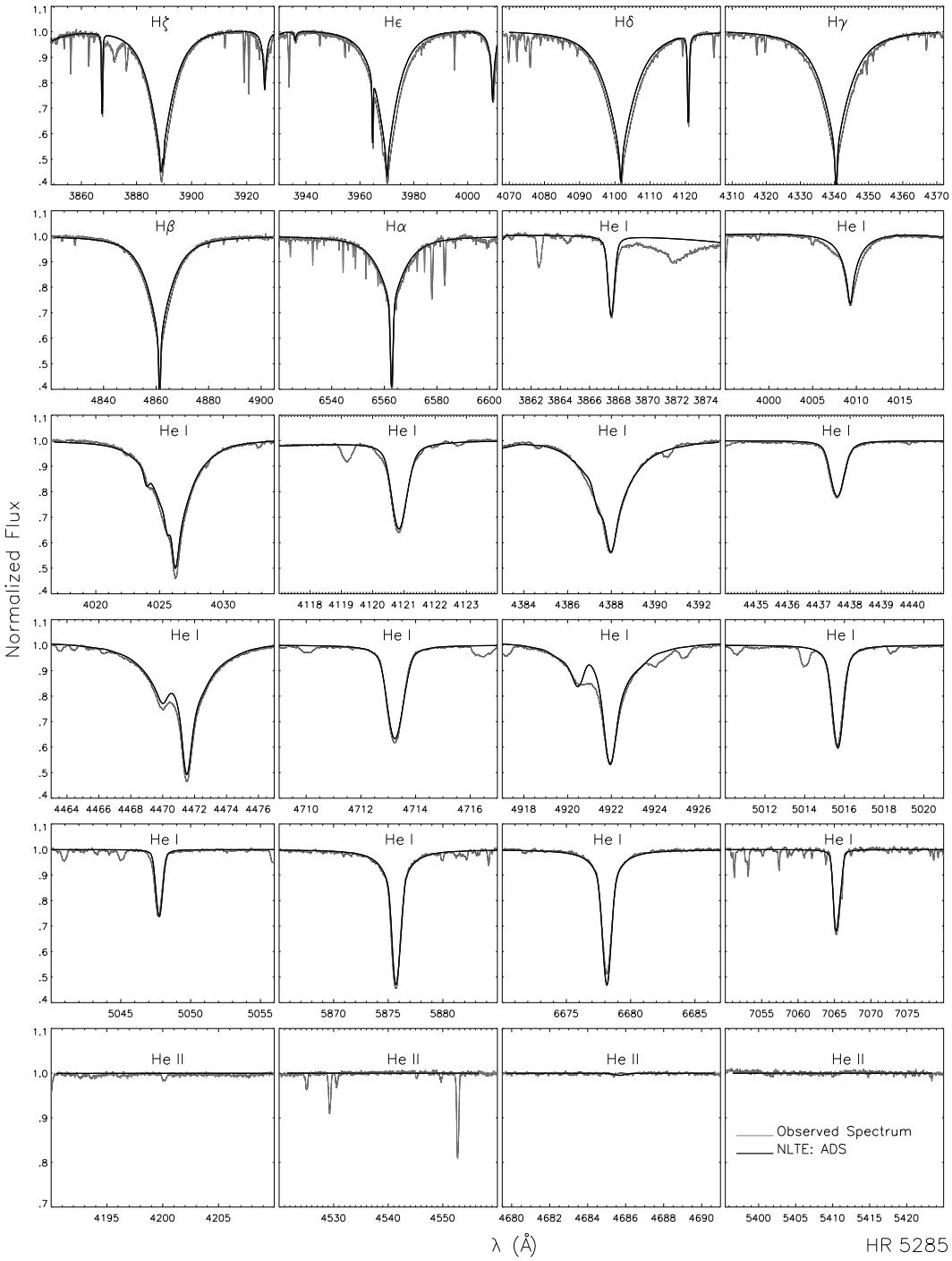

Figure C.5: As Fig. C.2, but for HR 5285 (B2 V).

Appendix D

Linefits to C lines

Synthetic profiles for a almost all analysed carbon lines in HR 3055, HR 1861, HR 2928, HR 5285, HR 3468. These are the best simultaneous fits within the uncertainties of the parameters from Table 5.1. For a discussion see Sect. 6.3.

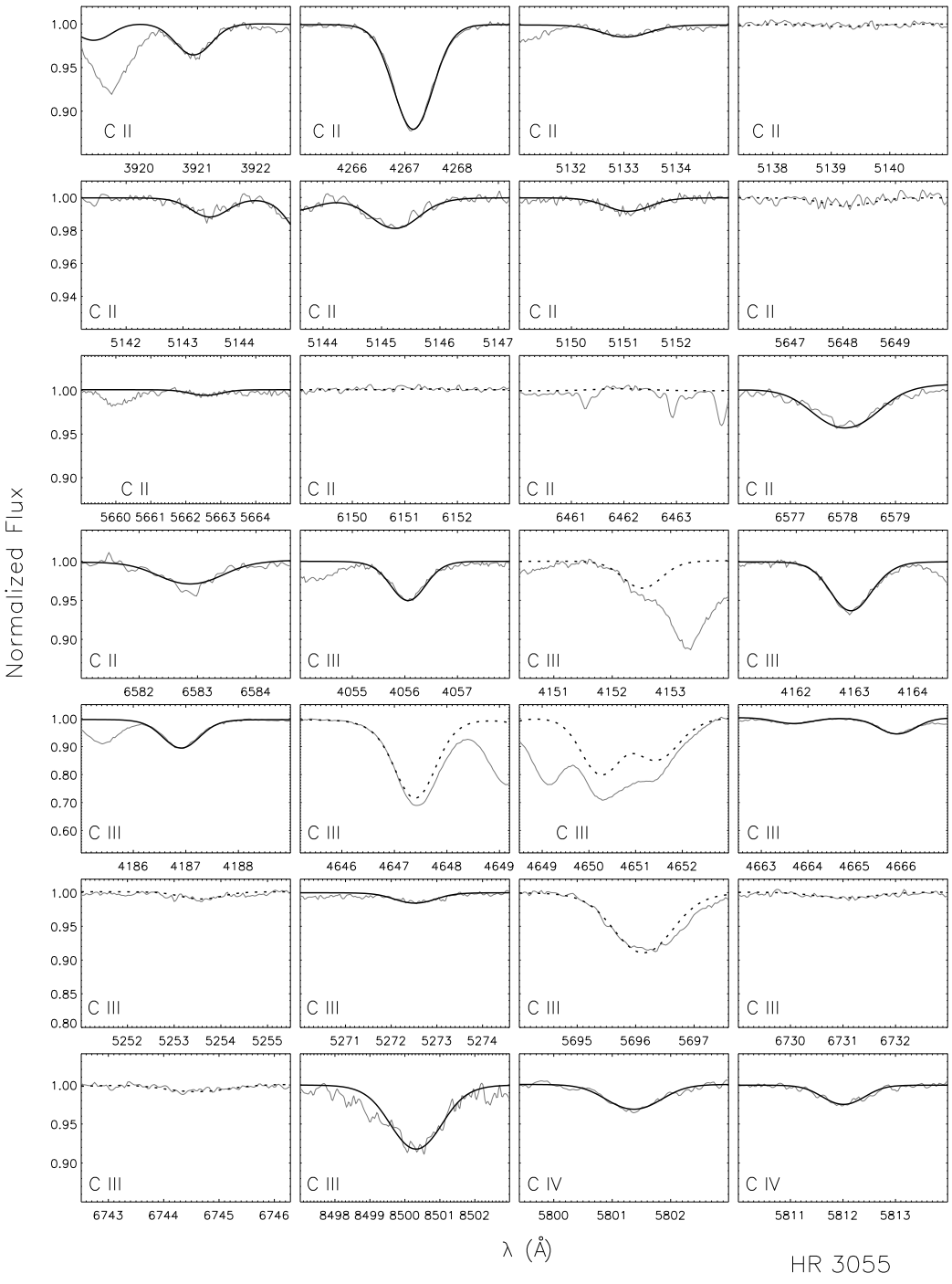

Figure D.1: As Fig. 6.13, but for HR 3055. Dotted lines indicate the features not included in the abundance determination.

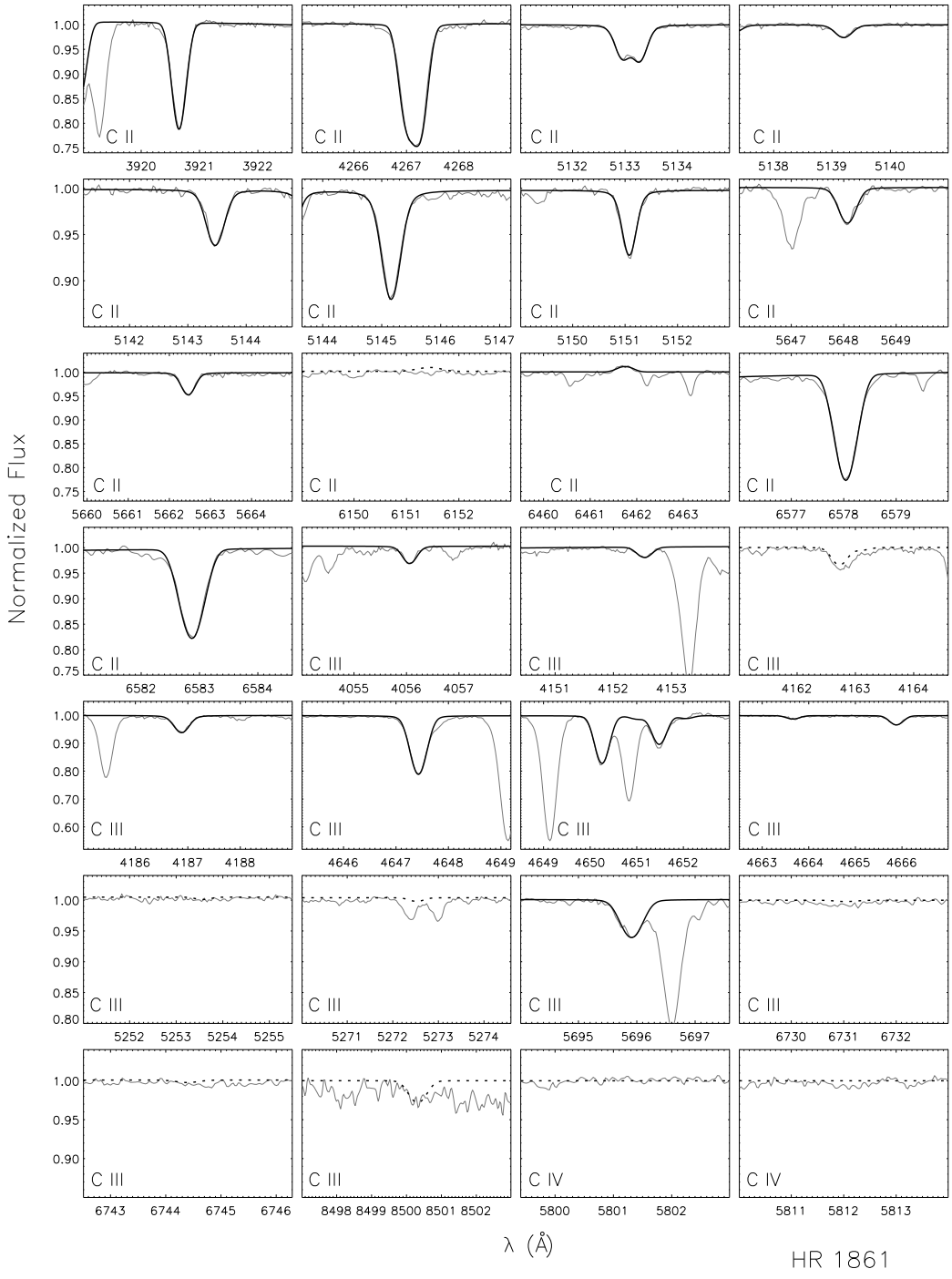

Figure D.2: As Fig. D.1, but for HR 1861.

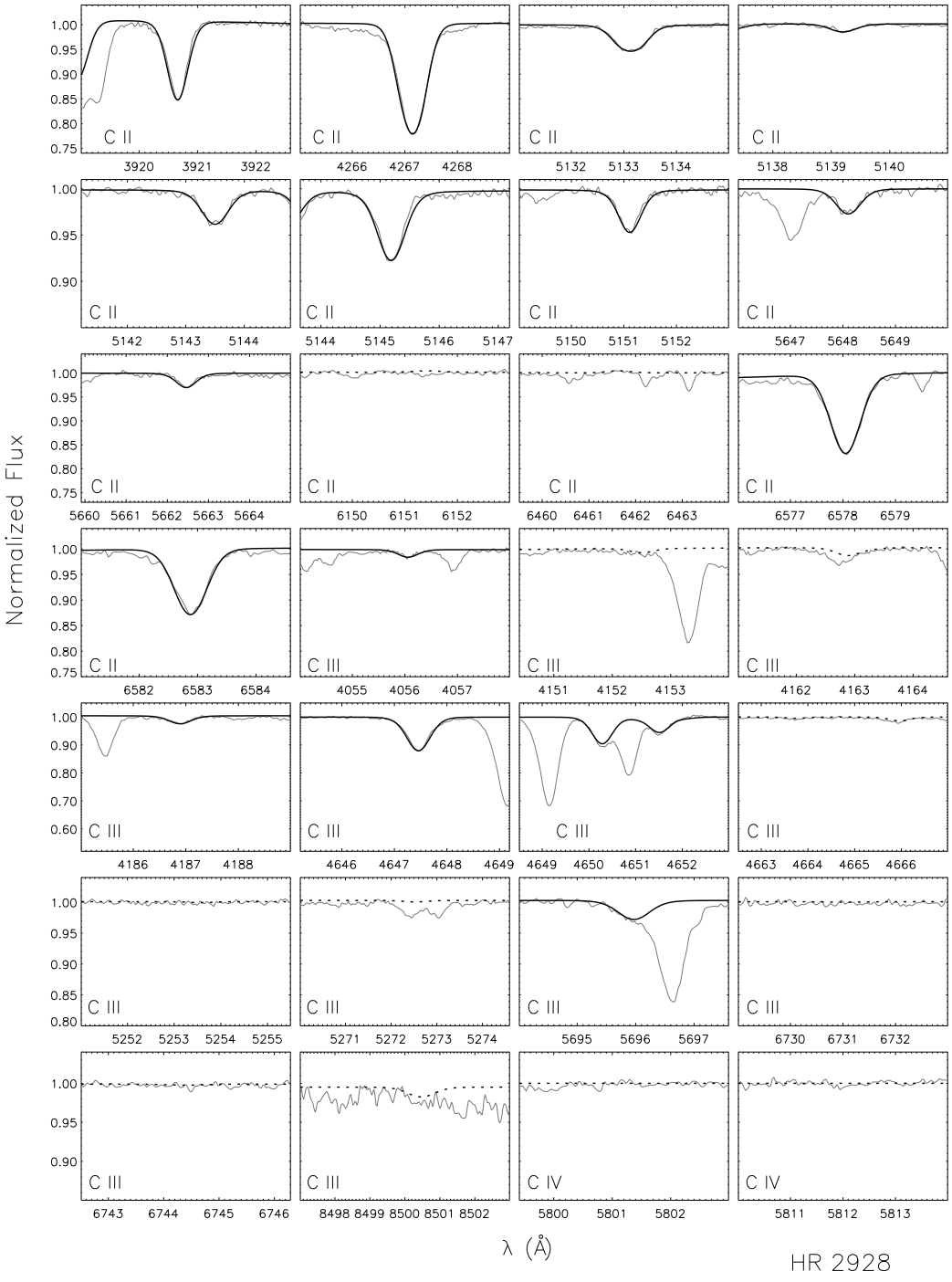

Figure D.3: As Fig. D.1, but for HR 2928.

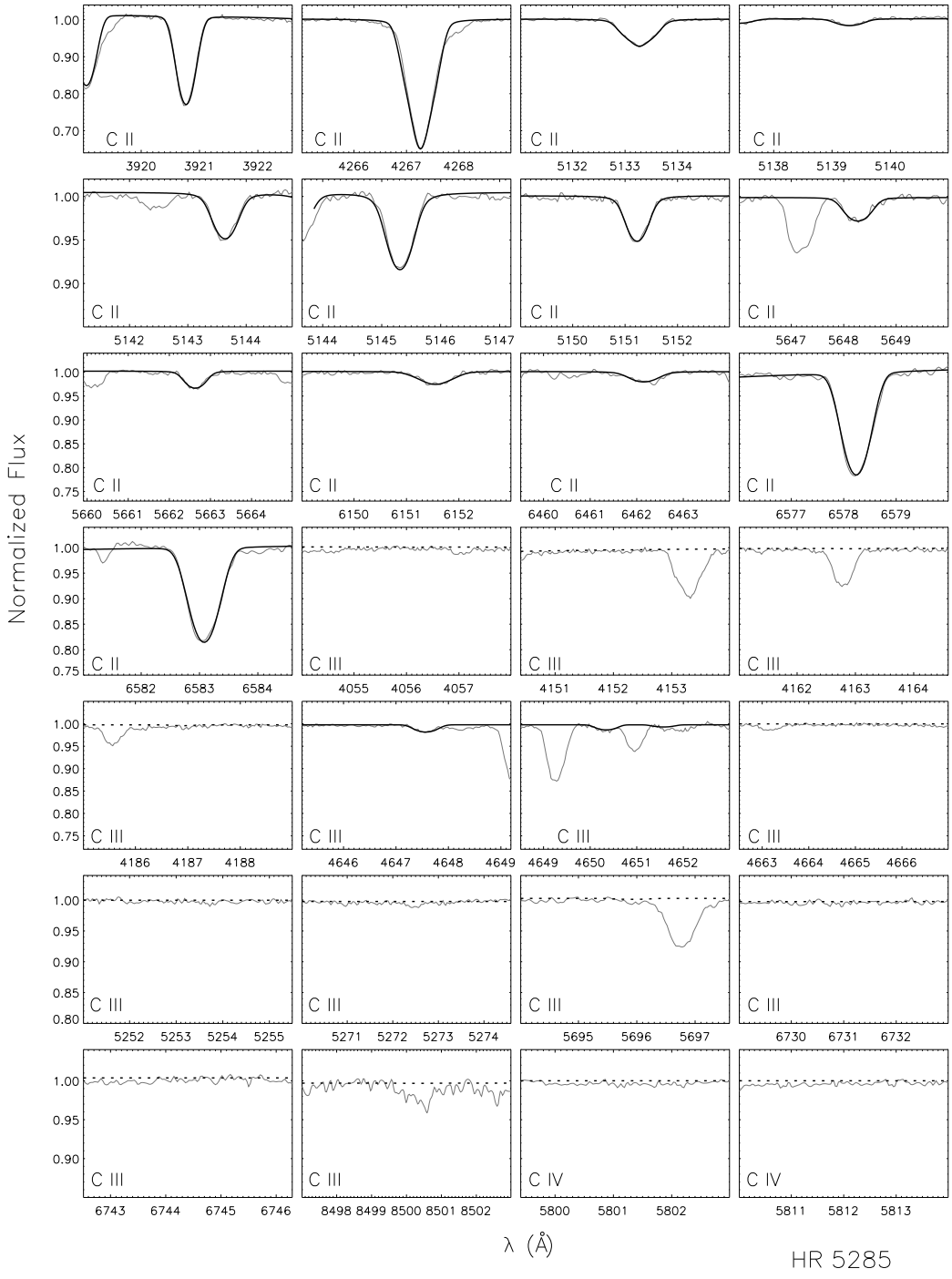

Figure D.4: As Fig. D.1, but for HR 5285.

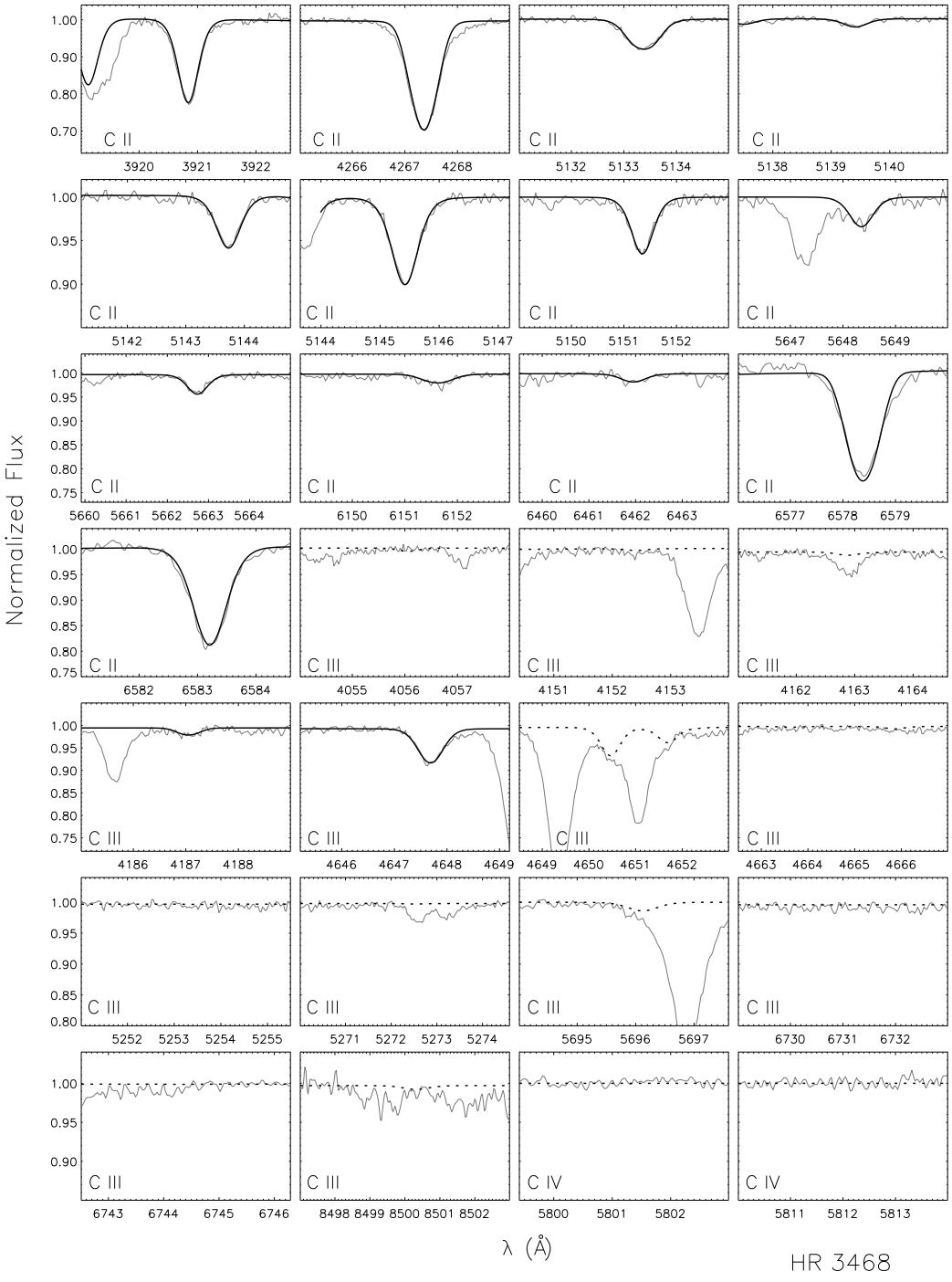

Figure D.5: As Fig. D.1, but for HR 3468.

Bibliography

Adelman, S.J., Pintado, O.I., **Nieva, F.**, et al. 2002, *On the effective temperatures and surface gravities of superficially normal main sequence B and A stars*, A&A, 392, 1031

Aggarval, K. M. & Keenan, F. P. 2004, PSSC, 69, 385

Allen, C.W. 1973, *Astrophysical Quantities*, 3rd Ed. (Athlone Press, London)

Anders, E. & Grevesse, N. 1989, Geochim. Cosmochim. Acta, 53, 197

Andrievsky, S.M., Korotin, S.A., Luck, R.E., & Kostynchuk, L. Yu. 1999, A&A, 350, 598

Asplund, M., Grevesse N. & Sauval, A. J. 2005, in: T. G. Barnes III & F. N. Bash (eds.), *Cosmic Abund. as Records of Stellar Evol. and Nucleosyn.* (ASP, San Francisco), 25

Auer, L.H. & Mihalas, D. 1972, ApJS, 24, 193

Auer, L.H. & Mihalas, D. 1973, ApJS, 25, 433

Balona, L.A. 1993, MNRAS, 260, 795

Balona, L.A. & Jerzykiewicz, M., 1993, MNRAS, 260, 782

Barnard, A.J., Cooper, L., & Shamey, L.J. 1969, A&A, 1, 28

Barnett, E. W. & McKeith, C. D. 1988, MNRAS, 234, 325

Bautista, M. 2000, in: Bautista, M., Kallman, T.R. & Pradhan, A.K. (eds.), *Atomic Data Needs for X-ray Astronomy*, 25 (astro-ph/0006286)

Becker, S. & Butler, K. 1990, A&A, 235, 326

Berrington, K., Eissner, W., & Norrington, P.H. 1995, CPC, 92, 290

Bouret, J.-C., Lanz, T., Hillier, D.J., et al. 2003, ApJ, 595, 1182

Burbidge, E. M., Burbidge, G. R., Fowler, W. A., & Hoyle, F. 1957, Rev. Mod. Phys., 29, 547

Burgess, A. 1961 Mem. Soc. Roy. Sci., Liege 4, 299

Burke, P.G., Hibbert, A., & Robb, W.D. 1971, J. Phys B, 4, 153

Butler, K. & Giddings, J.R. 1985, in *Newsletter of Analysis of Astronomical Spectra*, No. 9 (Univ. London)

Caloi, V. & Cassatella, A. 1995, A&A, 295, 63

Cameron, A. G. 1957, PASP, 69, 201

Cannon, C.J. 1973, J. Quant. Spectrosc. Radiat. Transfer, 13, 627

Chiappini, C., Matteucci, F. & Romano, D. 2001, ApJ, 554, 1044

Chiappini, C., Romano, D., & Matteucci, F. 2003, MNRAS, 339, 63

Cescutti, G., Matteucci, F., Francois, P., & Chiappini, C. 2007, A&A, 462, 943

Condon, E.U., & Shortley, G.H. 1935, *The Theory of Atomic Spectra* (Cambridge University Press, London & New York)

Cowley, C. 1971, Observatory, 91, 139

Crivellari, L., Hubeny, I., & Hummer, D.G.(eds) 1990, *Stellar Atmospheres: Beyond Classical Models*, NATO ASI Series C 152 (Kluwer, Dordrecht)

Cunha, K. & Lambert, D.L. 1992, ApJ, 399, 586

Cunha, K. & Lambert, D. L. 1994, ApJ, 426, 170

Daflon, S. & Cunha, K. 2004, ApJ, 617, 1115

Daflon, S., Cunha, K. & Becker, S. R. 1999, ApJ, 522, 950

Daflon, S., Cunha, K., Becker, S. R. & Smith, V. V. 2001a, ApJ, 552, 309

Daflon, S., Cunha, K., Butler, K. & Smith, V. V. 2001b, ApJ, 563, 325

Dimitrijević, M.S. & Sahal-Bréchot, S. 1990, A&AS, 82, 519

Donati, J.F., Howarth, I.D., Jardine, M.M. et al. 2006, MNRAS, 370, 629

Dufton, P.L., Ryans, R.S.I., Trundle, C., et al. 2005, A&A, 434, 1125

Eber, F. 1987, Diploma Thesis, Ludwig-Maximilians-Universität, München, Germany

Eber, F. & Butler, K. 1988, A&A, 202, 153 (EB)

Eissner, W. 1991, J. Physique (Paris), C1, 3

Eissner, W., Jones, M. & Nussbaumer, H. 1974, CPC , 8, 270

Esteban, C., Peimbert, M., García-Rojas, J., et al. 2004, MNRAS, 355, 229

Evans, C.J., Smartt, S.J., Lee, J.-K., et al. 2005, A&A, 437, 467

Feautrier, P. 1964, C.R. Acad. Sci. Paris, 258, 3189

Fernley, J.A., Taylor, K.T., & Seaton, M.J. 1987, J. Phys. B, 20, 6457

Froese Fischer, C. 1977, *The Hartree-Fock Model for Atoms* (Wiley, New York)

Froese Fischer, C. & Tachiev, G. 2004, At. Data Nucl. Data Tables, 87, 1 (FFT04)

Giddings, J.R. 1981, Ph.D. Thesis, University of London, UK

Gies, D.R. & Lambert D.L. 1992, ApJ, 387, 673

Gold, M. 1984, Diploma Thesis, Ludwig-Maximilians-Universität, München, Germany

Gray, D.F. 1992, *Observations and Analysis of Stellar Photospheres*, 2nd Ed. (Cambridge University Press, Cambridge)

Green, L.C., Rush, P.P., & Chandler, C.D. 1957, ApJS, 3, 37

Grevesse, N. & Sauval, A.J. 1998, SSR, 85, 161

Griem, H.R. 1960, ApJ, 132, 883

Griem, H.R. 1964, *Plasma Spectroscopy* (McGraw-Hill, New York)

Griem, H.R. 1967, ApJ, 147, 1092

Griem, H.R., Baranger, M., Kolb, A. C., & Oertel, G. 1962, Phys. Rev., 125, 177

Griem, H.R. 1974, *Spectral Line Broadening by Plasmas* (Ac. Press, New York and London)

Grigsby, J. A., Morrison, N. D., & Anderson, L. S. 1992, ApJS, 78, 205

Gummersbach, C.A., Kaufer, A., Schäfer, D.R., Szeifert, T., & Wolf, B. 1998, A&A, 338, 881

Hanson, M.M., Kudritzki, R.P., Kenworthy, M.A., Puls, J., & Tokunaga A. T. 2005, ApJS, 161, 154

Heap, S., Lanz, T., & Hubeny, I. 2006, ApJ, 638, 409

Heber, U. & Jeffery, C.J. (eds.) 1992, *The Atmospheres of Early-Type Stars* (Springer, Berlin)

Heger, A., & Langer, N. 2000, ApJ, 544, 1016

Hensberge, H. 1996, in: M. Iye, T. Takata, and E. J. Wampler (eds.), *Workshop on High Resolution Data Processing*, SUBARA Telescope Technical Report No 55, 3

Hensberge, H., 2001, Report, http://astro.oma.be/common/research/dep3/publications/HH-FEROS-PipeEval.pz.gz

Hensberge, H., 2004, in: R. W. Hilditch, H. Hensberge, & K. Pavlovski (eds.), *Spectroscopically and Spatially Resolving the Components of Close Binary Stars*, ASP Conf. Ser. 318, 41

Hensberge, H. & Vershueren, W. 1989, ESO Messenger, 58, 51

Herrero, A. 1987, A&A, 171, 189

Herrero, A. 2003, in CNO in the Universe, ed. C. Charbonnel, D. Schaerer, & G. Meynet (San Francisco: ASP), 10

Hibbert, A. 1975, CPC, 9, 141

Hou, J.J., Prantzos, N., & Boissier, S. 2000, A&A, 362, 921

Hubeny, I. 1992, in: Heber, U. & Jeffery, C.J. (eds.) 1992, *The Atmospheres of Early-Type Stars* (Springer, Berlin), 377

Hubeny, I. 1997, in: De Greve, J.P., Blomme, R., & Hensberge, H. (eds.), *Stellar Atmospheres: Theory and Observations* (Springer, Berlin), 1

Hubeny, I. & Lanz, T. 1995, ApJ, 439, 875

Hubeny, I., Mihalas, D., & Werner, K. (eds.) 2003, *Stellar Atmosphere Modeling*, (ASP, San Francisco)

HummerD. G., Berrington, K.A., Eissner, W. et al. 1993, A&A, 279, 298

Hunter, I., Dufton, P. L., Smartt, S. J., et al. 2007, A&A, 466, 277

Jaschek, C. & Jaschek, M. 1990, *The Classification of Stars* (Cambridge: Cambridge University Press)

Kane, L., McKeith, C. D. & Dufton, P. L. 1980, A&A, 84, 115

Kaufer, A., Stahl, O., Tubbesing, S., et al. 1999, ESO Messenger, 95, 8

Keller, S.C., Bessell, M.S., & Da Costa, G.S. 2000, AJ, 119, 1748

Kilian, J. 1992, A&A, 262, 171

Korn, A. J., Keller, S.C., Kaufer, A., et al. 2002, A&A, 385, 143

Korn, A.J., **Nieva, M.F.**, Daflon, S., & Cunha, K. 2005, *Pristine CNO Abundances from Magellanic Cloud B Stars. II. Fast Rotators in the Large Magellanic Cloud Cluster NGC 2004*, ApJ, 633, 899

Korotin, S. A., Andrievsky, S. M., & Kostynchuk, L. Yu. 1999, A&AS, 260, 531

Kudritzki, R.P. & Hummer, D.G. 1990, ARA&A, 28, 303

Kurucz, R.L. 1988, in: McNally, ed., *Trans. IAU, XXB* (Dordrecht, Kluwer), 168

Kurucz, R.L. 1992, Rev. Mex. Astrof., 23, 45

Kurucz, R.L. 1993a, CD-ROM No. 2–12 (Cambridge, Mass.: SAO)

Kurucz, R.L. 1993b, CD-ROM No. 13 (Cambridge, Mass.: SAO)

Kurucz, R. L. 1993c, CD-ROM No. 18 (Cambridge, Mass.: SAO)

Kurucz, R.L. & Avrett, E.H. 1981, SAO Spec. Rep., 391

Kurucz, R. L. & Bell, B. 1995, CD-ROM No. 23 (Cambridge, Mass.: SAO)

Kurucz, R.L. & Peytremann, E. 1975, SAO Special Report, 362

Lambert, D. L. 1993, PSSCR, T47, 186

Lanz, T. & Hubeny, I. 2003, ApJS, 146, 417 (LH03)

Lanz, T., & Hubeny, I. 2007, ApJS, 169, 83

Lennon, D. L., 1983, MNRAS, 205, 829

Lucy, L.B. 1976, ApJ, 206, 499

Lyubimkov, L. S., Rachkovskaya, T. M., Rostopchin, S. I. & Lambert D. L. 2002, MNRAS, 333, 9 (LRRL)

Maeder, A. & Meynet, G. 2000, ARA&A, 38, 143

Maeder, A. & Meynet, G. 2005, A&A, 440, 1041

McErlean, N.D., Lennon, D.J., & Dufton, P.L. 1198, A&A, 329, 613

Meynet, G. & Maeder, A. 2003, A&A, 404, 975

Mihalas, D. 1978, *Stellar Atmospheres*, 2nd Ed., (Freeman, San Francisco)

Mitnik, D. M., Griffin, D. C., Ballance & C. P., Badnell, N. R., 2003, J. Phys. B, 36, 717

Mokiem, M.R., de Koter, A., Puls, J., et al. 2005, A&A, 441, 711

Mokiem, M.R., de Koter, A., Evans, C.J., et al. 2006, A&A, 456, 1131

Moore, C. E. 1993, in CRC Handbook of Chemistry and Physics, 76th ed., ed., J. W. Gallagher (Boca Raton: CRC)

Morel, T., Butler, K., Aerts, C., Neiner, C., & Briquet, M. 2006, A&A, 457, 651

Munari, U., Sordo, R., Castelli, F., & Zwitter, T. 2005, A&A, 442, 1127

Nahar, S. 2002a, At. Data Nucl. Data Tables, 80, 205 (N02a)

Nahar, S. 2002b, Phys. Rev., 65, 2702 (N02b)

Nahar, S. 2002c, A&A, 389, 716 (N02c)

Nahar, S. 2003, in: Hubeny, I., Mihalas, D., & Werner, K. (eds.), *Stellar Atmosphere Modeling*, ASP Conf. Ser., 288, 651

Najarro, F., Hillier, D.J., Puls, J., Lanz, T., & Martins, F. 2006, A&A, 456, 659

Napiwotzki, R., Schönberner, D., & Wenske, V. 1993, A&A, 268, 653

Nieva, M.F. 2002, *Determinación de Temperatura Efectiva y Estado de Evolución de Estrellas Tipo B, A y F*, Diploma Thesis, Universidad Nacional de Tucumán, San Miguel de Tucumán, Argentina

Nieva, M.F., Cunha, K., Daflon, S., Korn, A.J. 2003, *Chemical Abundances of LMC Fast-Rotating B-Type Stars*, in: *Bol. da Sociedade Astronômica Brasileira*, 23, 123

Nieva, M.F., Heber, U., Edelmann, H., & Przybilla, N. 2007, *Non-LTE abundances of the hypervelocity star HD 271701*, in preparation

Nieva, M.F. & Przybilla, N. 2006a, *C II Abundances in Early-Type Stars: Solution to a Notorious Non-LTE Problem*, ApJL, 639, L39

Nieva, M.F. & Przybilla, N. 2006b, *Present-Day Carbon Abundances of Early-Type Stars*, in: *Nuclei in Cosmos IX, Proceedings of Science*, PoS(NIC-IX)150 (astro-ph/060922)

Nieva, M.F. & Przybilla, N. 2007a, *Hydrogen and helium line formation in OB dwarfs and giants. A hybrid non-LTE approach*, A&A, 467, 295

Nieva, M.F. & Przybilla, N. 2007b, *Accurate Quantitative Spectroscopy of OB Stars: the H, He and C Spectrum*, in: Pasquini, L., Romaniello, M., Santos, N.C., & Correia, A. (eds.), *Precision Spectroscopy in Astrophysics*, ESO Astr. Symposia (Springer-Verlag), in press

Nieva, M.F. & Przybilla, N. 2007c, *Accurate Quantitative Spectroscopy of OB Stars: C and N abundances near the Main Sequence*, in: Benaglia, P., Bosch, G., & Cappa, C.E. (eds.), *Massive Stars. Fundamental Parameters and Circumstellar Interactions*, RMxAA Conf. Ser., in press

Nieva, M.F. & Przybilla, N. 2007d, *Non-LTE line-formation for* C II-IV *in early B-type stars. Self-consistent stellar atmospheric parameters and a reevaluation of the present-day carbon abundance in the solar neighbourhood*, submitted to A&A

Perryman, M.A.C., de Boer, K., Gilmore, G., et al. 2001, A&A, 369, 339

Pfeiffer, M.J., Frank, C., Baumüller, D., Fuhrmann, K., & Gehren, T. 1998, A&AS, 130, 381

Przybilla, N. 2002, PhD Thesis, Ludwig-Maximilians-Universität, München, Germany

Przybilla, N. 2005, A&A, 443, 293

Przybilla, N. & Butler, K. 2001, A&A, 379, 955

Przybilla, N. & Butler, K. 2004, ApJ, 609, 1181

Przybilla, N. & Butler, K. 2007, in preparation.

Przybilla, N., Butler, K., Heber, U., & Jeffery, C.S. 2005, A&A, 443, L25

Przybilla, N., Butler, K., Becker, S.R., & Kudritzki, R.P. 2006, A&A, 445, 1099

Przybilla, N., Butler, K. & Kudritzki, R. P. 2001, A&A, 379, 936

Przybilla, N., **Nieva, M.F.**, & Edelmann, H. 2006, *NLTE Analyses of SdB Stars: Progress and Prospects*, Baltic Astronomy, 15, 107

Przybilla, N., **Nieva, M.F.**, Heber, U., & Jeffery, C.S. 2006, *Non-LTE Metal Abundances in V652 HER and HD 144941*, Baltic Astronomy, 15, 163

Puls, J. & Herrero, A. 1998, A&A, 204, 219

Puls, J., Urbaneja, M.A., Venero, R., et al. 2005, A&A, 435, 669

Quinet, P. 1998, A&AS, 129, 603

Repolust, T., Puls, J., & Herrero, A. 2004, A&A, 415, 349

Repolust, T., Puls, J., Hanson, M.M., Kudritzki, R.P., & Mokiem, M.R. 2005, A&A, 440, 261

Rolleston, W.R.J., Smartt, S.J., Dufton, P.L., & Ryans, R.S.I. 2000, A&A, 363, 537

Rolleston, W.R.J., Venn, K., Tolstoy, E., & Dufton, P.L. 2003, A&A, 400, 21

Roy, J. R., & Kunth, D. 1995, A&A, 294, 432

Ryans, R.S.I., Dufton, P.L., Rolleston, W.R.J. et al. 2002, MNRAS, 336, 577

Rybicki, G.B. & Hummer, D.G. 1991, A&A, 245, 171

Schiff, B., Pekeris, C.L., & Accad, Y. 1971, PhRA, 4, 885

Schöning, T. 1993, A&A, 267, 300

Schöning, T. & Butler, K. 1989, A&AS, 78, 51

Seaton, M.J. 1962, in: *Atomic and Molecular Processes* (Acad. Press, New York and London)

Seaton, M.J. 1987, J. Phys. B, 20, 6363

Seaton, M.J., Yan, Y., Mihalas, D., & Pradhan, A.K. 1994, MNRAS, 266, 805

Shamey, L.J. 1969, Ph.D. Thesis, University of Colorado

Shaver, P.A., McGee, R.X., Newton, L.M., Danks, A.C., & Pottasch, S.R. 1983, MNRAS, 204, 53

Sigut, T. A. A. 1996, ApJ, 473, 452

Sofia, U. J., & Meyer, D. M. 2001, A&AS, 554, L221

Smalley, B. 1996, in: Adelman, S.J., Kupka, F., & Weiss, W.W. (eds.), *Model Atmospheres and Spectrum Synthesis*, (ASP, San Francisco), 43

Stehlé, C. & Hutcheon, R. 1999, A&AS, 140, 93 (SH99)

Trundle, C., Dufton, P.L., Lennon, et al. M.A. 2002, A&A, 395, 519

Unsöld, A. 1955, *Physik der Sternatmosphären*, 2. Aufl. (Springer, Berlin)

Urbaneja, M. A., Herrero, A., Bresolin, F., et al. 2005a, A&A, 622, 862
Urbaneja, M. A., Herrero, A., Kudritzki, R. P., et al. 2005b, A&A, 635, 311
Van Regemorter, H. 1962, ApJ, 136, 906
Werner, K. 1986, A&A, 161, 177
Werner, K. & Husfeld, D. 1985, A&A, 148, 417
Wiese, W. L., Fuhr, J. R. & Deters, T. M. 1996, J. Phys. & Chem. Ref. Data, Mon. 7
Wilson, N. J., Bell, K., L. & Hudson, C. E. 2005, A&A, 432, 731
Wilson, N. J., Bell, K., L. & Hudson, C. E. 2007, A&A, 461, 765
Yan, Y., Taylor, K. T. & Seaton, M. J. 1987, J. Phys. B, 20, 6399
Yan, Y. & Seaton, M. J. 1987, J. Phys. B, 20, 6409
Zaal, P.A., de Koter, A., Waters, L.B.F.M., et al. 1999, A&A, 349, 573

Acknowledgements

"Science knows no country, because knowledge belongs to humanity, and is the torch which illuminates the world." Louis Pasteur

In the beginning of my studies at the National University of Tucumán (Argentina), I met an astronomer, Arcadio Poveda (Mexico), who encouraged me to follow my dream of studying the stars through the rigorous physics formalism (nothing trivial for a woman in South America). I was the first student who did it at that University, which follows the motto *Pedes in Terra ad Sidera Visus*. Several years later, I am concluding the doctorate in Astrophysics.

This thesis work had enormous support from many persons in different countries. I am grateful to some of them for their direct participation in the thesis, to others for contributing to my scientific background. Some of them helped me with administrative issues, gave me good advice and supported me in difficult moments. This enterprise would not have been realised without them and without the financial support.

I am infinitely grateful to *Norbert Przybilla* and *Ulrich Heber* for accepting me to work in their team at the Dr. Remeis Sternwarte Bamberg, for providing excellent working conditions, for very fruitful scientific discussions. Also for their respect of my ideas, my work and my person, for their permanent support, patience, comments and suggestions. Vielen Dank an Beide! A special thank to Norbert, for his immense patience in the long process of constructing reliable model atoms for non-LTE calculations. Thanks for letting me understand part of the wonderful and complicated physics hidden behind these pretty nice lines called spectra. And for the extra working hours answering all my questions, correcting errors, suggesting new tests, reading the manuscripts. Danke schön für deine Details, sie machen doch den Unterschied! Thanks also to Martin Altmann for the spectra required to calibrate model atoms. The stay in Germany was funded by DAAD (German Academic Exchange Service). This allowed me to finish the Ph.D. Danke H. Jupe und W. Gairing für die Unterstützung.

The research project was proposed by Katia Cunha and a preparatory phase for this thesis work was done in Brazil (Observatório Nacional, ON) under her supervision and the collaboration of Simone Daflon. I am grateful to both. Thanks Katia for encouraging me to do a work of high scientific level, for your support, for the possibility to participate in observing runs and for establishing the contact to the German supervisors. Thanks Simone for introducing me to the non-LTE computations, for the interesting discussions and for your questions. I hope I have answered some of them in this work. Muito obrigada! The stay in Brazil was financed by CNPq (National Counsel of Technological and Scientific Development) and the observing runs by ON.

Hugo Levato and Stella Malaroda provided letters of reference for the DAAD scholarship. Muchas gracias por su permanente apoyo! Many thanks to Herman Hensberge

for helping me with the reduction of FEROS spectra, for his patience and his extraordinary experience. Thanks for your interest in my work and thanks to both you and your wife for the kind reception in Brussels. Thanks to Verne Smith and Dmitriy Bizyaev (and John Olguin) for the support at McDonald Observatory (Texas, USA). Thanks to the staff at La Silla (Chile, European Southern Observatory) and at CASLEO (Argentina) for the technical support in observing runs. I am indebt to Keith Butler for his patience in reading some manuscripts, for his valuable comments, his support and interest in my work. Thanks also Joachim Puls for suggestions to some manuscripts.

The participation to conferences, schools and trainings were possible because of the partial financial support of several institutions: the University of Erlangen-Nürnberg (Sternwarte Bamberg and Frauenbeauftragte), DAAD, CERN (European Organization for Nuclear Research), Royal Observatory of Belgium, CNPq, ON. Several persons also provided interesting ideas and feedbacks to this work through very nice discussions: M. Asplund, C. Chiappini, T. Beers, A. Herrero, S. Simón-Díaz, S. Ekström, S. Möhler, D. Fabbian, L. Pasquini, U. Käufl, A. Seifahrt. Thanks to all! I am also indebt to D. Baade, A. Maeder, A. Kaufer, M. Kissler-Pattig for their support and interest in my work and career. Thanks to Ulrich Katz, for giving me excellent advice for planning the last year of my Ph.D. and further career plans through the ARIADNE project at the University of Erlangen-Nürnberg and even now, after the programme. Danke schön!

Thanks to my friends/colleagues/professors at ON for a very nice atmosphere. Diana, Sergio, Cecilia, Flavia, Thais, Bia, Ricardo, Roberta, Vinicius, Wagner, Marcelo, Vladimir, Evgeni, Flavio, Jucira, Kohl, Dalton, Ramiro, Iara, Antares. Obrigada! Rene Duffard found a new home for me in Rio. Gracias! Thanks Diana Andrade and Thais Mothe for the support when I had health problems and no health insurance.

Thanks to my friends/colleagues at the Sternwarte Bamberg for the nice environment. Stefan and Meike Nesslinger, thanks for your help with German: Ich habe viel gelernt. I am grateful to Rainer Sterzer for his friendship and his private and technical support, for helping me with my new home when I arrived to Bamberg. Thanks to Markus Firnstein, Florian Schiller, Heiko Hirsch, Alfred Tillich, Stephan Geier, Christian Karl, Simon O'Toole, Heinz Edelmann, Manfred Hanke, Jörn Wilms, Horst Drechsel, Irmela Bues, Edith Day for making me feel at home in the institute. A special thank to Markus and Florian for reading a draft of my thesis. Thanks to Norberto Castro Rodríguez for the interesting questions and his comments to my thesis.

Thanks Giovanni Pinzón Estrada for beautiful moments, for our friendship, for your point of view of life, for excellent discussions about physics. Muchas gracias por tu amistad! Thanks Patricia Côrtes Nogueira for your sincere friendship. Você é minha irmã brasileira. Sinto saudades de você! Gracias Tity y Silvina por ser mis eternas amigas de la infancia y por apoyarme siempre. Las extraño mucho!

Danke Hedwig und Ernst für ein wunderbares Zuhause in Deutschland. Ihr seid meine Deutsche Familie und ich bin sehr glücklich bei euch. Vielen Dank für Alles!

A special thank to my partner, for his patience and friendship, for the enormous support and for respecting my dedication to work. Thanks for our life together and for your love. Gracias a mi familia por el eterno apoyo, después de viajar tanto para realizar mis sueños que comenzaron en mi niñez, en las noches despejadas de San Javier, con ustedes. Gracias por su cariño y por estar siempre presente cuando los necesito.